Fabrication of Flexible Pressure Sensor Systems for Biomedical Applications

A thesis submitted in partial fulfillment
of the requirements for the degree of

Doctor of Philosophy
in
Electronics and Communication Engineering

by

Anis Fatema
2019802002
anis.fatema@research.iiit.ac.in

Advisor: Dr. Aftab M. Hussain

INTERNATIONAL INSTITUTE OF INFORMATION TECHNOLOGY
HYDERABAD

International Institute of Information Technology Hyderabad
500032, India

June 2024

International Institute of Information Technology Hyderabad
Hyderabad, India

CERTIFICATE

This is to certify that work presented in this thesis proposal titled ***Fabrication of Flexible Pressure Sensor Systems for Biomedical Applications*** by *Anis Fatema* has been carried out under my supervision and is not submitted elsewhere for a degree.

Date	Advisor: Dr. Aftab M. Hussain

To *My Beautiful Mother,*

Habeebunnisa

Acknowledgements

All praise is to Allah the Almighty.

When I started my Ph.D. journey, I had very little knowledge of doing research, making the best presentations, and writing good research papers, and research proposals. I had no knowledge of the semiconductor and flexible electronics world. After five years of my beautiful life at IIITH, I learnt all these things and much more. There are no words to express my gratitude and respect for my mentor, advisor, and well-wisher, Dr. Aftab M. Hussain. I would like to thank him from the bottom of my heart for each and everything, for selecting me to work under his guidance, for escalating my research qualities, for giving me all the life lessons, motivating me, guiding me in the right direction, and providing moral support. He is not only an outstanding mentor but an amazing and incredible human being and a great friend. He is my inspiration and my role model and I will always look up to him for guidance after becoming a professor. I thank God every day for giving me such an amazing mentor.

A special thanks to Prof. Nazek El-Atab who is an Assistant Professor at Electrical and Computer Engineering at KAUST for considering me to be a visiting student at KAUST in Monsoon 2023. I thank her for giving me with the opportunity to work on interesting projects and for her unwavering support. She is an amazing and commendable mentor.

I extend my heartfelt appreciation to my Ph.D. committee members, Prof. S. Sundar Kumar Iyer, Prof. Nazek El-Atab, and Prof. Anshu Sarje, for taking the time off their busy schedule and providing their thoughtful insights, insightful feedback, and constructive critiques that greatly enhanced the quality of this thesis. I am deeply appreciative of all my friends in my research group who have stood by me, offering encouragement, inspiration, and a sense of community.

Finally, I would like to thank my adoring family. Firstly, I would like to thank my loving, extraordinary, protective, and strong mother, Habeebunnisa. I dedicate my every success and education to her. She is my strong pillar of support and the reason I could dare to dream and achieve my dreams. My father, Mohd. Sameer Farooqui has always been encouraging and raised me to be his strong and confident daughter. Secondly, I would like to thank my bold, brave, and affectionate brother, Dr. Mohd. Umar Farooqui for his support and constant motivational talks, whenever I feel low. My beautiful and loving daughter Inaya Fatima has been my driving force for my accomplishments throughout my path and brought all the happiness in my life. She is indeed what her name signifies- ”Gift of Allah” for me. Lastly, I would like to thank my grandparents for their encouragement and prayers for me.

Abstract

In today's sedentary lifestyle, a person spends a substantial amount of time in a sitting position. Having a poor sitting posture can put more stress on specific muscles and joints, forcing them to be overworked and causing them to fatigue, which results in back pains. "Health is Wealth" and when we are talking about a healthy body, posture is as important as eating in the right way and regular exercising. Hence, it is very important for us to sit in the correct posture. Incorrect sitting posture leads to widespread chronic back pain and other health-related issues, particularly in young adults.

We developed a flexible pressure-sensor-array-based smart chair that analyses sitting posture using machine learning algorithms. This is an add-on feature that can be installed on any existing chair or can be integrated into chairs by manufacturers. The solution is completely flexible, requires very low power, and is low-cost. The smart chair works by mapping the body pressure at the seat and the backrest. Machine learning algorithms are used for the training and classification of different postures for posture recognition.

To fabricate a flexible pressure sensor, we presented the synthesis of an organic polymer-polypyrrole used as a piezoresistive conductive material that was synthesized using in-situ chemical oxidative liquid polymerization. The sensor showed high sensitivity at low-pressure ranges and can measure pressure in the range of 160 Pa to 16 kPa. We then presented the design of a smaller sensor array mat (4×4) using a carbon-impregnated conductive polymer named velostat, and performed various tests to ensure that it could be effectively used for posture recognition applications.

We presented the mechanical reliability of a velostat-based pressure sensor. We reported the bending response by examining its reliability when subjected to repeated mechanical stress for 150 bending cycles. We presented for the first time ever, the long-term reliability of velostat by testing it for 210 days. From the results, we observed that the particles of the velostat settle after a particular amount of time on repeated load applications. Once that happens, the change in the resistance of the velostat becomes practically invariant with time. We have observed that the decay ratio is closer to 1 after 210 days. This implies that we can expect reliable and repeatable results from the velostat sensor after the application of load 15 times with a load range from 1 to 12 kg. The relative error is also drastically reduced, and there is an overall error reduction by 53 percentage points in 210 days.

A novel data acquisition circuit design with flexibility to read out both capacitive and resistive types of sensors has been presented. It requires less area and is more cost-effective compared to separate single-sensor read-out circuits. We finally present the design of a smart chair system. We tested different machine learning models for the classification of seven different postures and achieved the best accuracy of 95.89% using the Support Vector Machine (SVM) model and 95.61% using the Neural Network (NN). Though the training time for NN is longer compared to SVM, the prediction speed is almost double that of SVM.

Contents

List of Figures

List of Tables

Abbreviations

ADC	Analog to Digital Converter
AI	Artificial Intelligence
CDC	Capacitance to Digital Converter
CVC	Capacitance to Voltage Converter
DAC	Digital to Analog Converter
DRC	Design Rule Check
EOC	End of Conversion
FSR	Force Sensing Resistor
FXR	FlexiRes
LVS	Layout Vs Schematic
MCE	Minimum Classification Error
ML	Machine Learning
MSE	Mean Square Error
NN	Neural Network
PCC	Polypyrrole coated cotton
pPy	Polypyrrole
PVC	Polyvinyl chloride
RCDC	Resistance and Capacitance to Digital Convertor
RVC	Resistance to Voltage Converter
SAR	Successive Approximation Register
SVM	Support Vector Machine

Symbols

C	Output capacitance
C_0	Initial capacitance
C_s	Sensor capacitance
C_r	Reference capacitance
E_r	Relative error
P	Pressure
R_b	Bias resistance
R_0	Original resistance
R_{sens}	Sensor resistance
R_t	Instantaneous resistance at the applied time
S	Sensitivity
V_0	Output voltage
V_r	Reference voltage
V_{in}	Supply voltage
W	Weight
W_a	Actual weight
W_e	Estimated weight
a, b, n, ψ	Constants
σ	Applied pressure
ε_0	Original strain
θ	Filler volume fraction
φ	Potential barrier height

List of Related Publications

[P1] **Anis Fatema**, B. Kokad. M. Hussain, "Development of Flexible Pressure Sensor System for Posture Recognition in Smart Chair using Machine Learning," submitted in *Scientific Reports*, 2024.

[P2] **Anis Fatema**, S. B. Mishra, A. M. Hussain, "Investigation of Reliability of a Polypyrrole coated Conductive Cotton Fabric for Sensing Applications," in proceedings of *2024 IEEE International Conference on Flexible and Printable Sensors and Systems (FLEPS)*, 2024.

[P3] **Anis Fatema**, S. Chauhan, M. Datta, A. M. Hussain, "Investigation of the Long-term Reliability of a Velostat-based Flexible Pressure Sensor Array for 210 Days", in *IEEE Transactions on Device and Materials Reliability*, vol. 24, no. 1, pp. 41-48, 2024.

[P4] **Anis Fatema**, S. Chauhan, M. Datta, A. M. Hussain, "Polypyrrole-based Cotton Flexible Pressure Sensor using In-situ Chemical Oxidative Polymerization", in proceedings of *2023 IEEE International Conference on Flexible and Printable Sensors and Systems (FLEPS)*, pp. 1-4, 2023.

[P5] **Anis Fatema**, I. Kuriakose, R. Gupta, A. M. Hussain, "Analysis of Interpolation Techniques for a Flexible Sensor Mat for Plantar Pressure Measurement", in proceedings of *IEEE Applied Sensing Conference 2023*, pp 1-3, 2023.

[P6] **Anis Fatema**, A. M. Hussain, "Investigation of Reliability of a Flexible Pressure Sensor Based on a Polyethylene Carbon Composite - Velostat", in proceedings of *MRS Fall Meeting and Exhibit 2022*, Boston, Massachusetts, USA, 2022.

[P7] **Anis Fatema**, I. Kuriakose, D. Devendra, A. M. Hussain, "Investigation of the Mechanical Reliability of a Velostat-Based Flexible Pressure Sensor", in proceedings of *2022 IEEE International Conference on Flexible and Printable Sensors and Systems (FLEPS)* pp. 1-4, 2022.

[P8] **Anis Fatema**, A. Navnit, D. Devendra, A. M. Hussain,"A Combined Capacitance and Resistance Read-out circuit for Sensory Nodes", in proceedings of *IEEE Sensors Conference 2021*, pp 1-4, 2021.

[P9] **Anis Fatema**, A. M. Hussain, "Flexible Pressure Sensor Device for Quantification of Physiotherapy Sessions", in proceedings of *MRS Fall Meeting and Exhibit 2021*, Boston, Massachusetts, USA, 2021.

[P10] **Anis Fatema**, S. Poondla, R. B. Mishra, A. M. Hussain,“A Low-Cost Pressure Sensor Matrix for Activity Monitoring in Stroke Patients Using Artificial Intelligence”, in *IEEE Sensors Journal*, vol. 21, no. 7, pp 9546-9552, 2021.

Related co-author publications:

[P1] S.B Mishra, **A. Fatema**, D. Niteesh, A. M. Hussain, “Development of Conductive Surface on Polyurethane Foam using in-situ Polymerization of Pyrrole for Capacitive Pressure Sensing”, in *IEEE Sensors Letters*, vol. 8, no. 1, pp. 1-4, 2024.

[P2] M. Datta, L. Lakhmanan, **Anis Fatema**, A. M. Hussain, “Characterisation and Quantification of Crosstalk on a Velostat-based Flexible Pressure Sensing Matrix”, *2023 IEEE International Conference on Flexible and Printable Sensors and Systems (FLEPS)*, pp. 1-4, 2023.

[P3] S. Chauhan, Ivin Kuriakose, **Anis Fatema**, A. M. Hussain, “Efficient Calibration Of Velostat-Based Flexible Pressure Sensor Matrix”, in proceedings of *2023 IEEE International Conference on Flexible and Printable Sensors and Systems (FLEPS)*, pp. 1-4, 2023.

[P4] M. Datta, L. Lakshmanan, **Anis Fatema**, A. M. Hussain, “Flexible Writing Pad based on a Piezoresistive Thin Film Sensor Matrix”, in proceedings of *IEEE Applied Sensing Conference*, pp. 1-4, 2023.

[P5] I. Kuriakose, S. Chauhan, **Anis Fatema**, A. M. Hussain, “Wearable Pressure Sensor Suit for Real-Time Detection of Incorrect Exercise Techniques”, in proceedings of *IEEE Sensors Conference*, pp. 1-4, 2022.

List of Patents

- **Indian Patent Office (IPO)**, patent application number **202141022334**: "System and method for monitoring an activity of user from sensor mat using machine learning," Aftab M. Hussain, **Anis Fatema**.
- **Indian Patent Office (IPO)**, patent application number **202341035778**: "System and method for detecting posture of user at smart chair using machine learning model," Aftab M. Hussain, **Anis Fatema**.

Chapter 1

Introduction

1.1 Motivation

Nowadays, people are more conscious of the value of investing in their own well-being, thanks to recent developments in the medical and health sciences as well as the accessibility of information about healthy living. However, because of stress and our contemporary way of life, we probably neglect our health. In particular, the problems of a lazy lifestyle and bad sitting posture have worsened due to the rise in desk-bound work and the usage of electronics like smartphones and tablets [1]. Incorrect sitting postures have been linked to a variety of physical and mental health problems. It has been estimated that we spend between fifty and eighty percent of our days sitting down due to the rise in desk-bound work and widespread usage of mobile devices [2]. People with sedentary employment sit for an average of 9.95 hours during working days and 8.07 hours during non-working days [3]. Slouching, hunching, or slumping are examples of poor posture that cause misalignment along the spinal column and affect all of the major musculoskeletal system components. One of the most vital components of the body is the spine. Any region of the body can become immobile if damage is done to the spinal cord. The body's weight or stress is rearranged due to a misaligned spine, which puts a great deal of strain on the joints. It has been reported that the point, annual, and lifetime prevalence rate of lower back pain in the Indian population (66%) is higher compared to global and other ethnic populations, especially among women, the rural population, and elementary workers [4]. When this back pain extends for over 12 weeks or more, it becomes chronic back pain. It is reported in 2023 that chronic lower back pain is a prevalent issue worldwide, affecting about 1.71 billion people, with a significant proportion being women. It is also a major health concern in India, particularly among women, which is reported to be 80% of women between 20 to 50 years of age [5].

The choice of this research problem was also influenced by a personal motivational story. When my brother was doing his internship after his medical studies, he once told me the story of his patient, who was a truck driver and suffered from terrible back pain. The doctors can only prescribe physiotherapy and painkillers to such patients. Some people avoid doing physiotherapy because they can't afford it, and painkillers are just temporary solutions. My brother said that there are almost 10 to 15 such cases that come regularly. It is a critical problem that has to be solved to save the young generation from

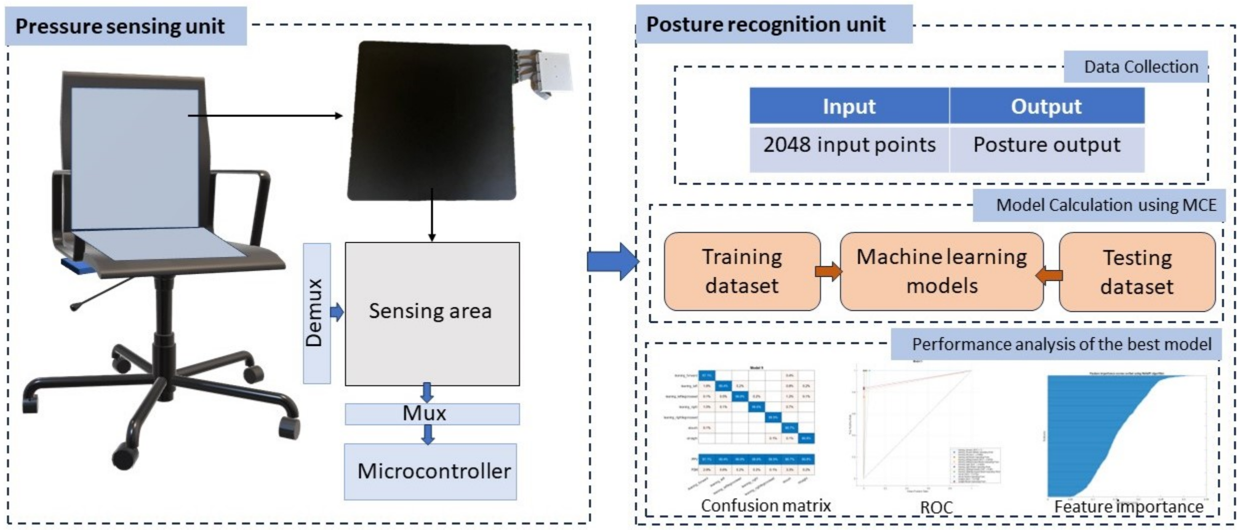

Figure 1.1 Architecture of the smart chair system

chronic back pain. This was a turning point and my motivation for doing this research. Preventing such pains is crucial because there is not a permanent solution outside of physiotherapy. In the words of the well-known proverb, ”Prevention is better than cure,” I started looking into how to avoid experiencing these kinds of pains. Approximately 80 percent of individuals experience persistent back discomfort. It ranks as the third most typical reason for visiting the doctor. An estimated 50 billion dollars are spent annually on back pain treatment only in the United States [6]. Therefore, maintaining good posture when sitting is crucial.

1.2 Smart Chair System

Maintaining good sitting posture is as important as eating a balanced diet and doing regular exercise to have a healthy body. In order for the muscles and joints to function more consistently and effectively, the bones must be positioned correctly. This is known as correct posture. In a number of disciplines, including biomedical engineering and public health services, the study of sitting behavior is becoming popular. We must sit with proper posture because we spend the majority of our waking hours seated. Real-time monitoring and adjustment of sitting postures is one of the main issues that need to be addressed using the newest advancements in sensor technologies and Artificial Intelligence (AI) and Machine Learning (ML) to lower the risk of issues associated with improper posture.

A simple architecture to design a smart chair system using a pressure sensing array is shown in Fig. 1.1. The pressure sensing unit includes designing a pressure sensing mat that can sense the pressure data of the seat and the backrest. After sensing the data, we need a readout circuit to read the data from the sensors. The readout or data acquisition circuit includes a microcontroller or an analog-to-digital converter (ADC). The next step is designing a posture recognition system. The posture recognition subsystem includes data collection, analysis, and classification using ML algorithms and do performance analysis to select the best model. The application service layer is developed on top of the posture recognition subsystem and can display the sensing results, perform activity level assessment, and alert the user to incorrect postures.

The smart chair system has various advantages for maintaining our health, too. By analyzing pressure distribution, it can monitor sitting habits over time, alert users to prolonged periods of sedentary behavior, which can contribute to health issues like obesity, cardiovascular problems, and diabetes. It can detect poor posture and provide real-time feedback to users, helping them maintain proper posture and reduce the risk of musculoskeletal issues. Furthermore, it can collect data on chair usage patterns, helping organizations optimize workspace layouts and improve ergonomic design. In addition to this, it can help in managing energy efficiently in smart office environments. It can integrate with building management systems to optimize heating, ventilation, and air conditioning based on occupancy patterns, contributing to energy savings. By promoting better posture and comfort, it can potentially enhance productivity by reducing discomfort and fatigue associated with prolonged sitting.

Since it is based on a detachable flexible pressure sensor mat, it can be attached to any chair, like a gaming chair, an office chair, wheelchairs, or even chairs in automobiles. For individuals with mobility impairments, it can provide assistance by detecting when they need to change positions or providing alerts if they remain seated for too long. In healthcare settings, smart wheelchairs can enable remote monitoring of patients' sitting behavior, allowing caregivers to intervene if necessary and preventing pressure ulcers or discomfort. Overall, a pressure sensor-based smart chair system offers a range of benefits that contribute to improved health, comfort, productivity, and safety in various environments.

1.3 Contributions of this Thesis

- We presented the synthesis of an organic conducting polymer-polypyrrole using in-situ chemical oxidative liquid polymerization. A flexible pressure sensor was fabricated using polypyrrole-coated cotton (PCC) as a piezoresistive conducting material .

- We presented the design and fabrication of a 4×4 flexible pressure sensor array that works on the principle of piezoresistivity. We have developed a novel AI based algorithm to determine the accuracy of positioning of load by the stroke patients and compared it with mathematical analysis.

- The mechanical reliability of a velostat-based pressure sensor is reported by examining its reliability when subjected to repeated mechanical stress for 150 bending cycles.

- We reported for the first time ever, the reliability of a flexible velostat-based pressure sensing system under long-term and repeated loading. Tests were performed every fortnight for 210 days.

- We presented a novel interface circuit with the flexibility to read out both capacitive and resistive types of sensors known as resistance and capacitance to a digital converter (RCDC). It requires less area and is more cost-effective than separate single-sensor read-out circuits.

- We presented the design of a smart chair system and the different machine learning algorithms used for the training and classification of seven different postures.

1.4 Thesis Outline

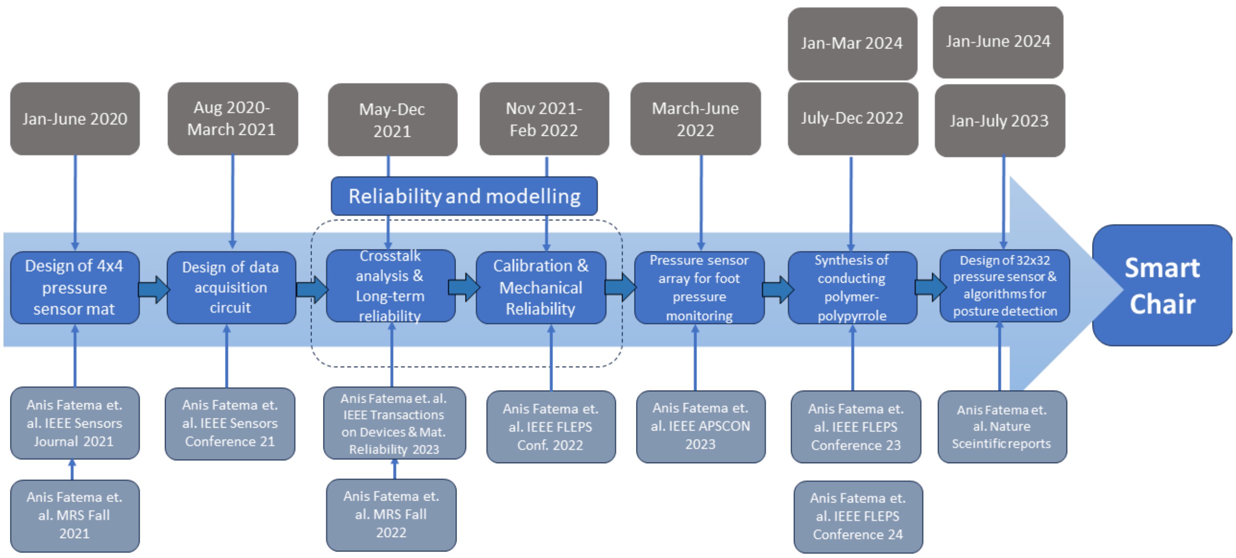

Figure 1.2 Outline of work done

In this doctoral thesis, we described the design and construction of a flexible pressure sensor array-based smart chair that uses ML algorithms to analyze the user's sitting postures. This is an add-on function that manufacturers can incorporate into their chairs or install on any existing chair. The solution is inexpensive, easy to make, breathable, totally flexible, and power-efficient. The way the smart chair functions is by using body pressure mapping at the backrest and seat. Different ML algorithms were used, and performance analysis was done to select the best ML model for training and classification of seven different postures. Fig. 1.2 shows the flow of work that was done. For better understanding, the thesis chapters are arranged in a different arrangement compared to the flow of work done. The pressure sensing system and the posture recognition system make up the two main components of the smart chair system. In Chapter 2, we presented the synthesis of an organic conducting polymer- polypyrrole, and the design of a piezoresistive pressure sensor using polypyrrole. We talked about the construction and design of a pressure sensor system in Chapter 3. A detailed discussion is held regarding the cross-talk, reliability, mechanical reliability, calibration, static, and dynamic features in Chapter 4. The design and development of the data acquisition circuit is covered in Chapter 5. We have manufactured the integrated circuit and designed a resistance and capacitance-to-digital converter in cadence. We talked about the posture recognition system in Chapter 6. We showcased the machine learning methods we have employed together with the model that yielded the highest accuracy. Chapter 7 concludes this thesis by summarizing the results obtained thus far. It provides an overview of the work conducted and presents the future work. The major achievements and challenges in this doctoral thesis are reviewed and summarized.

Chapter 2

Synthesis of conducting polymer for pressure sensing

2.1 Publication History

This chapter contains excerpts from the following publications: [7, 8]

- **Anis Fatema**, S. Chauhan, M. Datta, A. M. Hussain "Polypyrrole-based Cotton Flexible Pressure Sensor using In-situ Chemical Oxidative Polymerization", in *proceedings of 2023 IEEE International Conference on Flexible and Printable Sensors and Systems (FLEPS), 2023*.
- S.B Mishra, **A. Fatema**, D. Niteesh, A. M. Hussain, "Development of Conductive Surface on Polyurethane Foam using in-situ Polymerization of Pyrrole for Capacitive Pressure Sensing", in *IEEE Sensors Letters*.

2.2 Introduction

To design and fabricate a flexible pressure sensor array as a complete hand-made in-lab sensor, we synthesized our own conducting polymer- Polypyrrole (pPy). This chapter presents the synthesis of polypyrrole using in-situ chemical oxidative liquid polymerization and the design of a pressure sensor using polypyrrole-coated cotton. The fabrication of a capacitive pressure sensor using polypyrrole is also presented.

Organic conductive polymer composites (CPCs) are becoming increasingly important because of their capacity to withstand high temperatures and chemical reactions, strong electrical conductivity, affordability, and ability to charge quickly. These properties are a result of the presence of conjugated π-bonds within the CPCs [9]. Electronic conduction in organic polymers is facilitated by the interaction and delocalization of π-electrons in a conjugated carbon chain [10]. The diverse range of preparation procedures and surface deposition techniques enable us to utilize them in several applications. pPy is a widely studied electrically conductive organic polymer due to its simple synthesis, high conductivity, strong environmental stability, and low toxicity at low doses [11]. Due to its excellent bio-compatibility, it has been utilized to connect electrical components and tissues within the human body for the purpose of recording or stimulation [12]. Additional applications documented in the literature encompass chemical sensors utilized for the identification of volatile organic compounds (VOCs) [9, 13], the advancement of wearable sensors [14], electronic skins (E-skins) [15], soft robotics [16], bio-medical applications [17], and the creation of tactile sensors [18]. The mechanical tolerance threshold of pPy makes it very suitable for the design and production of flexible and elastic sensors.

Flexible and stretchable electronics have various application areas, including soft robotics [19, 20], healthcare, and implantable devices in the context of the internet of things (IoT) [21], internet of everything (IoE) [22], and embedded electronics applications [23]. Wearable electronics heavily rely on flexible pressure sensors, which are primarily constructed utilizing techniques such as piezoresistive sensors, [24–26], piezoelectric sensors [27], and capacitive sensors [28]. Piezoresistive sensors have emerged as the leading category in pressure sensing due to their easy manufacturing, affordability, uncomplicated signal processing circuitry, and standardized data collecting technique [29].

When combined with a stretchable substrate or matrix, pPy exhibits a piezoresistive phenomena. Various synthesis techniques have been investigated to enhance the conductivity of the pPy. A polymeric thin film is produced using a multi-phase reaction process to create a hollow sphere structure of the polymer, allowing it to undergo elastic deformation and regain its original shape when pressure is applied [30]. Nanosheets of a pPy thin film have been produced on a graphene oxide layer utilizing solution-based patterning with regulated pore diameters [31]. Fan et al. conducted the synthesis of pPy by performing in-situ polymerization of pyrrole monomer on carbon nanotubes (CNTs) [32]. Their examination revealed the absence of a chemical interaction between the carbon nanotubes (CNTs) and pPy. The CNTs solely serve as a framework for the polymerization of pPy. Shukla et al. conducted a study where they synthesized a copolymer called polypyrrole-grafted-cellulose (pPy-g-Cellu) using a

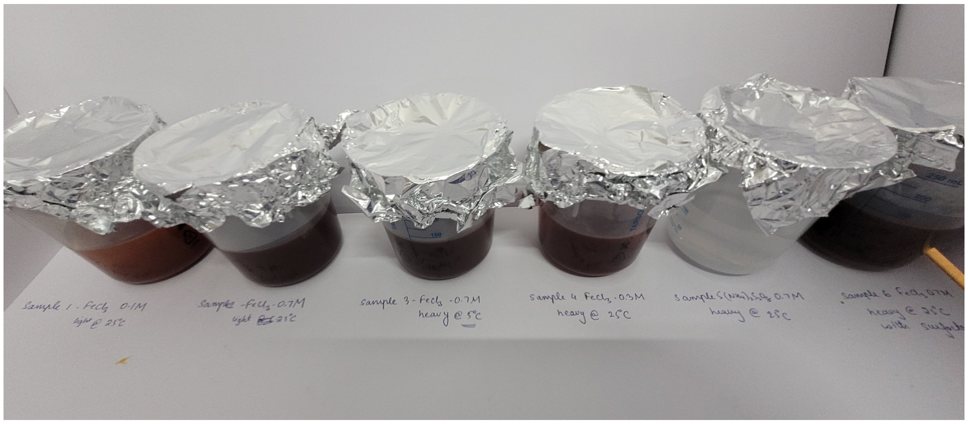

Figure 2.1 Aqueous solutions of $FeCl_3$ with varying molarities (0.3 M, 0.5 M, 0.7 M, 0.8 M).

chemical process. This copolymer showed potential as a material for sensing humidity, with a response time of 25 s and stability for 40 days [33].

pPy was synthesized by performing an in-situ chemical oxidative liquid polymerization of pyrrole monomer on cotton pads. In-situ polymerization enables the seamless incorporation of polymer composites into the desired surface or substance. A flexible, foldable, and stretchable pressure sensor was created by placing the synthesized polypyrrole coated cotton between the copper electrodes, which were then covered with protective layers of paper. The sensor based on pPy demonstrated excellent repeatability and minimal hysteresis.

2.3 Polypyrrole Synthesis and Sensor Design

The process of synthesizing pPy involved the in-situ growth of the material on cotton fiber using liquid chemical oxidative polymerization of pyrrole monomer. The oxidizing agent ferric chloride ($FeCl_3$) was employed to facilitate the polymerization of pyrrole. During the process of chemical oxidative polymerization, the occurrence of propagation, nucleation, and growth of polymer molecules is observed when pyrrole molecules come into contact with $FeCl_3$. $FeCl_3$ acts as an oxidizing agent and plays a role in shaping the micro and/or nanostructure and influencing the electrochemical behavior during the creation of pPy. Prior to usage, a cotton pad and a cotton fabric measuring 5 mm $\times$ 5 mm $\times$ 1 mm were properly cleansed with distilled water and subsequently dried at a temperature of 60°C. Aqueous solutions of $FeCl_3$ with varying molarities (0.3 M, 0.5 M, 0.7 M, 0.8 M) were made by dissolving the compound in distilled water under magnetic stirring until full dissolution. Fig. 2.1 shows the pPy dipped in various molarities of $FeCl_3$.

The pyrrole solution was produced with a concentration of 0.4 M using magnetic stirring. The cotton pads and fabric were immersed in a pyrrole solution for a duration of five minutes, followed by immersion in a $FeCl_3$ solution for one hour at ambient temperature. After one hour, they were extracted and rinsed with distilled water to eliminate $FeCl_3$ and any unreacted pyrrole. The sample was

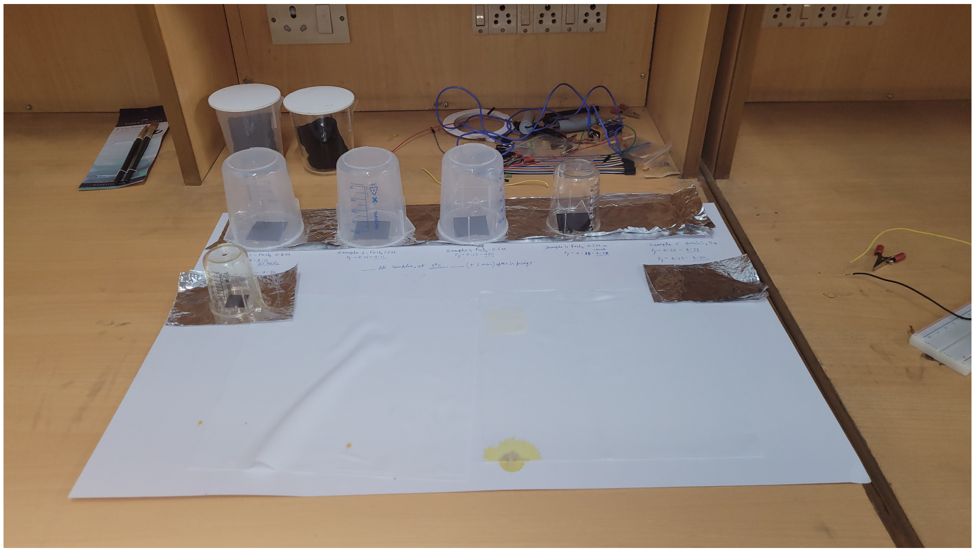

Figure 2.2 Overnight drying of samples under normal environmental conditions

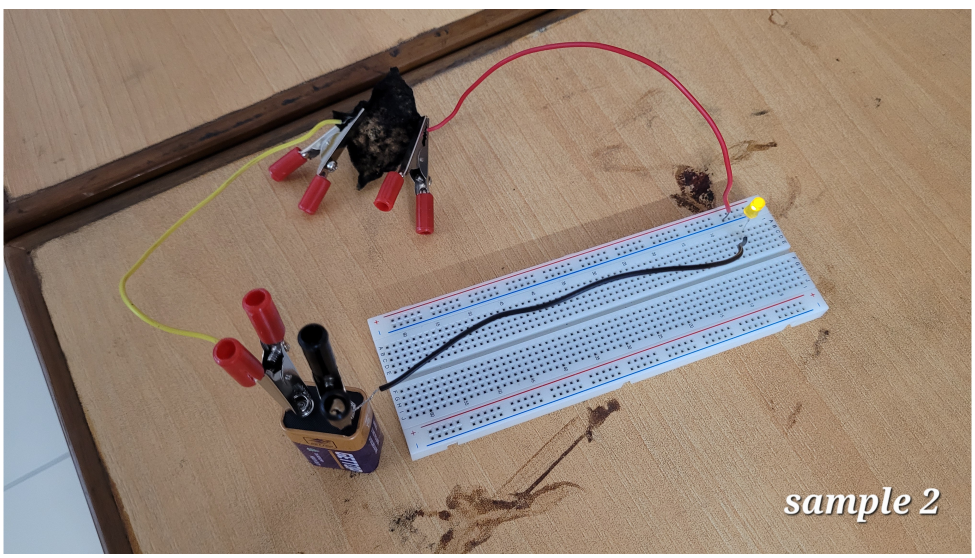

Figure 2.3 Testing the conductivity of the synthesised PCC

subjected to a drying process at a temperature of 60°C, followed by an overnight drying period under normal environmental circumstances. Fig. 2.2 shows all the samples being dried overnight under normal environmental conditions.

The conductivity of all the polypyrrole-coated cotton (PCCs) was assessed, and it was found that the cotton pad immersed in a 0.8M $FeCl_3$ solution exhibited the maximum conductivity. Fig. 2.4 depicts the process of pPy production. In order to create a strain sensor and assess its conductivity, the PCC material was divided into square pieces of 2.5 cm $\times$ 2.5 cm. These pieces were then placed between two copper electrodes that were attached to a sheet of paper.

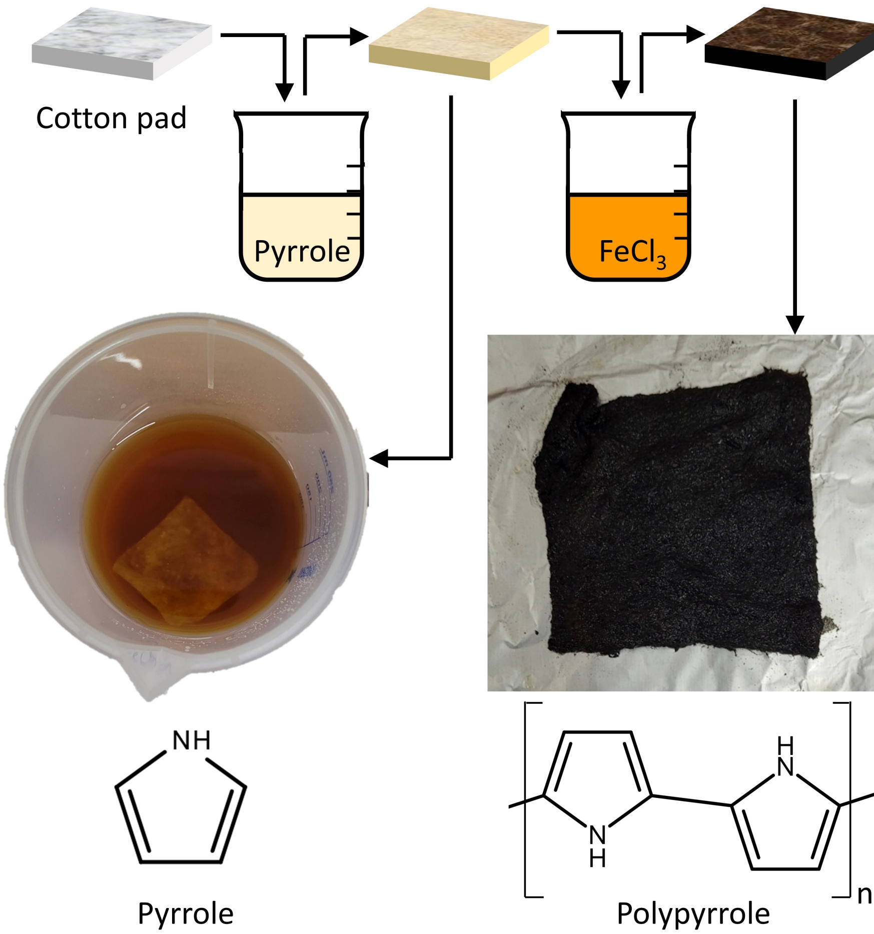

Figure 2.4 Illustration of the process of polypyrrole synthesis on a cotton pad.

2.4 Measurements

2.4.1 UV-visible Spectoscropy

Before using the pyrrole monomer for synthesis, we performed Ultraviolet–visible (UV-VIS) spectroscopy using Jasco V-770 Spectrophotometer of pyrrole and pPy. Fig. 2.5 shows the UV-VIS spectra of pyrrole and the synthesized polypyrrole. We can observe that the absorption peak of pyrrole is 236.5 nm and that of polypyrrole is 496.5 nm which lies in their typical absorption range.

2.4.2 Scanning Electron Microscopy

The morphology of the polypyrrole synthesized using in-situ polymerization can be observed in Fig. 2.5 which shows the Field Emission Scanning Electron Microscope (FE-SEM) images of the PCC under 5K (Fig. 2.5b) and 50K (Fig. 2.5c) magnification. We can observe that the cotton fibers were coated with uniform granular particles of pPy. The strands of cotton fiber are also clearly visible in the

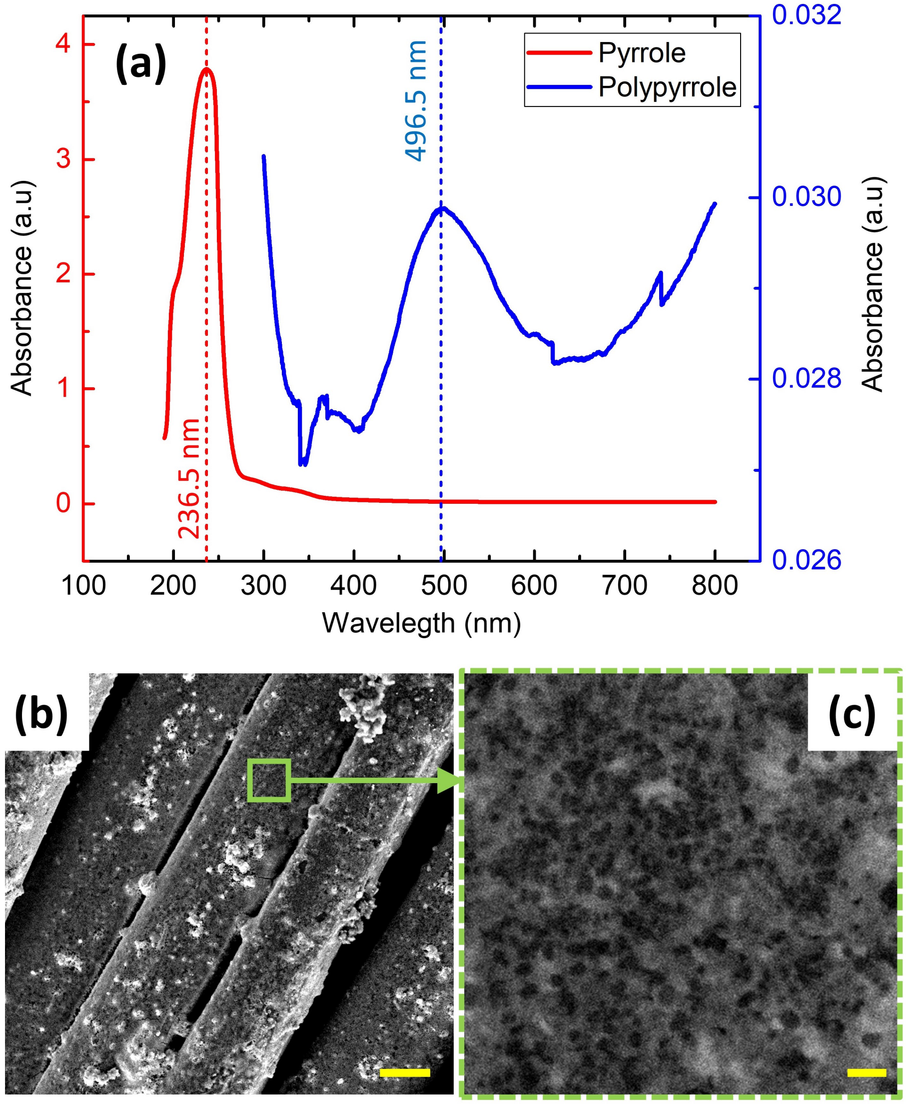

Figure 2.5 (a) UV-visible spectroscopy of pyrrole and polypyrrole shows peaks as expected from their absorption spectra. (b) and (c) Scanning electron microscopy (SEM) images of the cotton fabric after polypyrrole synthesis. Scale bars in (b) and (c) are 2 μm and 200 nm respectively.

image. This confirmed that pyrrole had polymerized on the surface of the cotton pad, and the pPy is uniformly distributed on the cotton strands.

2.4.3 Electrical Property Evaluation

The resistivity of pPy samples was measured using a four-point probe method, using a 2450 Sourcemeter (Keithley Instruments Inc). The four-point probe method is the most common technique to measure sheet resistance due to its low demand for sample preparation and high accuracy. It was observed that the sheet resistance of the cotton pad was 28.09 Ω, and the sheet resistance of the piece of cotton fabric

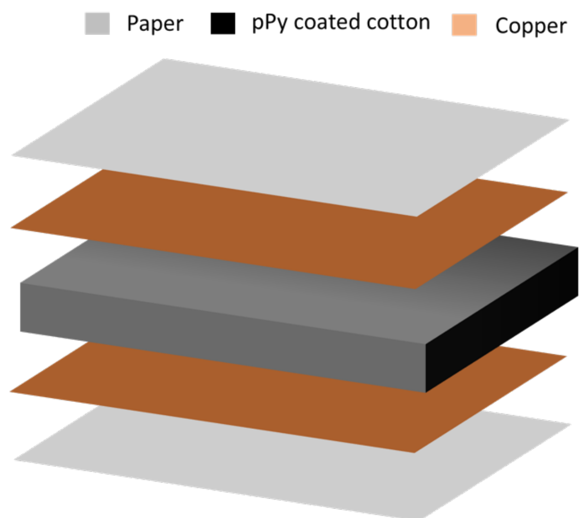

Figure 2.6 Polypyrrole based sensor design

was 5.89 $k\Omega$. We can observe more conductivity in the cotton pad compared to the fabric because the cotton fabric has a natural hollow fibrous structure providing more surface area for the adsorption and polymerization of pyrrole [34].

2.5 Sensor Design and Testing

Following the preparation of the PCCs, the polymer's conductivity was assessed using both a straightforward LED illuminating technique and the more precise four-point probe approach. To evaluate the piezoresistive sensing mechanism of the polymer, a sensor was created by placing the PCC material between the copper electrodes (Fig. 2.6). A 1 kΩ bias resistance was employed to construct a voltage divider circuit, and the output was measured using a microcontroller. Fig. 2.8a displays the force resistance and force-conductance curves of the sensor. For the subsequent trial, we assessed the sensor's capacity to produce consistent results. Pressure sensors, especially those used in commercial and industrial applications, consider it an important metric. The sensor's repeatability was assessed by subjecting it to 1000 loading-unloading cycles with a force of 2 N applied. The sensor had a consistent response, as depicted in Fig. 2.8b. The response time of the sensor was calculated to be 463 ms (10% to 90% rise).

The sensor's response was evaluated when subjected to compressive strain. In order to precisely apply the strain, we positioned the sensor within the jaws of a screw gauge and proceeded to compress it. Our observation revealed an increase in strain and a decrease in resistance. The variation in resistance during compression and expansion (loading and unloading cycle) is seen in Fig. 2.9. The resistance of the sensor decreases from 1.8 kΩ at the initial state to 1.2 kΩ at 99.6% strain. Thus, we report the gauge factor of the sensor to be 0.32 in the large strain range of 0% to 99.6%. Such a large compressive strain range can be achieved with cotton-based sensors because of the fibrous nature of the material.

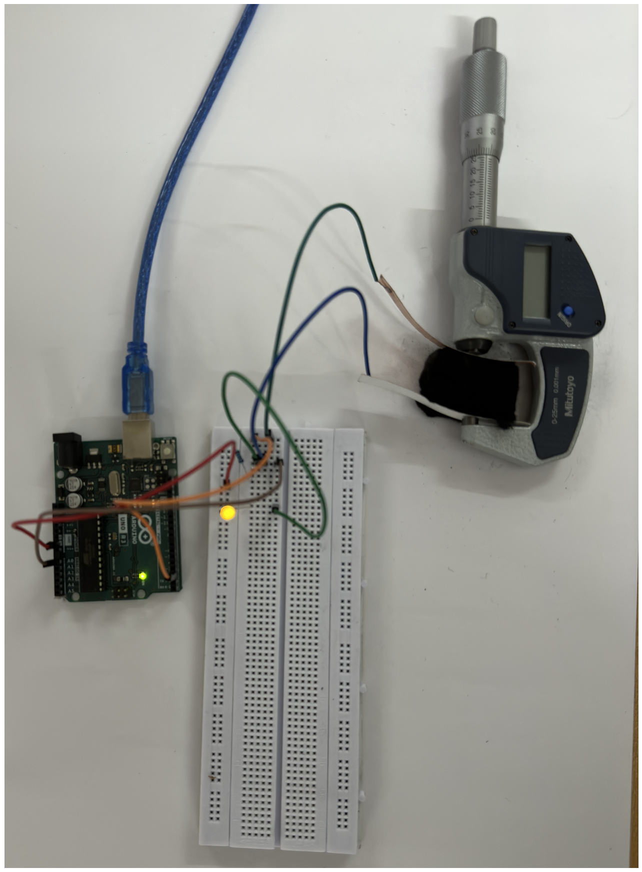

Figure 2.7 Experimental setup for testing the strain response of the polypyrrole-based sensor.

2.6 Fabrication of Capacitive Pressure Sensor using Polypyrrole

In the era of consumer electronics, one of the main study areas is affordable electronics. Although semiconductor fabrication technology has many benefits, it also necessitates expensive equipment and certain materials, which drives up the cost of the devices. Consequently, simple fabrication methods with common household components and fewer fabrication stages have been introduced in recent years [35]. However, appropriate sensitivity, high spatial resolution, and thermo-electromechanical stability should all be features of inexpensive electrical and robotic component development [36–40].

One significant class of materials for the production of inexpensive electronic devices is conductive polymers. These materials must be adjustable both mechanically and chemically. Since different types of pPy can be produced during polymerization in terms of crystallinity, solubility, conductivity, and thermomechanical properties by varying the dopant, oxidant molarities, surfactants, pH values, and temperature, polypyrrole (pPy) is a widely studied conductive polymer with adjustable chemistry. [41, 42]. The conductivity of pPy comes from its π-π conjugated backbone, which is made up of alternating single and double bonded sp^2 carbon atoms [43–45].

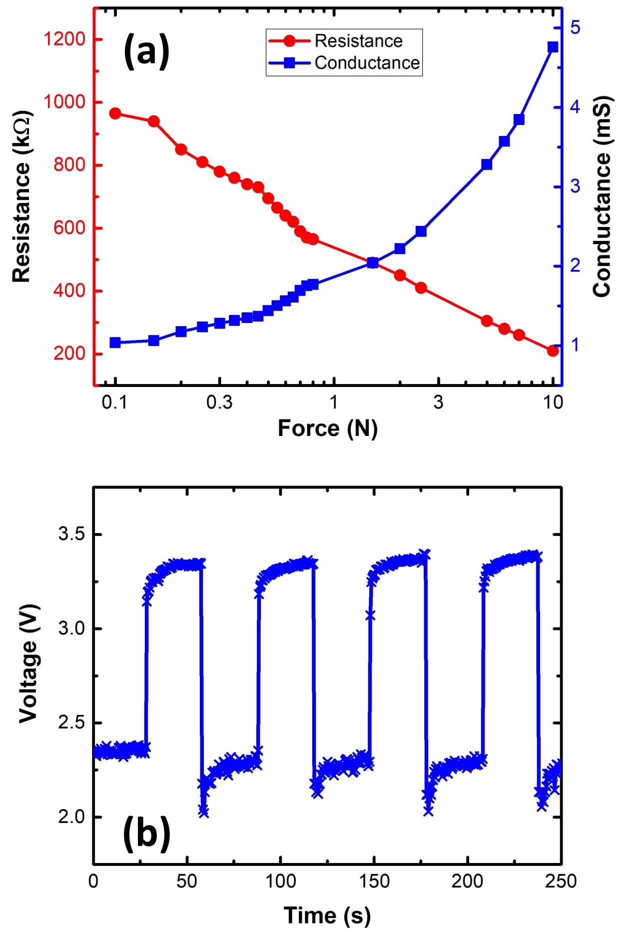

Figure 2.8 (a) The force-resistance and force-conductance characteristic for the sensor with 1 $k\Omega$ bias resistance (b) Response of the sensor for repeated application of load shows repeatable results.

Regarding mechanical sensitivity, dependability, low power consumption, and temperature insensitivity, capacitive pressure sensors show great promise [36, 38]. Due to their high stress tolerance, foams have been investigated as dielectric materials for capacitive pressure sensors. [46–48]. The design and sensitivity of a capacitive pressure sensor depend upon the properties of the electrode material as well as the dielectric. To increase the sensitivity of capacitive pressure sensors many structured dielectrics such as plateau, pyramids, micropillars, matrix arrays and so on have been studied [49–51]. Typically used materials include polymeric foams, porous PDMS, ecoflex, PET, and polymer gel [52, 53].

2.6.1 Sensor Design of polypyrrole based capacitive sensor

Polyurethane foam served as the foundation for the sensor's construction, and two parallel electrodes made of pPy thin film were created on it. The rectangular cuboid foam that was used has dimensions of 2 cm 2 cm 0.5 cm. When in compression within a suitable stress range, this material exhibits linear elastic behavior; at low pressure variations, it displays substantial deformation [54]. $FeCl_3$ was used

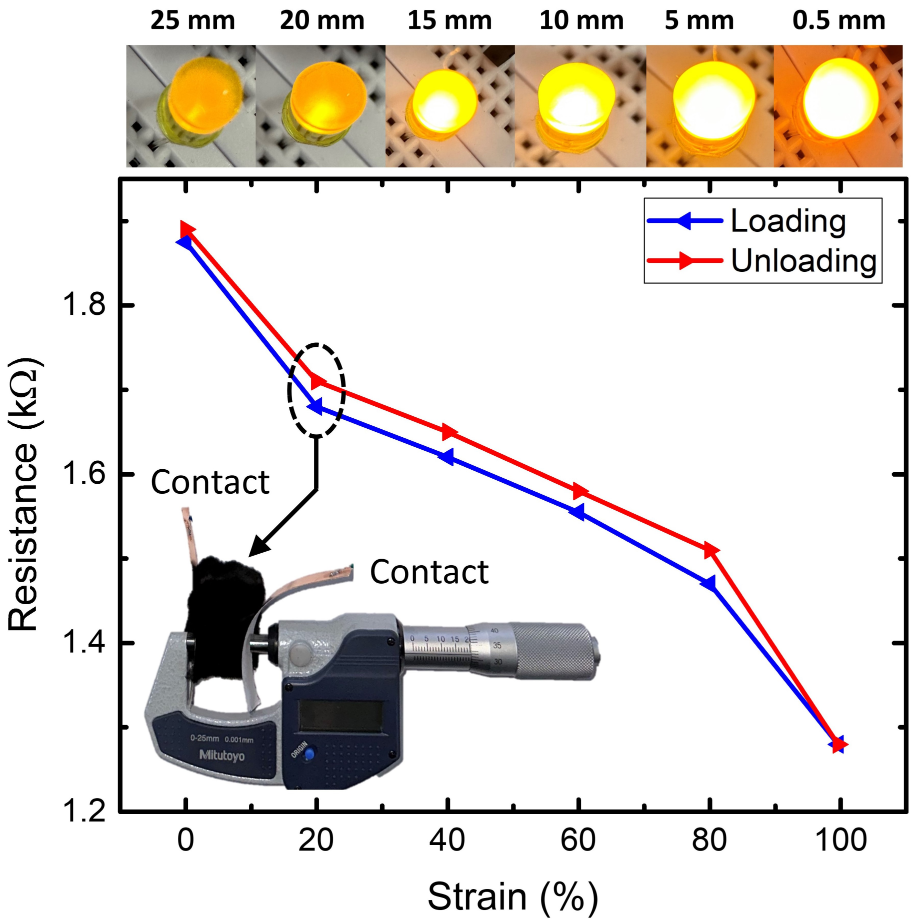

Figure 2.9 Response of a sensor under compressive strain during loading and unloading. The increase in LED intensity indicates the decreased resistance because of strain. Initial length (L_0) = 25 mm.

as the oxidant in an in-situ liquid chemical oxidative technique to prepare the pPy layer on the foam's top and bottom. A heterocyclic aromatic organic chemical with the formula C_4H_4NH and a molecular structure of a five-membered ring, pyrrole is the monomer. By precipitating an amorphous suspension in the majority of the polymerization solution, pPy is produced using this approach.

After properly cleaning the foam with distilled water, hot air was used to dry it. Sample 1: 0.6 M and 0.4 M, Sample 2: 0.6 M and 0.6 M, Sample 3: 0.6 M and 0.8 M, Sample 4: 0.4 M and 0.6 M, and Sample 5: 0.8 M and 0.6 M were the five samples made with varying molarities of pyrrole and $FeCl_3$, diluted in water. We laid the foam on top of the pyrrole solution that had turned yellow after it had dried. We put it in $FeCl_3$ after it had absorbed the pyrrole solution for five minutes. After around 60 minutes, we could see the beginning, growth, and saturation of polymerization (black color).

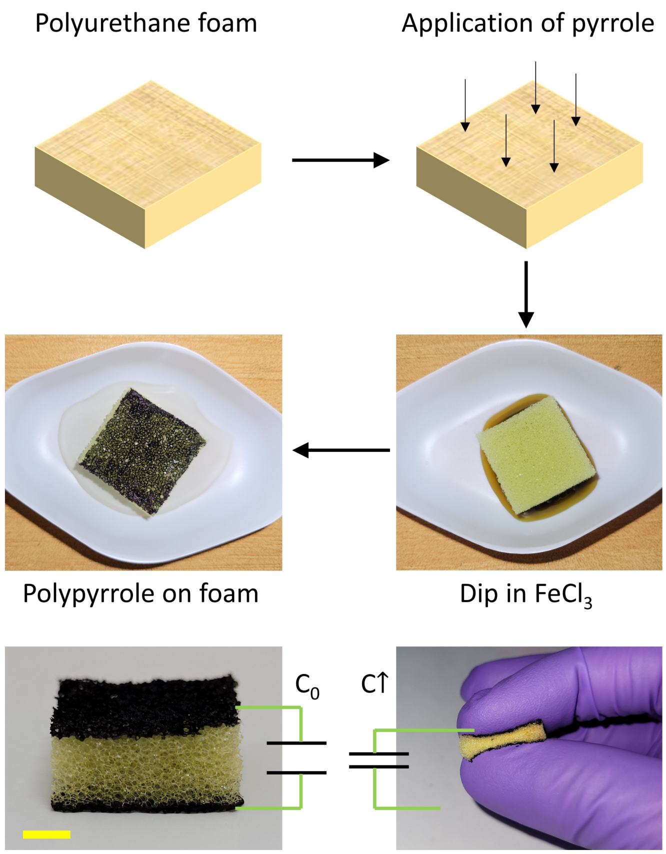

Figure 2.10 Process of polypyrrole surface foam synthesis on both sides of a polyurethane foam piece. Scale bar is 5 mm.

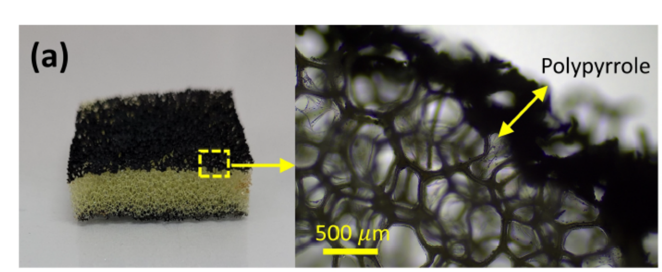

Figure 2.11 Optical microscopy image shows the penetration depth of the pyrrole at the foam surface (roughly 600 μm).

2.6.2 Characterization of the capacitive pressure sensor

The response of the sensor was characterized by applying known pressure onto the foam and measuring the capacitance (using Keysight E4980AL precision LCR meter). To apply pressure on the foam, we first put a transparent, thin, and lightweight acrylic sheet on the sensor to avoid proximity effects while placing the weights and for uniform distribution of pressure. The change in capacitance concerning the

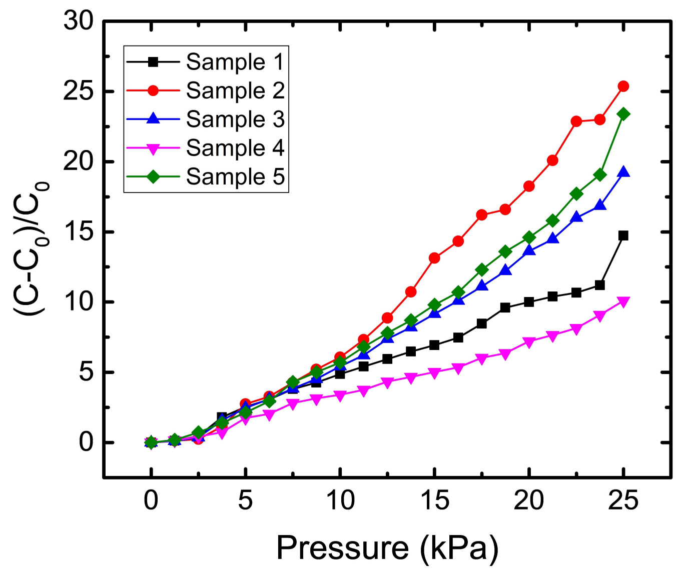

Figure 2.12 Response of various pressure sensor samples for applied pressure.

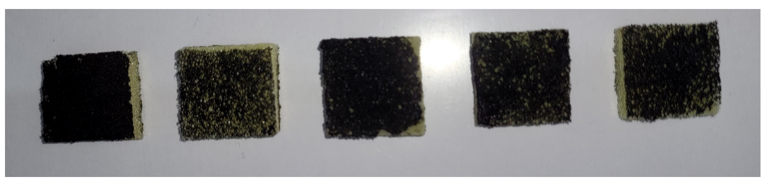

Figure 2.13 Photos of PU foam based capacitive sensor synthesized using different concentrations

initial capacitance ($(C - C_0)/C_0$) was noted for applied pressures. The response for all five samples is shown in Fig. 2.12.

Sensitivity is defined as the change in output for a given change in input stimulation. For a capacitive pressure sensor,

$$S = \frac{\delta(\frac{(C - C_0)}{C_0})}{\delta P} \tag{2.1}$$

where, C is the output capacitance for an applied pressure P, and C_0 is the initial capacitance of the sensor. Out of the five samples, sample 2 had the highest sensitivity, with a molar ratio of one for the monomer and oxidant. For 25 kPa pressure, we report the sensitivity as follows: 1.01 kPa^{-1}, 0.94 kPa^{-1}, 0.77 kPa^{-1}, 0.59 kPa^{-1}, and 0.43 kPa^{-1} for samples 2, 5, 3, 1, and 4. The results given here indicate that electrode qualities like conductivity also influence the sensitivity of a capacitive pressure sensor, even though the dielectric mechanical properties (stress-strain curves) have a considerable impact.

In Fig. 2.14, the sensitivities for each of the five samples are displayed. Sample 2 has the highest average sensitivity, although its value changes over the measurement range, as we have shown. Since sensitivity is a measure of the linearity of the sensor response, an ideal sensor should have a consistent value across its whole range. In our situation, sample 3 displayed the lowest sensitivity standard

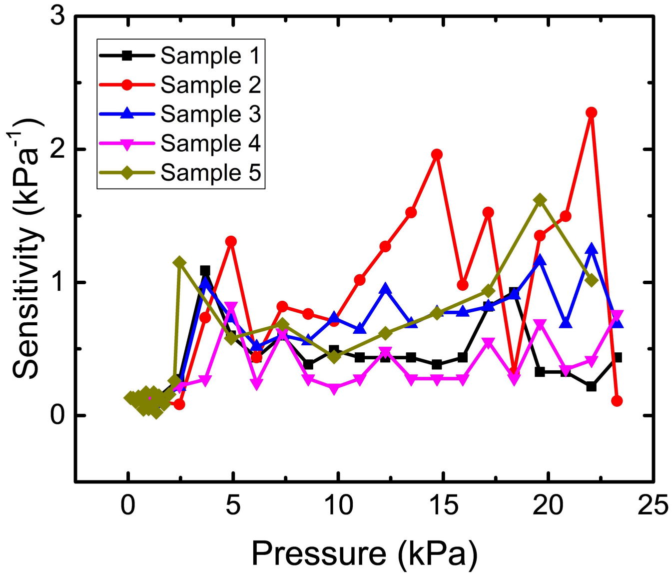

Figure 2.14 Sensitivity of the capacitive pressure sensor for all the five samples. Sample 2 has the highest sensitivity, whereas sample 3 has the most consistent value over the range of measurement.

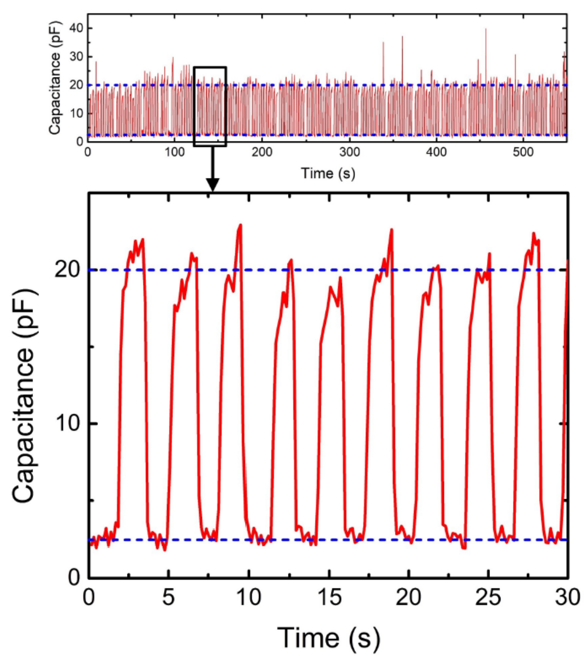

Figure 2.15 Repeatability plot for the sensor after several cycles shows constant output capacitance for the same applied pressure.

deviation of all the samples, although having a slightly larger $FeCl_3$ concentration. As a result, the preparation technique can be used to adjust the capacitive pressure sensor properties. The particular use case for the sensor will determine the trade-off between linearity and sensitivity.

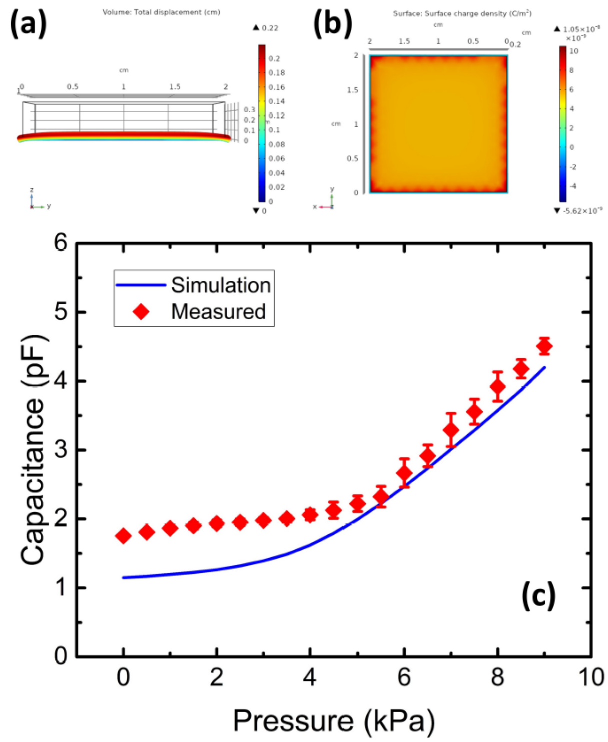

Figure 2.16 Simulation of capacitive pressure sensor (a) Deformation, (b) Space charge density (c) Capacitance vs Pressure compared with experimental results.

We repeatedly loaded and unloaded the sensor with a predetermined weight (in this case, sample 2 with a load of 12.5 kPa) in order to assess the repeatability of the sensor (Fig. 2.15). As may be expected from a repeatable sensor, the oscillation between two capacitance values was seen in the sensor's output. Additionally, it was noted that when the sensor is empty, its reaction spikes. This can be explained by the impact of the user's hand being close by during unloading.

2.6.3 Results and Discussion

It was noted that the foam's length increased in the directions lateral to the applied pressure in the FEM simulations. This was observed throughout the experiment as well. As a result, our practical findings and the deformation results from the FEM simulation agreed quite well as observed in Fig. 2.16. Nonetheless, the simulation's capacitance values were lower than the empirically measured values. The measuring setup and the capacitance added by the test leads are to blame for this. The capacitance values' trend matched the experimental findings. Consequently, capacitive pressure sensors of different dimensions and forms can be simulated using this model. Our research revealed that proximity to the user or other electrically charged surfaces is a crucial factor to take into account when assessing a sensor's capacitance. This is especially true for capacitive sensors that are big and have relatively tiny capacitance variations. When taking measurements, it is important to correctly account for the capacitance of the contact leads by employing open and short circuit compensation.

2.7 Summary

In this chapter, we presented the design of a piezoresistive conducting polymer-polypyrrole. We explored the feasibility and characteristics of a low-cost, flexible, and stretchable pressure sensor on a cotton fabric substrate based on polypyrrole. The in-situ liquid chemical oxidative polymerization method was used to ensure that the pyrrole can polymerize on the cotton fibers uniformly so that the PCC has stable electrical properties. We can also synthesize pPy using other oxidants and surfactants to explore improvements in the stability and conductivity of the polymer. We observed that the conductivity of the cotton pad is better than that of a piece of cotton fabric, possibly because of better adsorption of pyrrole in the pad. Because of the high compressibility of the cotton pad, the sensor can monitor the pressure in a large range, from 160 Pa to 16 kPa. The sensor has a reasonably fast response time of 463 ms. It can be used in various biomedical applications, tactile sensors, and wearable electronics. Though it shows good characteristics, we can't use it in the design of our sensor mat because of the sensing range. So, we used our carbon-impregnated polymer composite- velostat for designing our sensor mat.

We also presented a low-cost, highly sensitive capacitive pressure sensor. The electrodes were made of conductive polymer layers, while the dielectric used in the fabrication of the sensor was polyurethane foam. Pyrrole was polymerized in-situ while $FeCl_3$ was present as a chemical oxidant to create the pPy layers. Using a precision LCR meter, the capacitance was measured for a range of applied pressures following the manufacturing of the sensor. It was noted that the sensor exhibits high sensitivity for a particular molarity of $FeCl_3$ and pyrrole. Applications needing flexible sensor systems, like wearable technology, biomemetic systems, and soft robots, can use this kind of sensor.

Chapter 3

Pressure Sensing System

3.1 Publication History

This chapter contains excerpts from the following publications: [29, 55, 56]

- **Anis Fatema**, S. Poondla, R. B. Mishra, A. M. Hussain, "A Low-Cost Pressure Sensor Matrix for Activity Monitoring in Stroke Patients Using Artificial Intelligence", in IEEE Sensors Journal, vol. 21, no. 7, pp 9546-9552, 2021.
- **Anis Fatema**, S. Chauhan, M. Datta, Aftab M. Hussain, "Investigation of the Long-term Reliability of a Velostat-based Flexible Pressure Sensor Array for 210 Days", in IEEE Transactions on Device and Materials Reliability, 2023.
- **Anis Fatema**, I. Kuriakose, R. Gupta, A. M. Hussain, "Analysis of Interpolation Techniques for a Flexible Sensor Mat for Plantar Pressure Measurement", in Proceedings of IEEE Applied Sensing Conference 2023, pp 1-3,2023.

3.2 Introduction

The most important thing for recognizing the posture of the person is to have an accurate pressure-sensing device from which we can get the pressure maps of the different types of sitting postures of the person sitting on it. In the past decade, different types of sensing materials have been studied to develop high-performance flexible pressure sensors for pressure mapping. There are also commercially available pressure sensors for posture recognition. A sensing chair equipped with a commercially available pressure distribution sensor called the body pressure measurement system (BPMS) manufactured by Teckscan was presented in [57]. It was selected for the flexibility of the sensor sheets and high resolution so they can take the shape of a chair. The sensor sheet had an array of 42-by-48 pressure-sensing elements. Each sensing element gave an 8-bit digital output value that is proportional to the pressure applied. Another commercially available flexible body pressure measurement system (FBPM) manufactured by Teckscan, which was composed of two matrices for the seat and the backrest was presented in [58, 59]. Each matrix contained 16×16 force sensing resistors (FSR). However, these pressure mats are very expensive and require their own software setup, and their properties cannot be changed according to our use. To avoid these difficulties, researchers prefer to make their own pressure sensing mat using low-cost materials that are simple to use, portable, reliable, and can give real-time outputs. The most common pressure sensors that are used in the smart chair system are piezoelectric sensors, capacitive sensors, and piezoresistive sensors.

3.3 Types of Pressure Sensors

3.3.1 Piezoelectric Pressure Sensors

Piezoelectric pressure sensors utilize the piezoelectric effect to measure pressure. Piezoelectric materials generate an electric charge in response to mechanical stress, offering high sensitivity and accurate pressure measurements. They have a rapid response time, making them suitable for dynamic pressure measurements and fast-changing environments. They are typically robust and durable, able to withstand harsh environmental conditions such as high temperatures, vibrations, and mechanical shocks. Depending on the specific design and configuration, piezoelectric pressure sensors can measure a wide range of pressures, from very low pressures to high pressures. They can be used in various applications, such as automotive [60], robotic [61] aerospace [62], medical devices [63, 64], and consumer electronics [65, 66].

Piezoelectric sensors are those that transform changes in force or pressure into electrical charge by using the piezoelectric effect [67–69]. Lead zirconium titanate (PZT) ceramic, aluminum nitride (AlN), etc. are examples of frequently used piezoelectric materials [70]. The use of piezoelectric sensors is limited by the complicated structure of the electronic interface that needs to be built and the advanced fabrication tools required [71, 72]. This is because a charge amplifier is needed to convert the high-impedance charge output to a voltage signal. Although they are sensitive to temperature and bending, piezoelectric thin films of polyvinylidene fluoride (PVDF) [73] and piezoelectric zinc oxide (ZnO) [74] can be employed as flexible sensors. However, installing piezoelectric sensors may require careful mounting and calibration procedures to ensure accurate pressure measurement, especially in applications with non-uniform pressure distributions or dynamic loading conditions.

3.3.2 Capacitive Pressure Sensors

When pressure is applied, a diaphragm moves, which causes a change in electrical capacitance, which is measured by capacitive pressure sensors. They offer good measurement repeatability, can measure a wide range of pressures from vacuum to high pressures, and can be operated over a large temperature range. Normal, transition, touch, and saturation modes are what define them [75, 76]. Despite these advantages, capacitive pressure sensors also have some limitations. For example, designing capacitive pressure sensors with high sensitivity and accuracy can be complex, requiring precise manufacturing processes and calibration procedures. Capacitive sensors may be sensitive to environmental factors such as humidity, temperature, and electromagnetic interference, which can affect their performance and reliability. While capacitive sensors can measure a wide range of pressures, they may have limitations in extreme pressure conditions or very high-pressure applications. Furthermore, high-quality, high-performance capacitive pressure sensors may be relatively expensive compared to other types of pressure sensors, particularly for specialized or high-precision applications. Although, flexible materials can also be used to create capacitive sensors, their application is limited by parasitic capacitance [77,78].

3.3.3 Peizoresistive Pressure Sensors

Anytime pressure or mechanical strain is applied to a piezoresistive sensor, it changes resistance. Due to their various benefits, including their straightforward design, affordability, robustness, high resolution, and output linearity, these kinds of sensors are frequently employed [79, 80]. Piezoresistive sensors offer high sensitivity, allowing them to detect small changes in pressure accurately. They can measure a wide range of pressures, from very low pressures to high pressures, depending on the specific design and configuration. Furthermore, piezoresistive sensors can be designed to have good temperature stability, reducing the need for temperature compensation techniques and ensuring accurate measurements over a wide temperature range. They also have a rapid response time, enabling them to detect pressure changes quickly in dynamic environments. They are often compact and lightweight, making them suitable for integration into small and space-constrained systems. They generally have low power consumption, making them suitable for battery-powered or portable devices. They are also robust and durable, capable of withstanding mechanical shocks, vibrations, and harsh environmental conditions. They may exhibit low drift in their electrical properties over time, maintaining calibration and accuracy over long periods without frequent recalibration.

The advantages of piezoresistive materials and force sensing resistors also include their ability to be produced using flexible materials, their resilience to noise, and their straightforward conditioning electronics (bias resistors) [81]. Force Sensing Resistor (FSR) is one of the most popular piezoresistive sensors that can be purchased commercially. It's a conducting polymer that responds to force by altering its resistance. Particles that carry electricity and those that do not make up the sensing film are arranged in a matrix. Particles on the sensing film's surface come into contact with the conducting electrodes when force is applied, altering the film's resistance. Using the FSR sensor design results, specifications, and signal conditioning designs in accordance with the application needs, numerous researchers have performed measurements of pressure and posture analysis [82]. Velostat was also the subject of numerous experiments in which pressure sensors were created and applied to a variety of applications, including wearable sensors [83], real-time tracking systems in music [84], footprint pressure system [85], finger gesture recognition [86], smart chairs [87], in-socket pressure sensing [88], and many more.

3.4 Velostat Material

Velostat, which is also known as linqstat, is a conductive polymer that was initially used as a packaging material to protect and avoid damage from electrostatic discharge. It is now being extensively explored due to its electrical properties and is being showcased in mechatronics and biomedical applications [77, 89, 90]. It is a low-cost flexible material with piezoresistive properties, making it an attractive option for flexible sensing applications. It is an opaque conductive film made of a polyolefin matrix impregnated with carbon particles. The entrapped carbon particles turn the initially dielectric polymer matrix into electrically conducting composite material [91]. The piezoresistivity of velostat is due to the reduction in the distance between the conductive carbon particles due to the compression of the material [92]. Velostat is typically thin and flexible, allowing it to conform to curved surfaces and bend without losing its electrical properties. This flexibility makes it suitable for embedding into wearable electronics or conformable sensor systems. It is relatively inexpensive compared to other conductive materials, making it an affordable option for prototyping, experimentation, and low-cost electronic projects. It can be easily cut, shaped, and manipulated, making it versatile for various DIY and maker projects. It can be integrated into textiles, paper, or other materials to create custom sensors or electronic interfaces. While primarily used for its pressure-sensitive properties, velostat can also provide some degree of electromagnetic interference (EMI) shielding when grounded, making it useful in electronic enclosures or as a protective layer for sensitive components. However, velostat's conductivity can be affected by environmental factors such as temperature, humidity, and exposure to moisture, which may need to be considered in certain applications. Overall, velostat offers a unique combination of electrical conductivity, pressure sensitivity, flexibility, and affordability, making it a versatile material for a wide range of electronic applications.

The sensitivity of velostat to the application of pressure is defined by two physical phenomena: quantum tunneling and percolation [93]. Quantum tunneling uses the tunnel effect that affects the conductivity of the composite material when the distance between conductive particles inside polymeric

Figure 3.1 Velostat

materials varies due to the applied pressure, which deforms the material. Percolation is a function of geometrical features. It is linked to a change of conductivity between the isolating and conductive state of a composite material caused by the change in volume fraction of the conductive particles [94]. Thus, velostat changes its electrical resistivity upon application of pressure, strain, or mechanical bending due to the effects described above.

When pressure is applied to the velostat, the higher the pressure applied, the higher the change in conductivity. However, extremely high pressure can damage the velostat and lead to loss of conductivity or shortening of the measurement circuit [91]. In a comparison between fresh and used velostat, the resistance of the new material is higher. This is due to the fact that the applied load causes a permanent reorientation and "settling" of the carbon particles (hysteresis) [91]. The electrical properties of velostat also change with material aging [93]. Velostat-based sensors are highly sensitive to bending, stretching, creasing, and large pressures that can damage the material. It is essential to handle the material in a specific way to maintain its reliability.

3.5 Related work

Under the design and fabrication of piezoresistive pressure sensors, velostat has been extensively explored due to its low cost and flexibility. The use of velostat has been studied in the literature in various applications such as human motion monitoring [77, 95], pressure distribution in insoles [96], posture recognition [97], quantification of hand forces [98], finger gesture recognition [99], in-socket

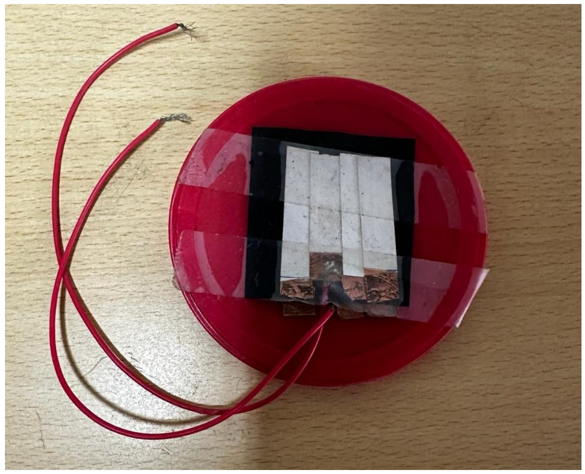

Figure 3.2 Photograph of the first single sensor

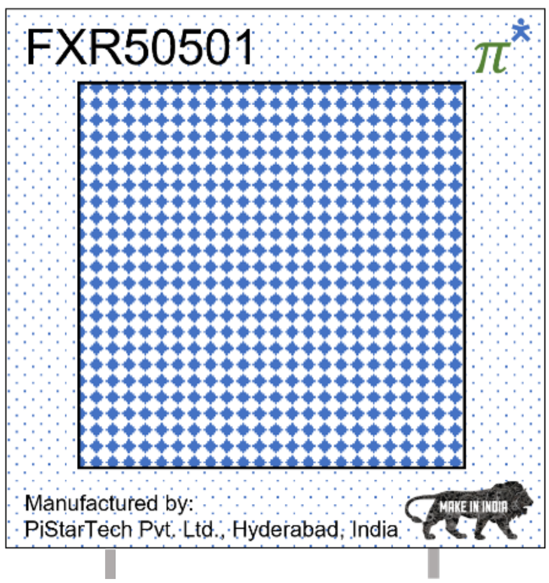

Figure 3.3 Photograph of the FXR sensor

pressure sensor [86], in vivo recordings in the gut [100], assessment of psychomotor development in children [101], neonatal monitoring [87], and many more.

In [77], a force-sensing resistor based on velostat was developed. For the electrodes, they used printed conductive ink on a polyethylene terephthalate (PET) substrate. It measured pressure in the range 0-2.7 kPa. Velostat was also used with different conducting materials for testing in human motion monitoring as presented in [95]. In one design, the velostat layer was sandwiched between two layers of conducting fabric sensors made from medical grade elastic fiber (76% Ag plated and 24% nylon). In another design, they replaced the conducting fabric with conducting thread composed of the same medical-grade elastic fiber. In the last type, the electrodes were made by stitching conductive thread

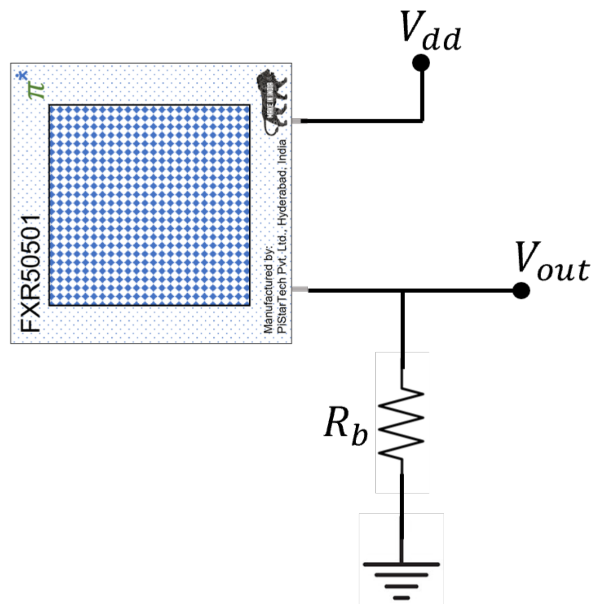

Figure 3.4 Circuit design to read the response of sensor from FXR

into neoprene strips to make the electrodes. After conducting experiments on the three types of sensors, they concluded that a small density of electrodes resulted in higher resistance change. Hence, we can conclude that the electrode configuration and composition affect the sensor performance. In [96], they designed a velostat-based pressure sensor using PVC as a protective material along with a pneumatic actuator for pressure sensing in insoles. In [97], a velostat-based pressure sensor was developed using aluminum foil as the conducting electrode. They developed 16 such sensors and placed them on the seat and backrest for posture recognition. In [86], they developed a wearable pressure-sensing glove using velostat and conductive yarn as electrode, used for finger-gesture recognition.

3.6 Design and Fabrication of Sensor Array

3.6.1 Introduction

In order to design a large sensor array, it is important to design a smaller matrix array first, i.e., a prototype model, and perform the characterization to ensure that the larger sensor matrix will work effectively. We started designing the prototype of the pressure sensor by first designing and fabricating a single sensor, as shown in Fig. 3.2. The working of this sensor is similar to the commercially available sensor FSR. After testing the first sensor as the proof of concept (PoC), we designed a better version of the sensor and named it FXR, as shown in Fig. 3.3.

The FXR is a square flexible force sensing resistor. It has a sensing area of 50 mm $\times$ 50 mm. Its thickness is 0.4 mm and dimensions 70 mm $\times$ 70 mm. The FXR sensors exhibit a decrease in resistance with an increase in force applied to the sensor. They can be characterized for human-machine

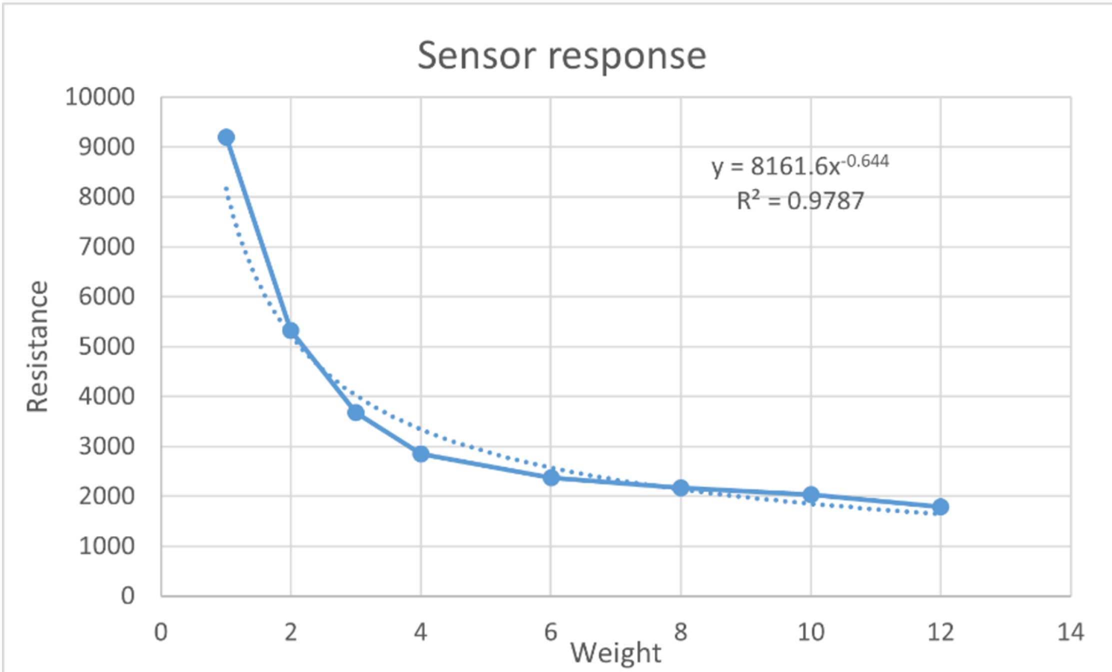

Figure 3.5 Sensor response of FXR

Table 3.1 Sensor Characteristics of FXR

Characteristics	Value
Force range	0.1 N - 40 N
Voltage range	1.8 V - 5 V
Rise time	0.2
Delay time	0.13
Drift	$\leq$ 3% for 1 kg load 1 day
Operating temperature	-40^0C to 60^0C
Electromagnetic Interference	Generates no EMI
Electrostatic discharge	Not ESD Sensitive

interface applications with a typical force range from 0.1 N to 40 N. The sensing range can be varied according to your requirement by varying the value of the bias resistor of the read-out circuit. The sensor characteristics are shown in the Table 3.1.

The entire sensing area of FXR is a single contact point. Hence, the applied load should be distributed evenly across the sensing area to get an accurate and repeatable response. The sensor must be loaded consistently or in the same way, each time to get repeatable readings. Readings may vary if the load distribution changes. If the load is bigger than the sensing area, then we have to use a lightweight, rigid material with the same dimensions as the sensing area and then place the load on top of it. The circuit connection to read the sensor response is shown in Fig. 3.4, which is a voltage divider circuit. Fig. 3.5 shows the response of FXR.

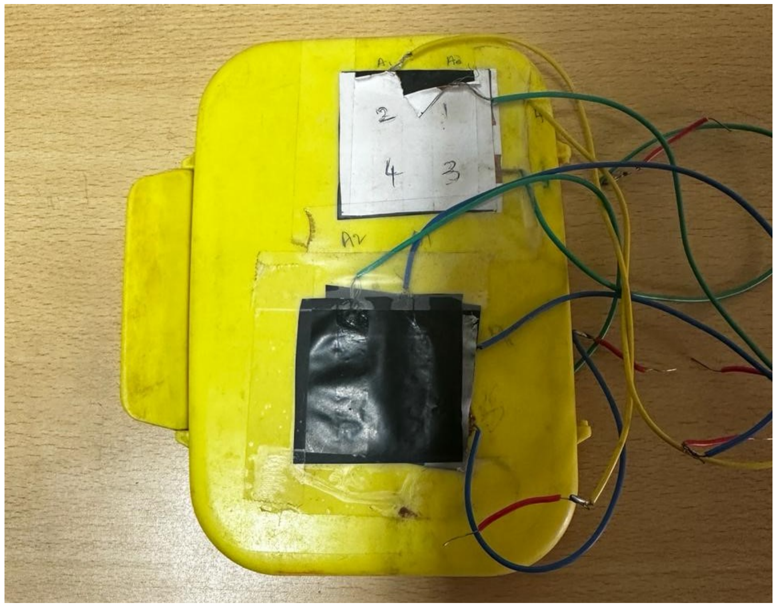

Figure 3.6 2×2 sensor array

Sensor resistance was measured after 10 s of applying load. The force was applied using a push-pull force gauge. Conditioning of sensors is essential for achieving accurate results. To condition a sensor, place a test weight on the sensor for some time and allow it to stabilize. The steps were repeated for four to five times before using it for actual sensing.

After designing the FXR, then we designed the first sensor matrix of size 2×2 as shown in Fig. 3.6. We designed it in a small area with sensor pixel dimensions of 10 mm $\times$ 10 mm and a pitch of 10 mm. We used the raster scanning method for reading the sensor response. After getting good results, we moved to another array of size 4×4.

In the next section, we will discuss the design and fabrication of a 4×4 sensor matrix and its static and dynamic characteristics. We will also present the application in which it can be used. Then, we will present the evolution of the sensor matrix from 4×4 to a 32×32 sensor matrix and the reason for selecting the above dimensions.

3.6.2 Design of a small (4 x 4) sensor array

As illustrated in Fig. 3.7, a sandwich structure consisting of three layers was used to fabricate a 4×4 pressure sensor matrix. Papers with copper electrodes arranged vertically and horizontally are layers 1 and 3, respectively. Due to their high conductivity, copper tapes were chosen as the electrode material. Aluminum tapes are another option, although the conductivity is less than copper. The velostat sheet with a thickness of 106 ± 2 μm made up Layer 2. It was seen that each paper had a thickness of 99 ± 1 μm (Mitutoyo micrometer). As a result, the pressure sensor matrix's overall thickness was roughly $304 \pm 1\mu$m, giving it a significant degree of flexibility. The copper electrodes had a width of 1 cm and a

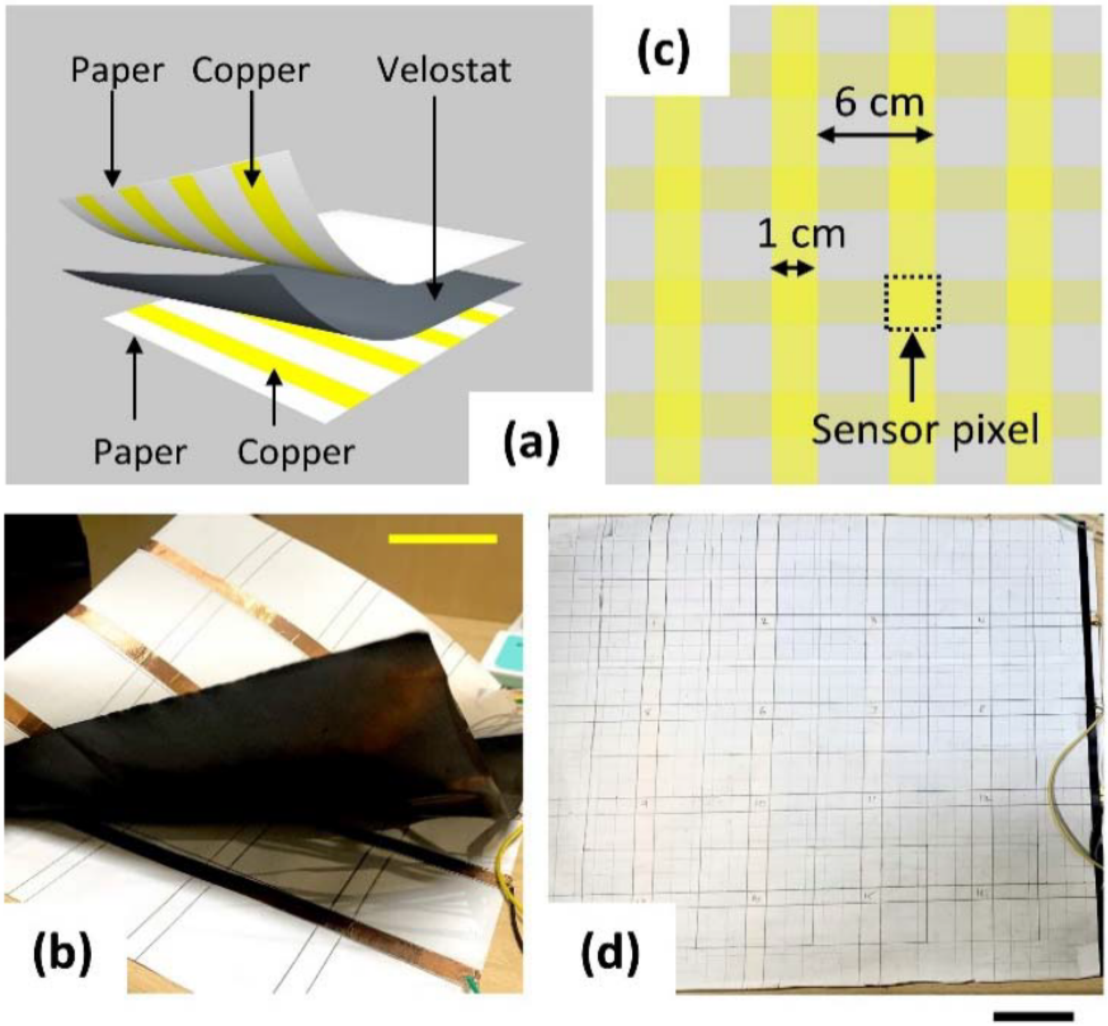

Figure 3.7 (a) Design of the flexible pressure sensor matrix with three layers. Layer 1 and layer 3 are paper with copper electrode strips, while layer 2 is a conductive foam (velostat); (b) Photograph of the fabricated pressure sensor matrix; (c) Design and dimensions of the 4 × 4 sensor matrix with a sensor pixel of 1 cm × 1 cm size, and pitch of 6 cm; (d) Photograph of the completed sensor matrix. Scale bars in (b) and (d) are 5 cm.

pitch of 6 cm between them. Each layer of paper had four of these copper strips attached to it. Thus, the individual sensor pixel is of size 1 cm × 1 cm with a pitch of 6 cm, as shown in Fig. 3.7 (c). Cables were soldered onto copper tapes, and all the sides of the pressure sensor were sealed with adhesive cellophane (scotch tape). When a force is applied to the pixel, its resistance changes, which can be sensed through the copper electrodes.

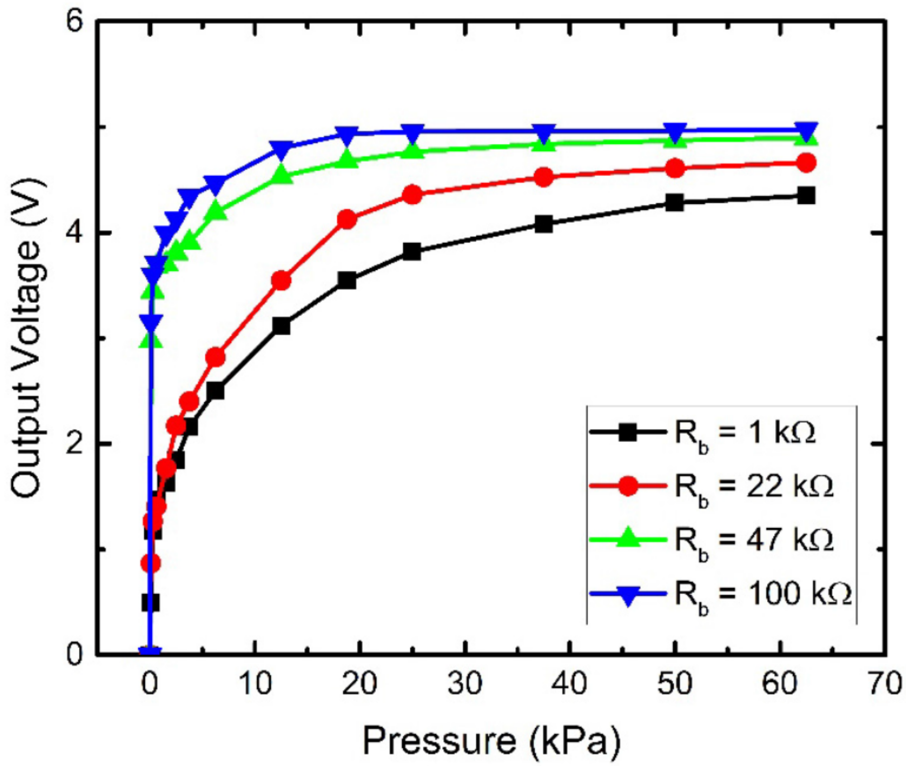

Figure 3.8 The change in bias resistance can affect the range and sensitivity of the system. A higher range is obtained for low values of bias resistance (1 kΩ), while higher sensitivity (at a lower range) is obtained for high values of bias resistance (100 kΩ).

Each sensor paired with the bias resistor was connected to the microcontroller's analog input, while the vertical copper electrodes were connected to the digital pins. The voltage at this pin was read as the output voltage for the particular sensor line. To read the output of a specific pixel, the particular horizontal line was energized by providing a stable DC input voltage, while the output signal was read through the vertical line. Each sensor value was measured at the rate of 0.1 s. It was observed that when no pressure was applied on the pressure sensor, the output voltage was zero, and as the pressure increased, the output voltage increased from 0 V to 5 V. For testing of the system, calibrated weights with constant surface area were used, varying from 0.1 kg to 10 kg, and the response of the system due to variation of weights was recorded. The output voltage for the system is given by:

$$V_o = V_{in}\left(\frac{R_b}{R_b + R_{sens}}\right) \tag{3.1}$$

where V_o is the output voltage, R_{sens} is the resistance of the velostat, and V_{in} is the input voltage. The response curves for a range of bias resistance values, from 1 kΩ to 100 kΩ, were recorded in order to choose an appropriate value for the bias resistor, as the output voltage is dependent upon it. Since the sensor matrix thickness is not strictly uniform, the sensor matrix was put on a level surface for this

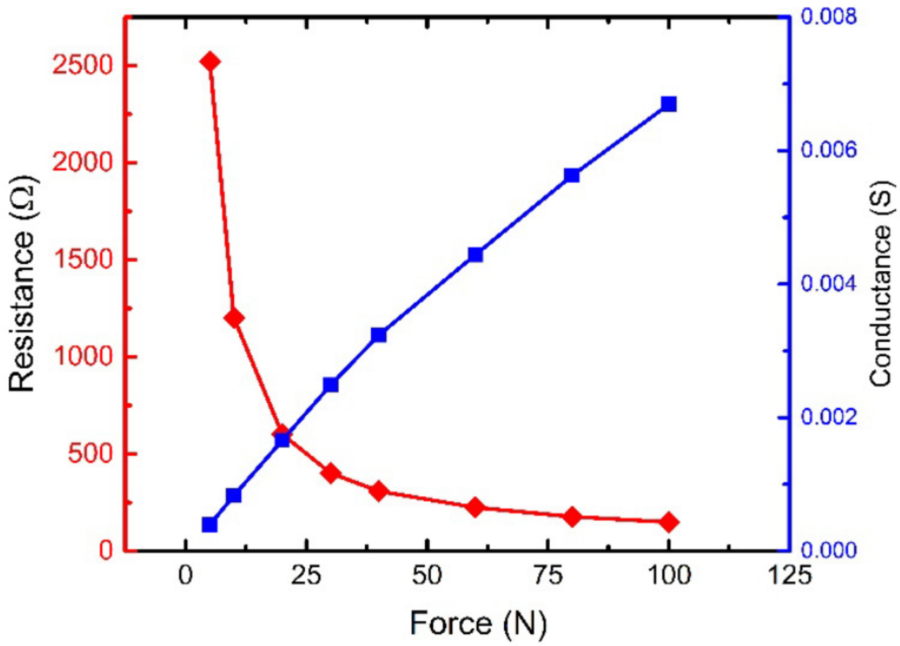

Figure 3.9 The force-conductance characteristic for an individual sensor pixel with 1 kΩ bias resistance shows approximately a liner increase in conductance with applied force.

experiment. A non-conductive, level block measuring 4 cm by 4 cm was positioned between the weight and the sensor to ensure uniform force distribution on each individual sensor. In order to ensure that the voltage was in a stable state, the output voltage was measured 10 s after the load application. Fig. 3.8 displays the output voltage vs applied force characteristic for four distinct values of bias resistance.

We can observe from the graph that when the bias resistance is increased, the sensor gets saturated at lower weights. At bias resistance of 100 kΩ, pressure greater than 20 kPa saturates the system. Hence, in order to cover a large range of pressures up to 60 kPa, a bias resistor of 1 kΩ was selected. A value lower than 1 kΩ would have caused excessive current through the system because the readout circuit was in a simple voltage divider configuration. It should be noted that the sensitivity of the sensor is higher for larger values of bias resistance, particularly for lower loads. This can be helpful in applications where higher sensitivity is required.

3.6.2.1 Static and Dynamic Characteristics of the Sensor

The sensor response for weights varying from 0.1 kg to 10 kg is shown in Fig. 3.9. We have given some relaxation time while changing the weights so that the sensor gives a stable value. The output voltage corresponding to the applied pressure is calculated by taking the mean of the values obtained in that particular period. In Fig. 3.9, we can see that the sensor resistance has more likely a power-equation relation in the force-resistance response and a relatively linear-equation relation in the force-conductance response.

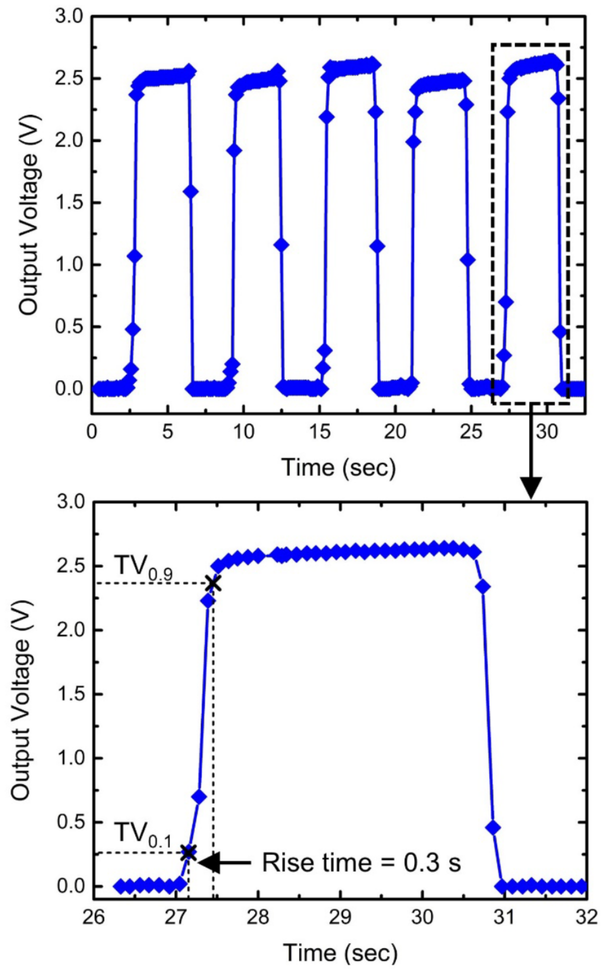

Figure 3.10 Response of a sensor pixel for repeated application of load shows repeatable results. The rise time is calculated to be 0.3 s.

To ascertain the repeatability of the sensor response, a sensor pixel was repeatedly subjected to a load of 500 g. The output voltage with respect to time is shown in Fig. 3.10. We can clearly observe that the response for a given load is uniform and repeatable. A similar true value (TV) of 2.55 V is observed for the output voltage. Further, the rise time for the sensor pixel is obtained as 0.3 s and the time constant of the sensor is 0.52 s, which is extremely fast for a sensor matrix primarily designed for human interactions. There are some variations in the response of different sensors in the sensor matrix due to the properties of the conducting material. The static and dynamic characteristics of a single sensor pixel are listed in Table 3.2.

Given the non-linear response of the sensor, the sensitivity has been calculated for applied pressure above 25 kPa for a bias resistance of 1 kΩ. The sensitivity of the sensor is much higher for lower values of load pressure, as seen in Fig. 3.8. The values of sensitivity and resolution have been calculated for the applied load above 25 kPa. All values reported are with a bias resistance of 1 kΩ.

Table 3.2 Characteristics of a Sensor Pixel

Characteristics	Value	Unit
Sensitivity	0.01	V/kPa
Resolution	0.488	kPa
Range	0-60	kPa
Rise time	0.3	s
Delay time	0.23	s
Fall time	0.17	s
Percentage Overshoot	1.6	%

3.6.2.2 Application

Typically, stroke victims are instructed to engage in exercises that include lifting and positioning a weight at a certain location. This facilitates the synchronized motion of muscles. Our device prompts an individual to position a weight in a specified location. For instance, when instructed to position the load on sensor 6, we may determine from the readings of sensor 6 and other surrounding sensors if the load was positioned with precision. For enhanced clarity, Fig. 3.11 displays heat maps that indicate the precise location of the object positioned on the pressure sensor matrix. The hue of the heat map corresponds to the magnitude of the output voltage. The experiment involved the placement of a weight weighing 0.5 kg, which took the form of a cuboidal box of 5 cm × 5 cm × 10 cm. The sensor matrix's response is unaffected by the shape of the item. The outcome is solely determined by the mass of the load. The sensor matrix has the capability to detect a load ranging from 0.02 kg to 10 kg, making it suitable for various activities, including the pressure sensor mat for patients. Additionally, by analyzing the temporal response, we can determine the duration it takes for an individual to both position and transport the load between two locations. In this approach, we can simply evaluate the activity of the patients and estimate their recuperation. Exercises can also be conducted and evaluated by instructing the individual to move an object along a designated path on a sensor. By analyzing the sensor's output values, we can determine whether the patient has accurately followed the prescribed path.

We developed a NN model and conducted training to accurately identify the location of the load on a sensor matrix. We utilized the NN to oversee the individual's reaction due to its simplicity, user-friendliness, and autonomous learning capabilities. The neural network assists us in verifying the accuracy of the load's placement by providing us with its coordinates. Additionally, it has the capability to acquire knowledge from an individual's reactions and behaviors over an extended duration. The neural network was provided with a training dataset consisting of 40 load points out of a total of 60, along with their corresponding output voltages. A total of twenty samples were employed for the purpose of validation. The architecture had an input layer, a hidden layer, and an output layer. The system consisted of 16 input channels that captured the output voltages from the sensor pixels, and two output channels that provided the x and y coordinates of the load. We conducted an analysis of the performance of several

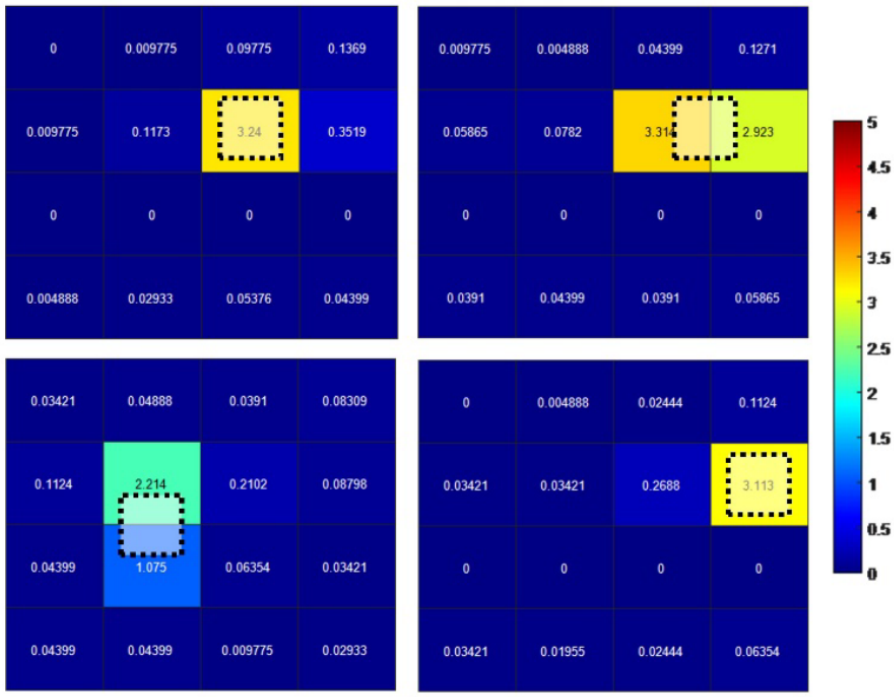

Figure 3.11 The heat map for a load (shown using a dotted square) placed on the sensor matrix clearly indicates the position of the load, which shows that the output of the sensor system can be used to predict load position. The color scale is in volts.

Table 3.3 Comparison of Network Architectures and Training Functions based on MSE

Network Architecture	Training Functions	Training Data	Validation Data
Feed Forward	Levenberg Marquardt	0.0924	0.8695
	Gradient Descent with Adaptive learn rate	1.0297	2.2401
	Gradient Descent	2.7847	3.4108
Cascade Forward	Levenberg Marquardt	0.9321	1.6851
	Gradient Descent with Adaptive learn rate	1.5108	2.1896
	Gradient Descent	2.9422	4.4556

training functions and their corresponding network designs. In each case, we estimated the mean square error (MSE), which is presented in Table 3.3.

From the table, we can see that the least MSE is given by the Levenberg-Marquardt (LM) training algorithm in feed-forward network architecture. LM training algorithm is suitable to use when the dataset is less in number. It gives the highest speed compared to other training functions, and thus, it was selected for training and testing.

We compared the results of the neural network with a mathematical model (MM) used to estimate the coordinates of the load. We calculated the weighted average of the coordinates of the sensors as follows:

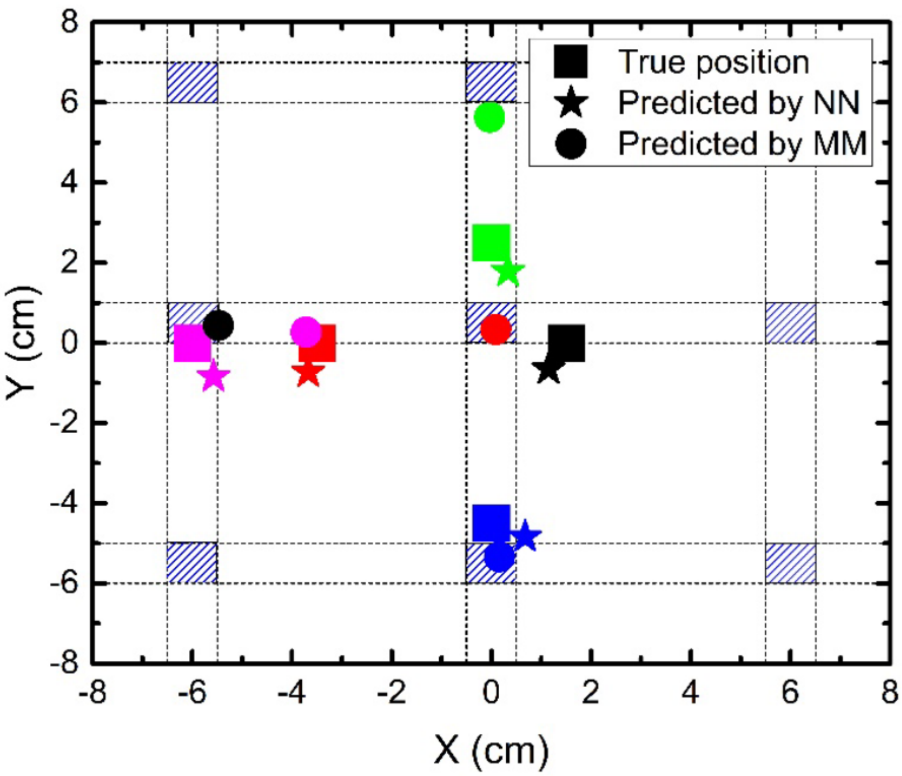

Figure 3.12 The position of the load as predicted by the trained neural network (stars) and the mathematical model (circles) compared to the actual position of the load (squares) indicates the accuracy of the neural network. The black dotted lines indicate the position of copper electrodes, while the blue hashed squares are the individual sensor pixel. Corresponding values are represented using the same color.

$$x = \frac{\sum_{i=1}^{16} C_i V_i}{\sum_{i=1}^{16} V_i} \tag{3.2}$$

where C_i represents the vector coordinates of the location of sensors, and V_i denotes the corresponding output voltage. By performing the mathematical analysis, we found the position of the load and calculated the mean distance error. The mathematical analysis gives a mean error of 0.704 cm, and the NN gives a mean error of 0.103 cm for the validation data. The mathematical analysis is effective for ideal sensors; however, it cannot handle the non-idealities present in a practical sensor system. On the other hand, the NN handles the non-idealities present in the sensor, learns from the inputs, and also helps in predicting future outcomes. The true position of the load, the position predicted by the neural network and, the position predicted by the mathematical analysis are shown in Fig. 3.12. We presented only 5 out of 20 positions of validation data on the graph for clear visualization. We can see that when

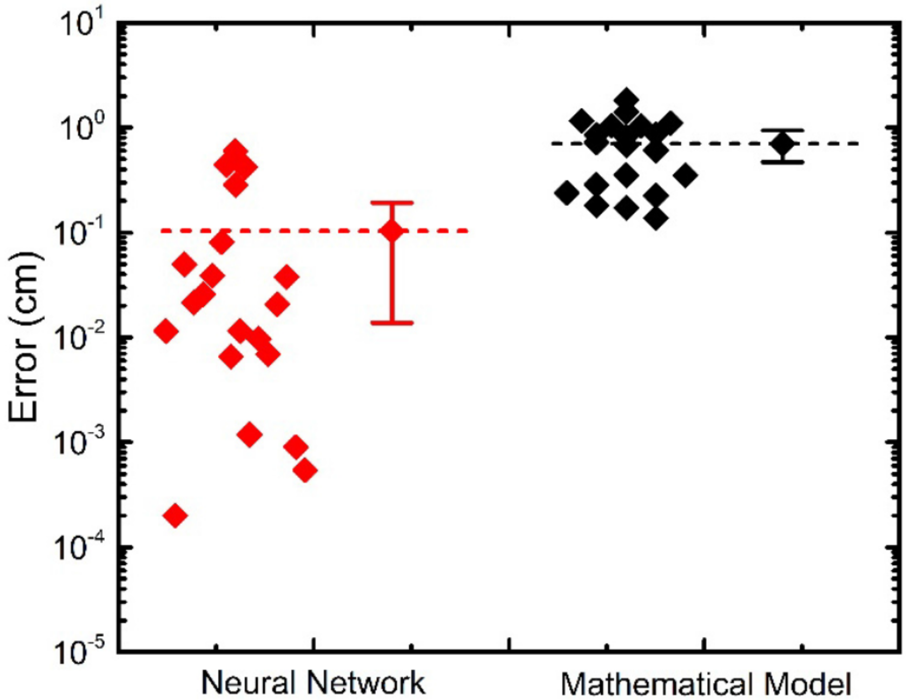

Figure 3.13 Scatter of error values for all the 20 data points in the validation set, for neural network (NN) and the mathematical model (MM) indicates the superior performance of the trained neural network at predicting the load position. The dotted lines indicate the mean error, while whiskers indicate standard deviation.

compared to analytically obtained load positions, NN's predictions are closer to the true value. Fig.3.13 shows the error scatter plot that represents the frequency of errors using neural networks and mathematical modeling. From the graph, we can conclude that the results obtained using neural networks have fewer errors and are more reliable.

3.6.3 Evolution of pressure sensor mats from 4 x 4 array

The design of the sensor array has evolved significantly, transitioning from a single pressure sensor to a 4×4 sensor configuration to a 32×32 sensor array design. The initial 4×4 sensor array was constructed with paper as the upper and lower layers. While this technology has its uses in specific contexts, it is not suitable for creating a large-scale sensor matrix. Subsequently, we conducted trials using various materials to determine the optimal protective upper and lower layers for the sensor array. Initially, we experimented with pliable polypropylene sheets. The surfaces of the seats were coarse, which could cause discomfort for individuals when seated. Subsequently, we endeavored to create the sensor array utilizing translucent plastic sheets. The issue arose from the visibility of the underlying electrode layers through the translucent sheets, which were aesthetically displeasing. Finally, we experimented with polyvinyl chloride (PVC) sheets, which proved to be an ideal pliable material for constructing the

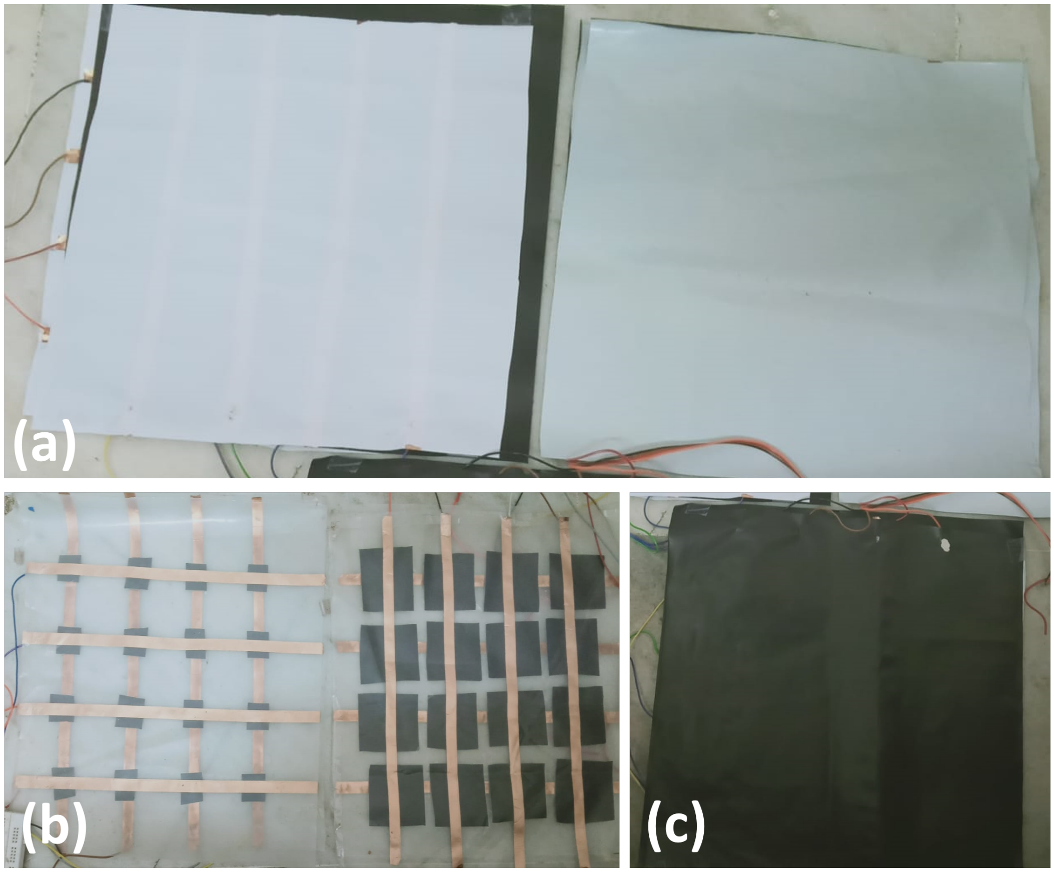

Figure 3.14 Evolution of the design of the sensor array (a) and (c) 4 × 4 sensor array using polypropylene (b) 4 × 4 sensor array using transparent plastic sheets

sensor array. We tested all these materials by designing a 4 × 4 sensor configuration with the same specifications as discussed in the previous section.

Following the material selection, we proceeded to create a sensor array of 16 × 16. Each sensor pixel has dimensions of 10 mm × 10 mm, with a pitch of 10 mm. The sensor array dimensions were insufficient to accurately perceive the individual's body position. Since the microcontroller will not have so many input and output pins, we used multiplexers to read the sensor response of each pixel. We used two multiplexers/demultiplexers, one for the horizontal set of copper electrodes and another for the vertical set of copper electrodes. The vertical set of copper electrodes are connected to a demultiplexer, and the horizontal set of electrodes are connected to the multiplexer. The demultiplexer was connected such that it would select the line to be on high voltage, and the multiplexer reads all the 16 sensor pixels on that particular line (which is on high voltage). This is called raster scanning.

After testing with the breadboard, we designed a PCB to get reliable and accurate response. The PCB was connected at the top and right side of the sensor mat (Fig. 3.16).

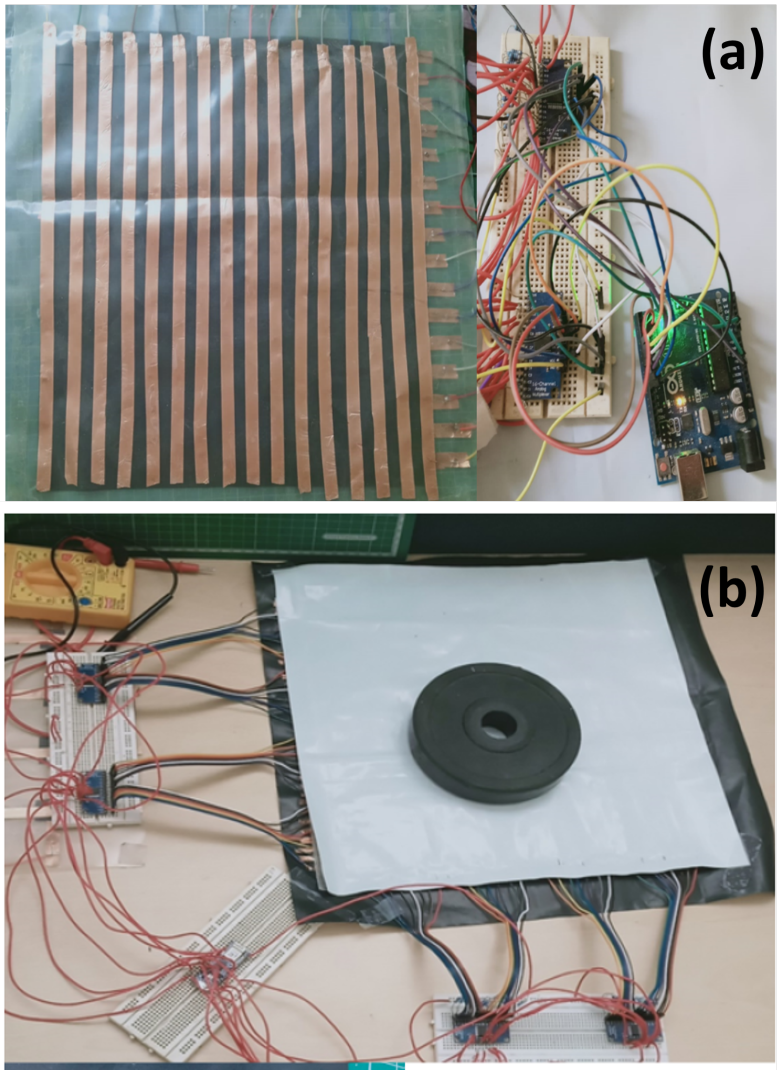

Figure 3.15 Evolution of the design of the sensor array (a) 16 × 16 sensor array (b) 32 × 32 sensor array

To make our sensor mat completely designed by the PCB manufacturers we designed our complete sensor design on Altium for PCB fabrication as shown in Fig. 3.17. This design didn't work as the thickness of the sensor pad was very less, and we couldn't get right pressure distribution

Subsequently, we enhanced the resolution and devised a sensor array measuring 32 × 32 by hand following our previous procedure. When we designed a 32 × 32 sensor array, we selected the sensor pixel of size 5 mm and a pitch of 4 mm. The sensing area of the mat was 28.4 cm × 28.4 cm. The dimensions of the overall mat were not enough for a person to stand on it comfortably, so we designed another prototype with larger dimensions.

Fig. 3.14, Fig. 3.15, Fig. 3.18 shows the pictures of the evolution of the design from a 4 × 4 to 32 × 32 sensor array. Fig. 3.14a and c shows the 4 × 4 sensor array designed using polypropylene as the top

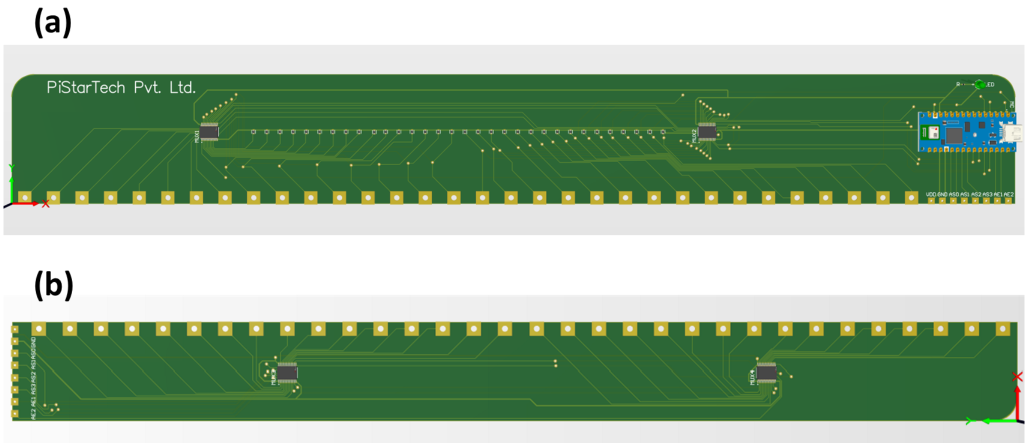

Figure 3.16 PCBs designed for the 32 × 32 sensor mat (a) connected on the top of the mat (b) Connected on the right side of the mat

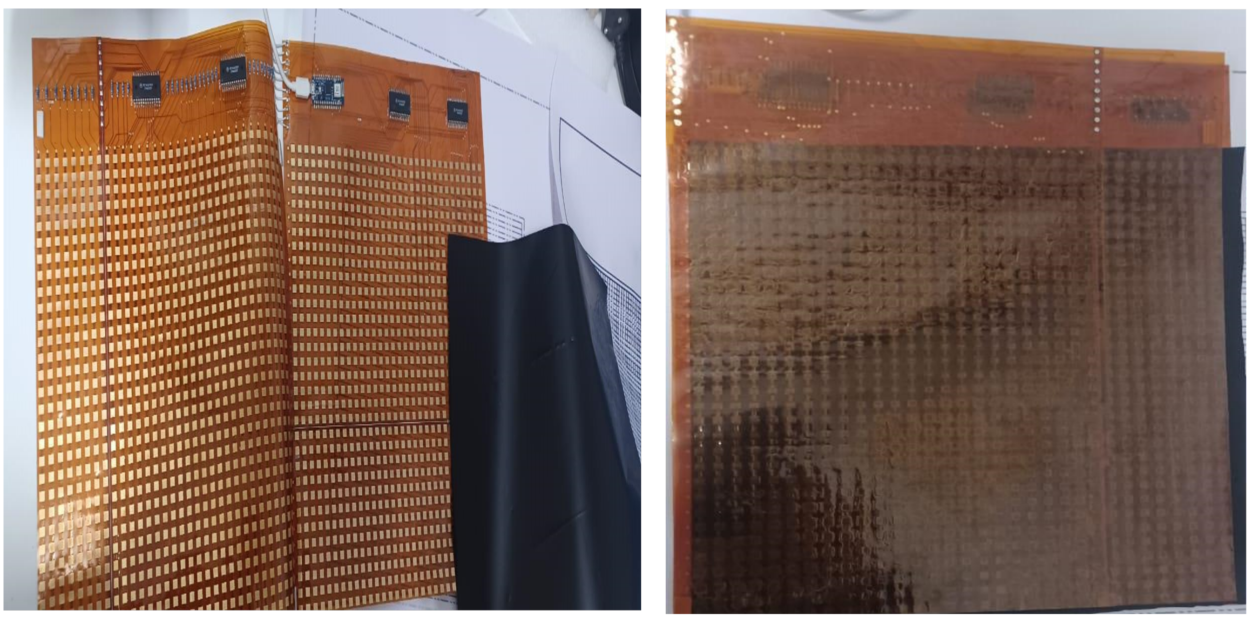

Figure 3.17 Printed 32 × 32 sensor mat

and bottom protective layer. Fig. 3.14b shows the 4 × 4 sensor array designed using translucent plastic sheets as the top and bottom protective layer. Fig. 3.15a shows the 16 × 16 sensor array designed using translucent plastic sheets as the top and bottom protective layer. Fig. 3.15 (b) shows the 32 × 32 sensor array designed using PVC sheets as the top and bottom protective layer. Fig. 3.18 shows the 32 × 32 sensor array with the PCB inside the mat.

We observed good results related to pressure distribution in 32 × 32 sensor array. In this prototype model of the sensor mat, since the rigid PCB is inside the sensor mat, it will be uncomfortable for the

Figure 3.18 32 $\times$ 32 sensor array using rigid PCBs

user to sit on the chair. In the final version, we designed the sensor mat using a flexible PCB such that the complete data acquisition circuit is outside the sensor mat in a box that can be attached at the back or below the chair. The final design of the sensor mat for the smart chair is discussed in Chapter 6.

The next section presents the sensor mat design of a 32 $\times$ 32 sensor array for designing a podia scanner or foot pressure monitoring system.

3.6.4 Design of a large (32 x 32) sensor array

3.6.4.1 Sensor Design and Fabrication

The pressure sensor mat comprises three layers, as depicted in Fig. 3.20a. The upper and lower layers consist of sheets made of Polyvinyl chloride (PVC) with copper electrodes arranged horizontally and vertically, respectively, creating a crossbar structure as depicted in Figure 2.11.b. The intermediate stratum consists of a piezoresistive polymer called velostat. It has a thickness of 106$\pm$1 μm, while the PVC sheets have a thickness of 169$\pm$1 μm. This gives a combined thickness of approximately 444 $\pm$ 1μm, as measured using a Mitutoyo micrometer. This makes the structure incredibly flexible. We have constructed a 32 $\times$ 32 sensor array resulting in 1024 sensor pixels.

We have observed that the minimum granularity or the distance between the two sensor pixels should be one more than the thickness of the dimension of the sensor pixel. If the dimension of the copper tape (that makes the sensor pixel) is x mm, then the spatial resolution or the distance between the copper

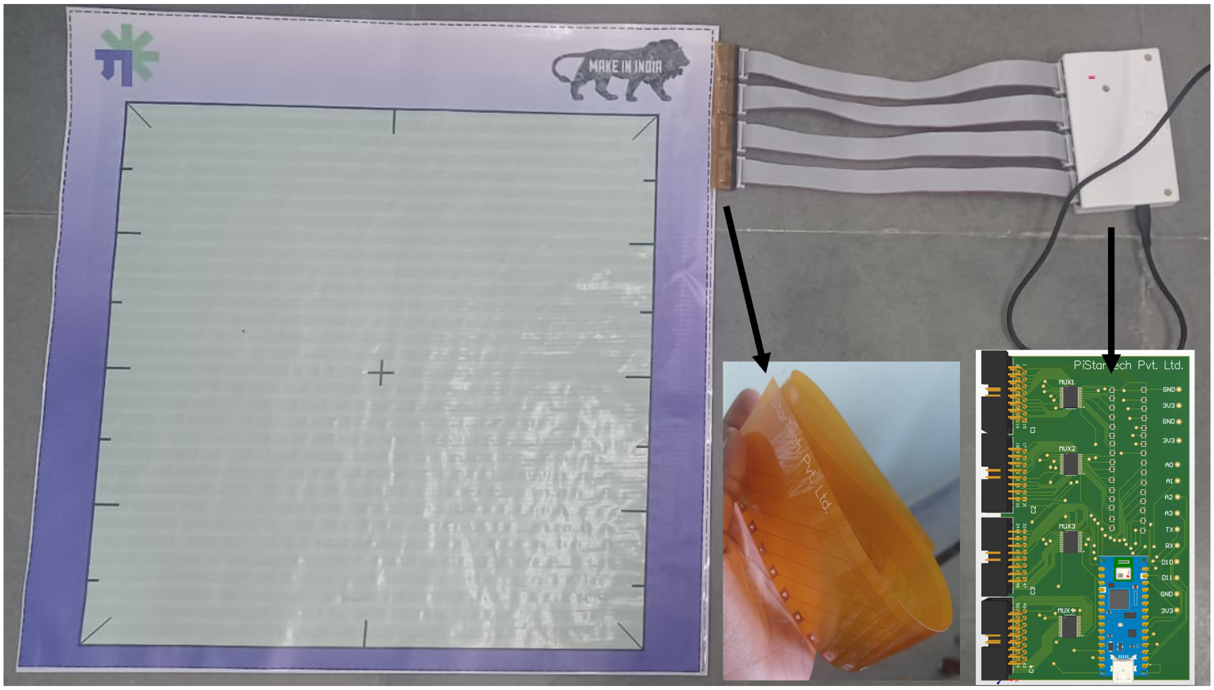

Figure 3.19 Final design of a 32 $\times$ 32 sensor array using flexible PCBs and the data acquisition circuit in a black box

tapes must be greater than or equal to $x+1$ mm. In our case, we have taken the width of copper tape as 6 mm, which makes the sensor pixel of size 6 mm $\times$ 6 mm, and the distance between the sensor pixels is 7 mm. We have conducted an experiment by designing a 2 $\times$ 2 pressure sensor with different spatial resolutions of 4 mm, 5 mm, 6 mm, 7 mm, and 8 mm and observed that if we apply pressure to one sensor pixel, we can observe a noticeable change in the other sensor pixels surrounding the pixel under test due to crosstalk. This crosstalk was negligible for 7 mm and 8 mm spatial resolutions. Hence, we concluded that the distance between the sensor pixels must be greater than or equal to x+1 mm and selected 7 mm as our spatial resolution.

The image of the entire pressure sensor mat is shown in Fig. 3.19. The operating concept of the sensor pixel is based on the variation of resistance of the polymer composite due to the applied pressure. The fabrication technique of the mat includes gluing the copper electrodes on the PVC sheets and attaching them to the planned PCB. Next, the velostat is positioned between the PVC sheets, and the three layers are then securely bonded. The entire fabrication process can be expedited and does not require any clean room facilities.

3.6.4.2 Application: Foot Pressure Monitoring using Sensor Mat

Plantar pressure analysis is a primary method used in biomedical assessment to evaluate posture, walking, and other activities. An analysis of the distribution and intensity of pressure might yield valuable insights for diagnosing or predicting the likelihood of foot illnesses or impairments. Plantar

Table 3.4 Specifications of the sensor array for podiascanner

Technology	Piezoresistive
Number of Sensor pixels	1024
Sensor area	28.8 cm $\times$ 28.8 cm
Total Area	30 cm $\times$ 30 cm
Spatial resolution	4 mm
Thickness	0.5 mm
Material	PVC
Connectivity	Wired
Weight Range	40-120 kg

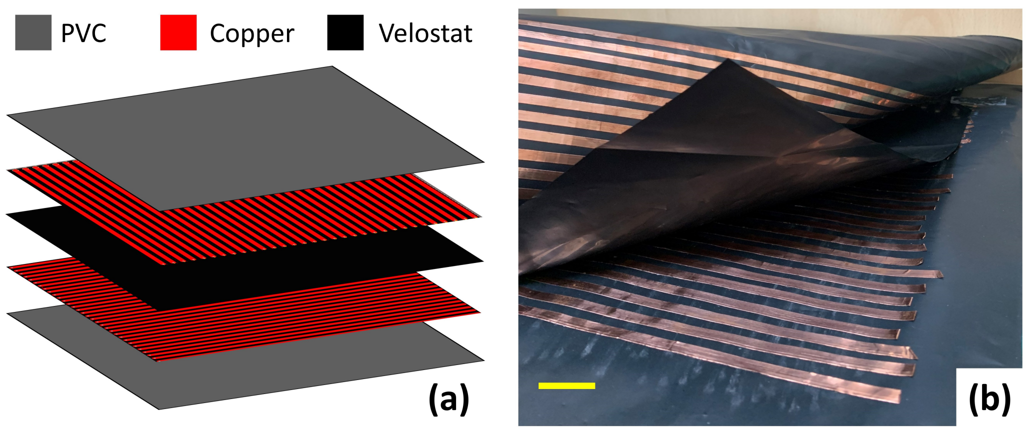

Figure 3.20 (a) Design of the flexible pressure sensor matrix with three layers, (b) Photograph of the fabricated pressure sensor matrix showing the three flexible layers. Scale bar in (b) is 3 cm.

pressure refers to the force exerted between the foot and the surface it is in contact with during regular activities including movement. [102]. Extensive study and development have been conducted in the field of plantar pressure measuring in recent decades. The development of pressure sensing technology has been significantly shaped by a desire to understand the pressure exerted by the feet during human movement [103]. Foot diseases can have a detrimental impact on foot function, which in turn can alter the way a person walks, significantly affecting their overall quality of life [104]. An analysis of an individual's pressure distribution data can help identify potential issues that, if left addressed, may increase the risk of developing or exacerbating a plantar surface injury caused by excessive pressure in specific parts of the footc [105, 106]. Information from these measurements have provided essential support in the assessment of various foot pathologies and disorders, including rheumatoid arthritis [107–109], Parkinson's disease [110–113], diabetic ulcers [114–117], plantar fasciitis [118, 119], identifying flat foot patients [120], prescribing customized footwear design [121–123], and in analyzing sport biomechanics [124], for injury prevention and other applications.

Table 3.5 Specifications of the sensor array for smart chair

Technology	Piezoresistive
Number of Sensor pixels	1024
Sensor area	41.5 cm × 41.5
Total Area	50 cm × 50 cm
Spatial resolution	7 mm
Thickness	0.5 mm
Material	PVC
Connectivity	Wired
Weight Range	40-120 kg

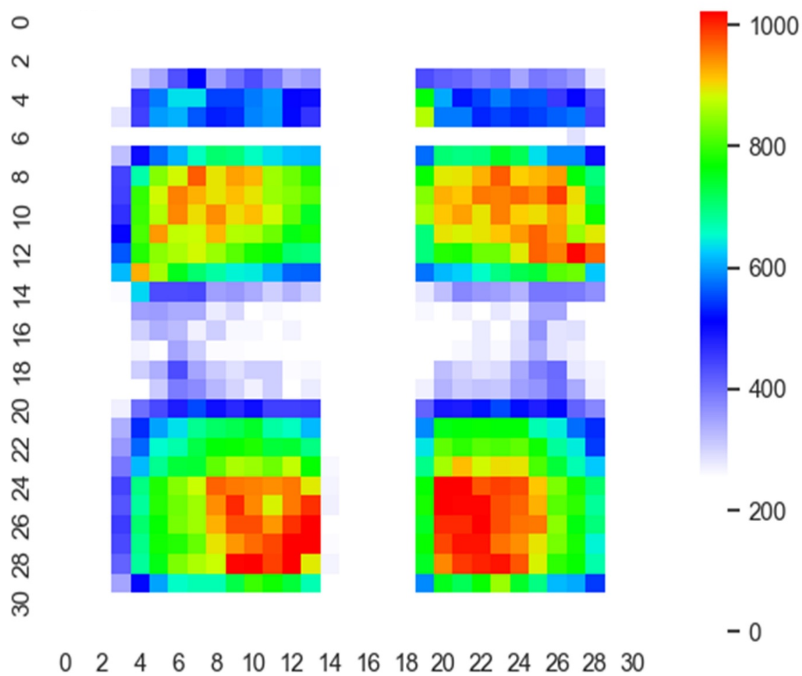

Figure 3.21 Heat map showing the foot pressure distribution of a healthy subject of weight 72 kg.

The pressure sensor array, consisting of 1024 sensors, is linked to a microcontroller that has a built-in analog-to-digital converter (ADC) for the purpose of acquiring and processing data. The microcontroller applies a high voltage to the row input and successively measures the voltage across the bias resistors for all 32 columns. The process is replicated for each of the 32 rows in order to acquire the entire 1024-pixel analog data. In order to minimize the need for a large number of analog input pins on the microcontroller, we have employed multiplexers to retrieve the voltage readings. The data can be shown using a heat map that displays the output voltage of each sensor. This voltage has been measured and divided into 1024 levels (2^{10}) using a 10-bit ADC in the microcontroller.

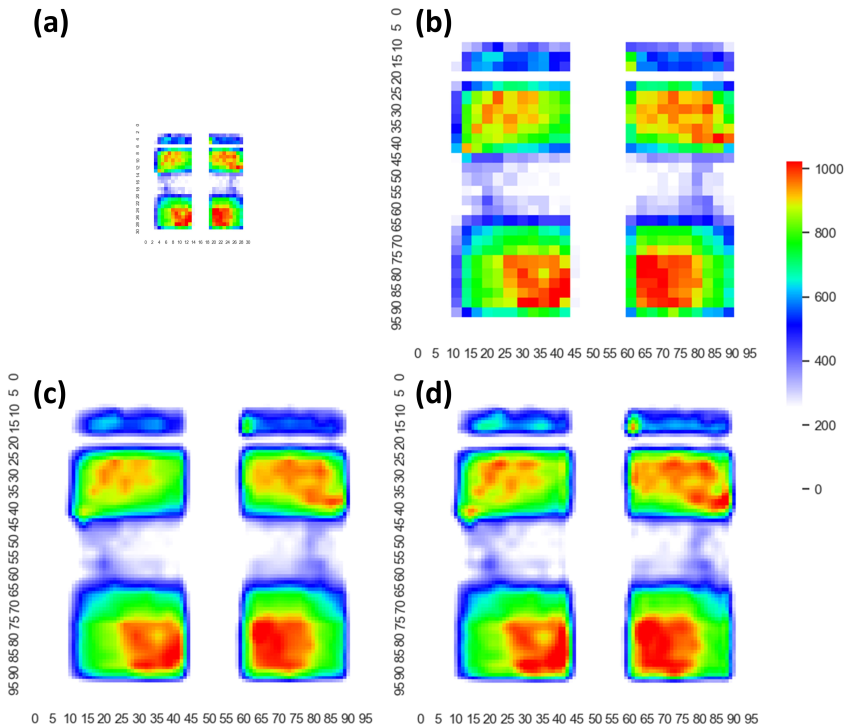

Figure 3.22 (a) Original foot pressure distribution of 32 × 32 array. Interpolated images of 100 × 100 pixels using (b) Nearest Neighbour Interpolation Technique (c) Bilinear Interpolation Technique (d) Bicubic Interpolation Technique. The linear scale for the pixels is kept the same to show the image enlarging.

Fig. 3.21 shows the pressure distribution of the foot of the person standing on it. The subject has a weight of 72 kg and a height of 176 cm. The person has a normal plantar distribution with no foot problems. In Fig. 3.21, we can see that the image of the footprint is not smooth. To provide a more detailed representation of the pressure distribution data of the foot, we are employing proven interpolation algorithms to increase the pixel count. Interpolation is a technique employed to enhance the pixel density of an image by calculating the missing values between the known pixel values.

Various interpolation algorithms can be utilized for image improvement. The primary categories of non-adaptive interpolation techniques include nearest neighbor, linear, and cubic interpolation. Using interpolation, we have transformed the data from a 32 × 32 sensor array into a 100 × 100 image representing pressure distribution.

In the nearest neighbor interpolation procedure, we assign the unknown pixel with the value of the nearest known pixel [125]. The Bi-Linear interpolation algorithm utilizes linear interpolation in two dimensions by calculating weighted averages of the adjacent pixels [125]. The procedure is straightforward and yields a more polished outcome, although it may not be optimal for achieving sharp transitions [125]. Bi-cubic interpolation is frequently preferred over bi-linear or nearest-neighbor interpolation for image re-sampling. The improved image quality is achieved by utilizing a polynomial

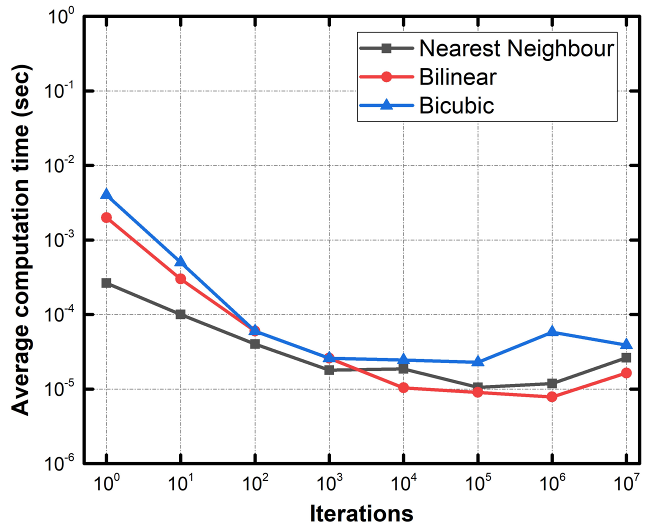

Figure 3.23 Average computation time versus iterations of different interpolation algorithms show that bicubic interpolation takes the longest time.

interpolation of 16 pixels (4×4), as opposed to the bilinear interpolation technique which only examines linear interpolation of the nearest 4 pixels (2×2) to calculate the values of unknown pixels. They have conducted a comprehensive analysis and comparison of various adaptive and non-adaptive image interpolation methods, focusing on their primary performance metric, namely Peak Signal-to-Noise Ratio (PSNR). They observed that bicubic interpolation outperformed other non-adaptive interpolation techniques in terms of PSNR [125]. Figure 3.22a illustrates the distribution of foot pressure in a normal feet using a 32×32 array of pixels. Fig. 3.22b, 3.22c and 3.22d display the distribution of foot pressure following the use of nearest neighbor, bilinear, and bicubic interpolation approaches, respectively. The linear pixel scale remains unchanged to demonstrate the impact of image enhancement and enlargement using interpolation. An objective assessment of the photographs indicates that the image contour for the nearest neighbor interpolated image is indistinct. The image obtained using bilinear interpolation exhibits improved clarity, albeit it lacks sharpness. On the other hand, the image resulting from bicubic interpolation has sharper edges, reduced pixelation, and superior image quality in comparison to the other methods.

In order to determine the processing time employed by various interpolation strategies, we executed the algorithm a total of 10 million times. The extensive repetition was necessary to mitigate interference from concurrent background processes associated with the computation, such as file read/write operations. Fig 3.23 displays the mean duration required to process the image following n iterations. It is evident that when we increase the number of iterations, the average processing time for a single conversion is approaching a stable value. The mean processing times were 20.89 μs, 21.61 μs, and 38.38 μs for the nearest neighbor, bilinear, and bicubic interpolation approaches, respectively. Because the refresh rate, i.e, the rate at which the data on heat map is changing dynamically is 195 ± 25 ms, the adoption of an interpolation technique, with such a small computation time, does not impact the overall timing of the device considerably. Despite the increased processing time, we have noticed that bicubic interpolation yields superior image quality.

3.7 Summary

In this Chapter, we discussed about the very important part of the smart chair system i.e. the design and fabrication of a pressure sensing system. We first discussed about the types of pressure sensors and the reason for selecting a piezoresistive pressure sensor for our system. Secondly, We explored the feasibility of fabricating a smaller (4×4) flexible pressure sensor matrix using paper as a structural material and developed a paper-based piezoresistive pressure sensor. The major advantage of using paper is its low cost, ease of fabrication and high flexibility. We have also presented the static and dynamic characteristics of the sensor. Though, there is a variation in response of different sensors in the sensor matrix due to the properties of the conducting material, it can be effectively used in applications for recognizing activity and assessing the recovery of the stroke patients by performing various exercises on the pressure sensor mat. We also analyzed the performance of the sensor matrix by training a neural network to detect the position of a load based on the individual sensor values. The load position predicted by the neural network was compared to a mathematical model and was found to be more accurate.

In the next part, we discussed about the evolution of our design from 4×4 to a 32×32 sensor matrix. We also presented the application of using the sensor mat for foot pressure monitoring. We have implemented an interpolation method for deriving an extended pressure map which provides us with a more detailed understanding of the plantar pressure distribution. The piezoresistive flexible pressure sensor (FLEPS) mat with 1024 pixels covers a total area of 1089 cm^2 and sensing area of 806.56 cm^2. It can measure upto a maximum pressure of 100 kPa and cover a weight range of 10-100 kg. It also provides dynamic pressure distribution of the feet when the person walks over it thus providing us with useful gait information. By increasing the size of the mat, it can be used in hospital beds for preventing the risk of getting bedsores which will be very beneficial for bed-ridden patients.

Chapter 4

Characterization of the Pressure Sensing System

4.1 Publication History

This chapter contains excerpts from the following publications: [55, 72, 126, 127]

- **Anis Fatema**, I. Kuriakose, D. Devendra, A. M. Hussain, "Investigation of the Mechanical Reliability of a Velostat-Based Flexible Pressure Sensor," in proceedings of 2022 IEEE International Conference on Flexible and Printable Sensors and Systems (FLEPS) pp. 1-4, 2022.

- **Anis Fatema**, S. Chauhan, M. Datta, Aftab M. Hussain, "Investigation of the Long-term Reliability of a Velostat-based Flexible Pressure Sensor Array for 210 Days", submitted in IEEE Transactions on Device and Materials Reliability, 2023.

- S. Chauhan, Ivin Kuriakose, **Anis Fatema**, A. M. Hussain, "Efficient Calibration Of Velostat-Based Flexible Pressure Sensor Matrix", in proceedings of *2023 IEEE International Conference on Flexible and Printable Sensors and Systems (FLEPS)*, 2023.

- M. Datta, L. Lakhmanan, **Anis Fatema**, A. M. Hussain, "Characterisation and Quantification of Crosstalk on a Velostat-based Flexible Pressure Sensing Matrix", *2023 IEEE International Conference on Flexible and Printable Sensors and Systems (FLEPS)*, 2023.

4.2 Introduction

Prior to implementing sensors in real-time applications, it is crucial to conduct several experiments and examine the sensor's distinct properties. In the preceding chapter, we developed the pressure-sensing array. In the current chapter, we will discuss various studies and experiments conducted on the mat to verify its ability to produce an effective output. Firstly, we will be covering the crucial aspect of sensor design, which is calibration. Next, we will show the various studies conducted, including the cross-talk analysis, mechanical reliability assessment, and long-term reliability testing spanning a duration of 210 days.

4.3 Calibration

Calibration is an essential aspect for ensuring that any sensor generates accurate, dependable, and consistent outcomes. Prolonged application of pressure can cause deformation in the microstructure of velostat, leading to a time-dependent change in sensor response and rendering the sensor unreliable. Therefore, it is crucial to calibrate the sensor based on velostat in order to ensure its reliability. The mathematical model proposed by Zhang et al. [128] describes the time-dependent relative resistance of conductive polymer composite materials as:

$$\frac{R_t}{R_0} = f(\sigma, D, \theta, \varphi, \varepsilon_0, \psi, n) \tag{4.1}$$

where R_t is the instantaneous resistance at the applied time, R_0 is the original resistance, σ is the applied pressure, D is the nominal diameter of the filler particles, θ is the filler volume fraction, φ is the potential barrier height, ε_0 is the original strain, ψ, and n are constants related to the creep behaviors in the material [128]. In a given velostat thin film, since D, θ, φ, ε_0, ψ, and n are fixed, the relative resistance will be related only to the pressure applied, i.e., σ. Then, the resistance of the velostat material at any given time t can be given as follows:

$$\frac{R_t}{R_0} = f(\sigma) \tag{4.2}$$

We have seen that the resistance of velostat approximately follows an inverse exponential relationship with respect to applied weight.

$$R_t = \frac{a}{W^b} \tag{4.3}$$

where a and b are constants and W is the applied weight. To calibrate the sensors, we need to find the two parameters, a and b, for every sensor pixel. For sensor systems that are subjected to static or dynamic flexing, it is essential to determine the variation of these parameters during and also after bending. For the reliability of sensors, it is expected that the values of a and b remain constant or vary predictably with usage.

Hence, the output voltage can be written as

$$V_o = \left(\frac{R_b}{R_b + \frac{a}{W^b}} \right) V_{in} \tag{4.4}$$

The calibration of this sensor configuration presents three major calibration challenges. First, 1024 sensors require 2048 parameters (a and b for each sensor), which are calculated after making $1024 \times 12 = 12,288$ measurements for calibration, which is impractical for even a small-scale product. Second, accurate placement of weights on a single sensor without distributing the weight to any other sensor is a very painstaking process. We noticed that even 1 mm of shifting of the load-bearing area affects results significantly. Third, the obvious approach of using a large flat surface to uniformly distribute weight on the sensor matrix and reading values from individual sensors does not yield accurate calibration characteristics as there is directional crosstalk, i.e., crosstalk between columns but not between rows [126].

4.4 Characterization of the Sensor Array

4.4.1 Cross Talk Analysis

Due to the multidirectional conductivity, i.e., the normal and transversal conductivity exhibited by velostat, the application of these materials in sensor arrays becomes complicated [91]. When pressure is applied to one sensor pixel of the array, not only is there a change in resistance at that point but also at some adjacent points or sensor pixels. This phenomenon is known as crosstalk, which is particularly high for continuous thin films of velostat and for electrodes in crossbar architecture. It originates from the electrical and mechanical responses of the sensor [129]. The mechanical cross-talk occurs due to the non-ideal force diffusion of the velostat on the application of pressure [130]. The electrical cross-talk is due to the fact that the current flows not only through the target sensor pixel but also into the adjacent sensor pixels. In order to eliminate or reduce the effect of crosstalk, it is important to quantify it. We designed an algorithm to characterize the crosstalk and calculate their mean. We only consider the adjacent sensor pixels of the center pixel under test (PUT). We weigh the output of each of the neighboring pixels (laterally and diagonally) according to their distance from the PUT. Thus, we have defined the crosstalk value at each pixel as the normalized sum of the pressure reading at neighboring pixels weighted by their distance [131].

$$CT = \frac{\displaystyle\sum_{i \in n - \{s\}} d_i p_i}{p_0 \displaystyle\sum_{i \in n - \{s\}} d_i} \tag{4.5}$$

where p_0 is the pressure value of the PUT, and p_i and d_i are the pressure value and distance of the neighboring pixels. As the neighboring pixel readings will always be less than that of p_0, this parameter

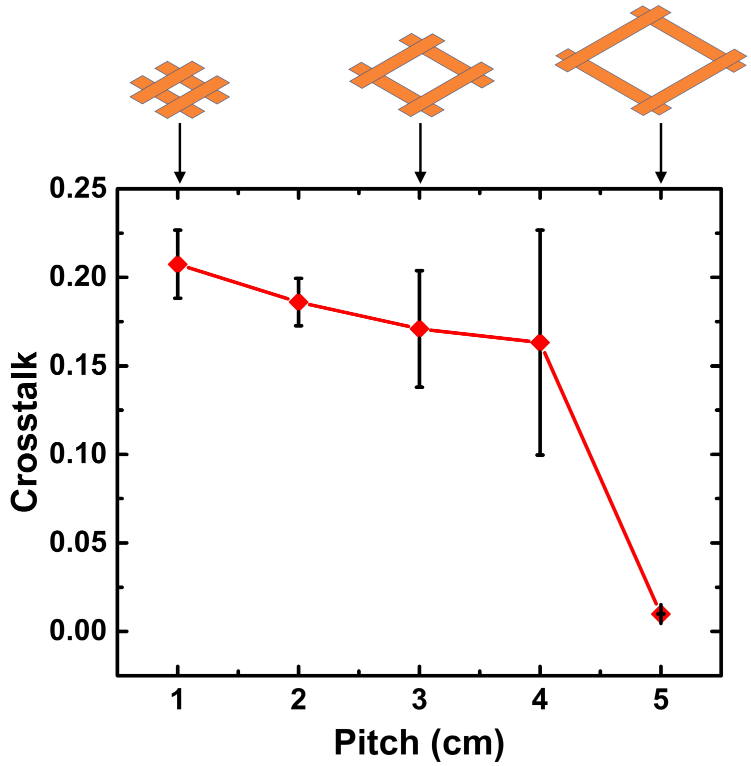

Figure 4.1 The mean crosstalk decreases as the pitch length increases. The error bars shows the standard deviation in the crosstalk values. The diagrams at the top are to scale in terms of electrode width and pitch.

will be a dimensionless value between 0 and 1. This equation can be used for any size of the matrix and considering any size for the neighborhood of the pixels, allowing the general structure of the measure to remain consistent.

An examination of crosstalk is crucial in determining the pitch length throughout the sensor array design process. The pitch length refers to the spatial separation between the individual sensor pixels. The experiment was conducted by creating a 3×3 sensor matrix, where each pixel had dimensions of 1 cm $\times$ 1 cm. We have sliced a rectangular acrylic block of 1 cm $\times$ 1 cm with a thickness of 2 mm. This block is intended to be positioned over the sensing area of an individual sensor pixel in order to exert pressure on it. We applied a load of 1 kg to each individual sensor pixel and documented the reaction of all 9 sensor pixels. We analyzed the output response 10 s after applying the weight in order to obtain a consistent and steady output. The experiment was replicated using pitch lengths of 1 cm, 2 cm, 3 cm, 4 cm, and 5 cm. Our observation confirms that there is a decrease in crosstalk as the pitch length increases, as anticipated. Fig. 4.1 illustrates the variation in the average crosstalk as the pitch distance increases. The average crosstalk values for the pitch lengths of 1 cm, 2 cm, 3 cm, 4 cm, and 5 cm were 0.21 ± 0.02, 0.19 ± 0.01, 0.17 ± 0.03, 0.16 ± 0.06, and 0.00100 ± 0.00008, respectively. We observe that the standard deviation from 1 cm to 4 cm varies and drops suddenly for 5 cm pitch length. This may be because the

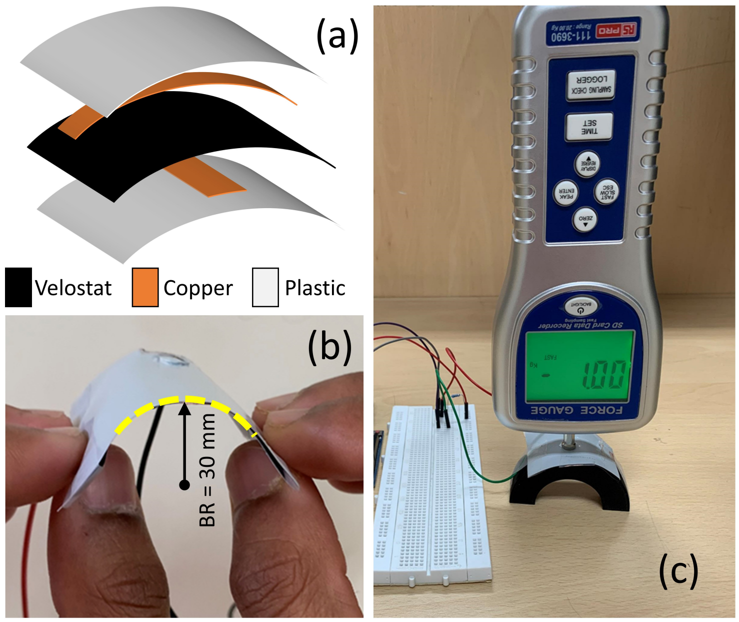

Figure 4.2 (a) Design of a sensor using a sheet of velostat sandwiched between two sheets made of plastic with cross-bar copper electrodes, (b) Photograph of a fabricated sensor showing its flexibility. (c) Experimental setup showing measurement of force applied on pressure sensor with the help of a push-pull force gauge, when placed on a curved surface.

sensor array includes both mechanical and electrical crosstalk, and for pitch lengths of 1 cm to 4 cm, both factors have an effect on it variably. However, when the pitch length increases to 5 cm, the electrical crosstalk drops greatly compared to mechanical crosstalk, and hence, we can observe an overall drop in the standard deviation. Therefore, we chose a pitch distance of 5 cm to conduct reliability testing on the sensor matrix. We opted for a larger pitch to mitigate the potential interference of crosstalk on the sensor's response during reliability testing. Alternatively, it is possible to create sensor arrays with a reduced pitch gap. However, this would necessitate precise calibration of the sensor array under various settings, as well as the utilization of sophisticated algorithms for data analysis and processing [132]. Addressing these challenges will expand the potential uses of velostat, particularly in the fields of bio medicine and healthcare.

4.4.2 Mechanical Reliability

In this section, we present a systematic study to understand the influence of repeated mechanical stress on the characteristics of a velostat-based resistive pressure sensor. We present the effect on the response of the sensor after being subjected to 150 bending cycles for up to 16 hours. This will help us understand whether it can be used on chairs with cushions since the sensor array will be bending in particular areas. The velostat-based pressure sensor was fabricated by sandwiching a velostat sheet between two plastic sheets along with top and bottom layers of copper electrodes in a crossbar architec-

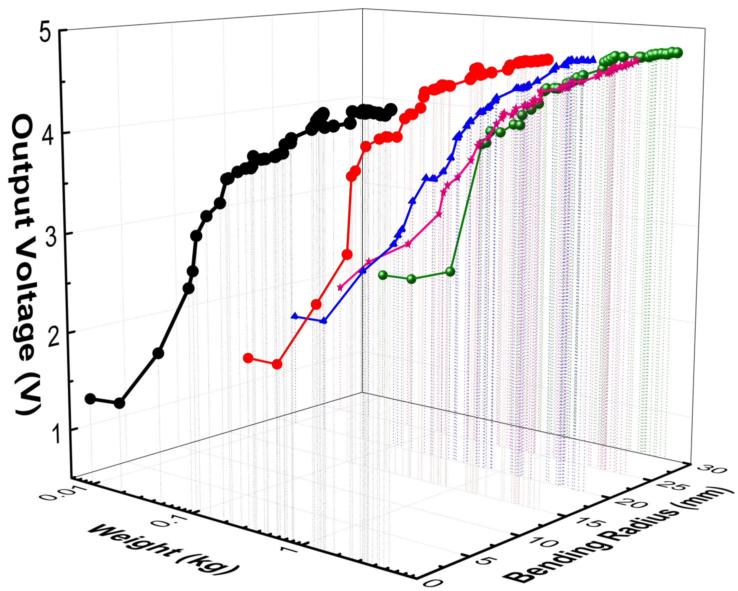

Figure 4.3 Output voltage for a sensor pixel for different applied loads, at various bending radii.

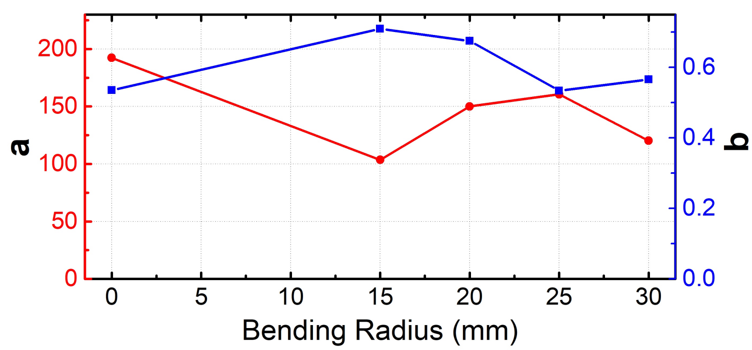

Figure 4.4 Variation of parameters a and b with different bending radii.

ture, as shown in Fig. 4.2a. The sensor pixel dimensions were 10 mm $\times$ 10 mm. In order to determine the influence of pressure on the velostat resistance, a setup with push-pull force gauge (maximum load - 200 N) was designed as shown in Fig. 4.2c. We made 4 samples of pressure sensor for testing it with different bending radii of 15 mm, 20 mm, 25 mm, and 30 mm. For the third experiment, we made 4 new samples to test the dynamic response for different bending radii. We made another sample of pressure sensor for repeatability testing. Hence, 9 samples of pressure sensors were fabricated for the complete testing of mechanical reliability.

The initial trial involved recording the sensor's reaction on a level surface. The sensor responses were recorded on curved surfaces with varying bending radii of 15 mm, 20 mm, 25 mm, and 30 mm. The purpose of designing 3D printed blocks was to regulate the degree of bending and the number of bending repetitions. The measurements' findings are displayed in Fig. 4.3. It is evident that when the

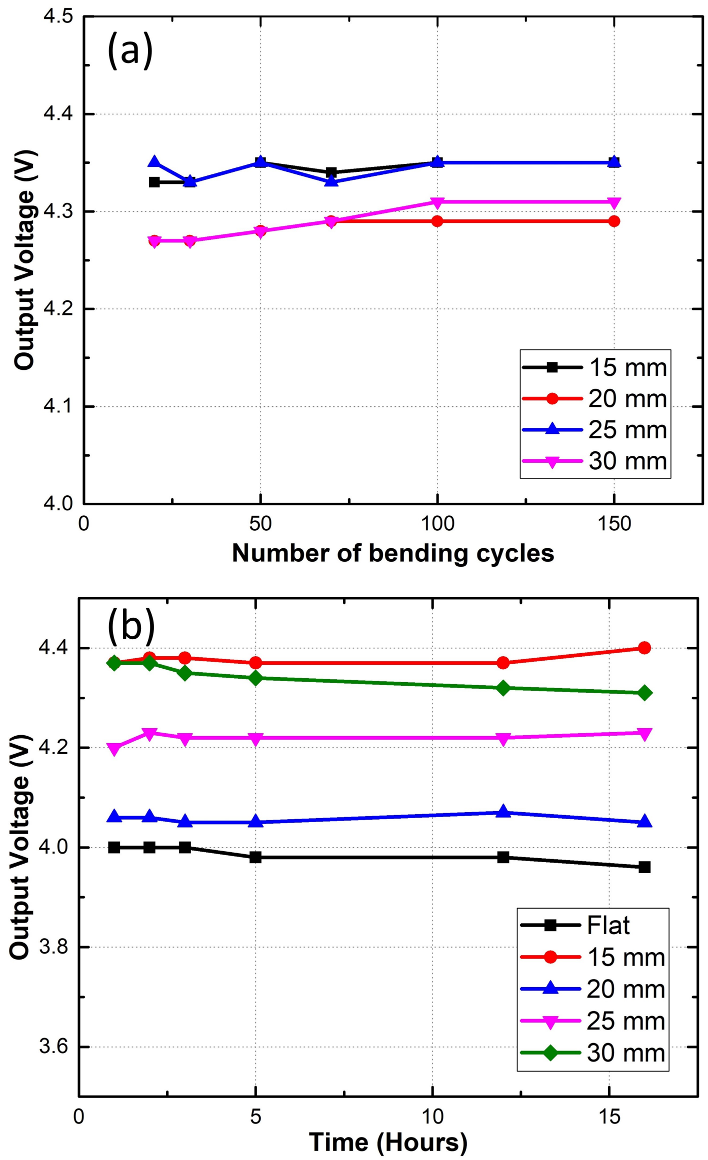

Figure 4.5 Sensor response for various (a) bending cycles, and (b) bending times. Load applied is 0.5 kg.

bending radius grows, the output voltage also increases for a constant weight due to the deformation of velostat's shape. This is deemed unacceptable as it will compromise the reliability of the sensor. Nevertheless, the variation in sensor response due to bending radius can be represented by adjusting the parameters a and b in order to accurately forecast the appropriate response for a specific bending radius. In order to analyze the variation in the sensor's output for a specific bending radius, we determined the values of a and b using the bending depicted in Fig. 4.4. If we are utilizing the sensor to detect pressure on a curved surface, it is imperative that we take this modification into consideration.

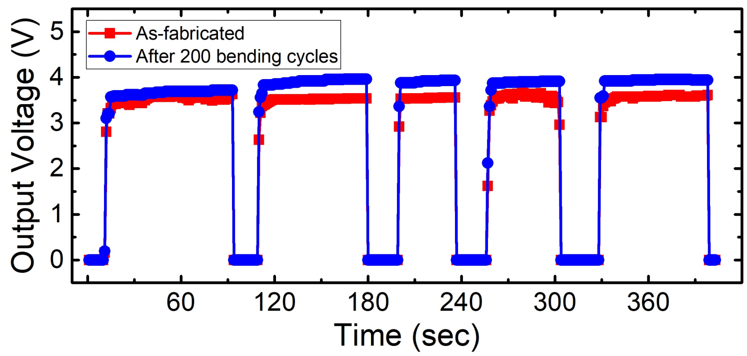

Figure 4.6 Sensor response for repeated application of load for as-fabricated sensor, and after 200 bending cycles. Only few out of the 50 loading cycles are shown in the figure.

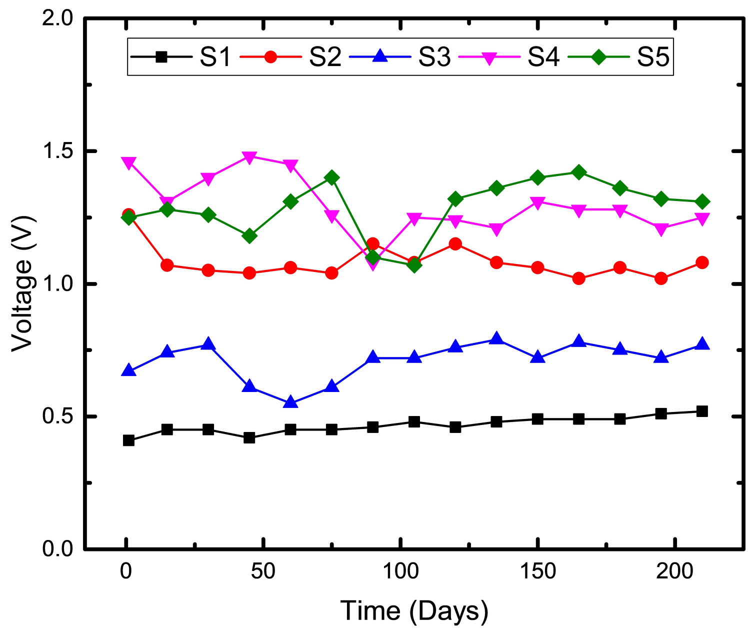

Figure 4.7 Response of first five sensors on the application of a load of 1 kg every fortnight for a duration of 210 days.

In the second experiment, we exposed the sensor to many bending cycles at various bending radii. Subsequently, we evaluated the sensor's reaction by placing it on a level surface while applying a consistent weight of 0.5 kg. This experiment aimed to assess if the sensor's reaction is affected by rolling, folding, or bending, especially in scenarios that involve dynamic flexing. The results are displayed in Fig. 4.5a. The output voltage is not monotonic with bending radius because of the internal structure of the velostat. The non-uniform distribution of the carbon particles in velostat affects the response of the sensor; hence, we observe a slight change in the sensor's response over multiple cycles of bending. The graph indicates a minimal alteration in the sensor's response over multiple cycles of bending. The

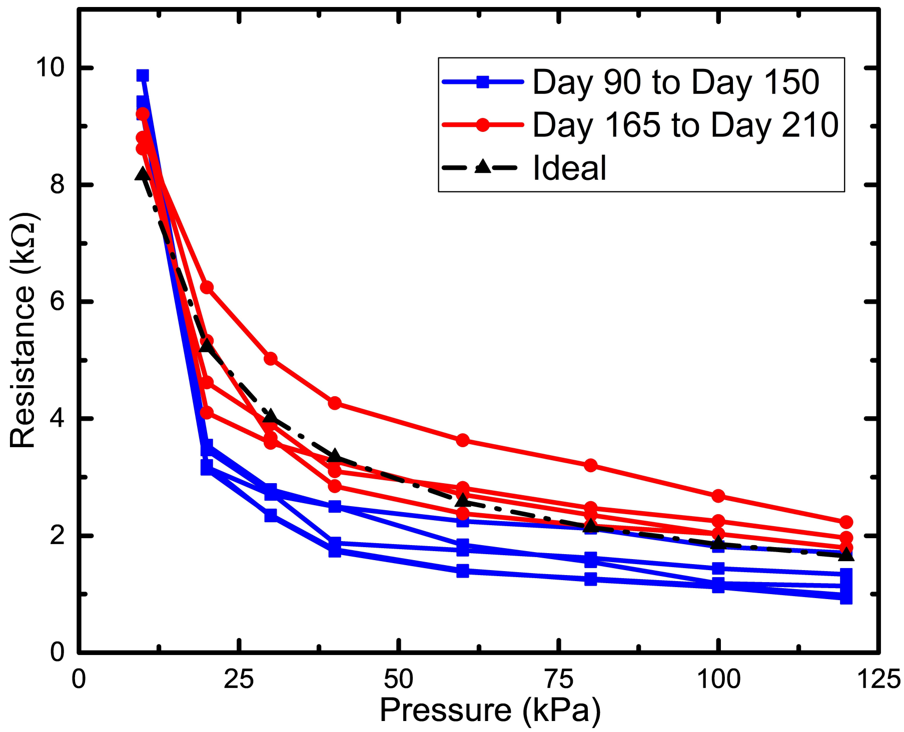

Figure 4.8 Change in resistance of the sensor pixel with the application of pressure from day 90 to day 210.

variation in output voltage was determined to be 0.95%, 0.95%, 0.97%, and 2.2% for bending radii of 15 mm, 20 mm, 25 mm, and 30 mm, respectively, following 150 cycles of bending. The sensor output was consistently measured in a horizontal position in all instances.

In the third experiment, we tested the dynamic response of the sensor for various bending radii. The results shown in Fig. 4.5b convey that there is a negligible change in the sensor's response which shows the reliability of the sensor. With respect to the output voltage, at $t = 0$, there is a deviation of 1.63%, 1.17%, 0.82%, 1.09%, and 2.5% for flat surface, 15 mm, 20 mm, 25 mm, and 30 mm bending radii respectively, after 16 hours of continuous operation.

In the final experiment, we tested the repeatability of the sensor response without bending and after bending it for 200 cycles. The sensor response was measured for 50 loading cycles, of which, results are shown for a few cycles in Fig. 4.6. Even after subjecting the sensor to 200 bending cycles, it shows reproducible results for rise and fall times. Repeatability is calculated as the difference in output produced when the sensor is loaded with the same weight for many cycles. The output voltages for a 0.5 kg load were found to be 3.54 $\pm$ 0.06 V for the as-fabricated sensor and 3.8 $\pm$ 0.1 after V 200 bending cycles, while the rise and fall times were found to be 1.22 s and 1.34 s for both cases.

Experimental results show the possibility of using it as a reliable device given rigorous calibration. It opens a broad perspective of using velostat as a force sensor. Hence, the sensor array can be used in any type of chair, with or without cushion.

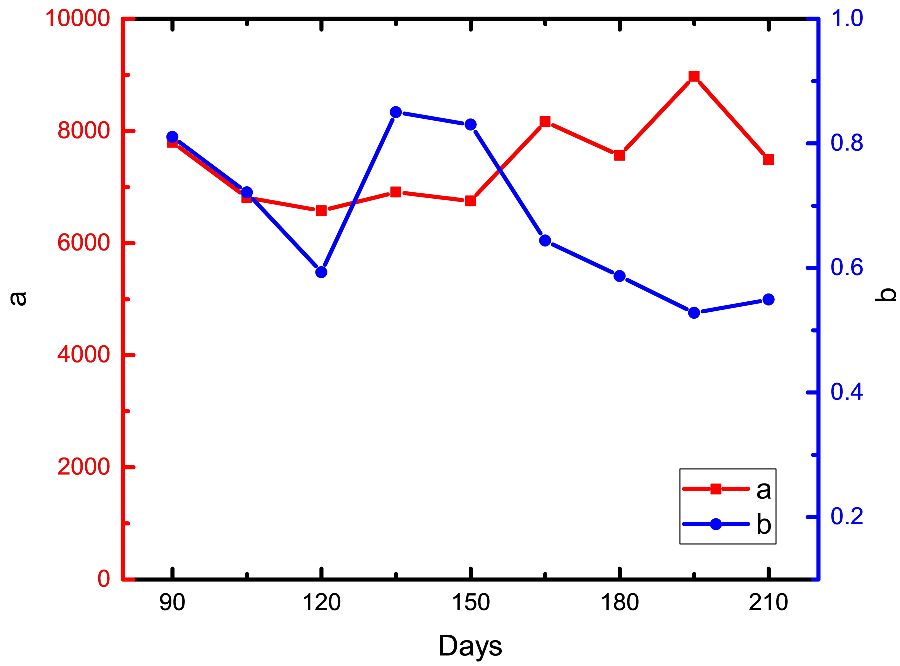

Figure 4.9 Variation of the calibration constants a and b for 150 days.

4.4.3 Long-term Reliability Analysis for 210 Days

Pressure sensors are subjected to continual force and stress that may damage the operation of the sensor in the long run. When designing and constructing any sensor, it is essential to consider reliability as a critical element. Evaluating the reliability of the entire product necessitates conducting tests on the sensor's substance. We have documented the enduring dependability of a pliable pressure sensor mat. Our main goal is to analyze the performance of a flexible pressure sensor array when subjected to prolonged and repetitive loading.

To perform the reliability study of the velostat-based pressure sensor, we conducted various experiments for a period of 210 days. In the first experiment, we tested the sensor's response every fortnight by applying a load of 1 kg to all sixteen sensors. As a representative sample, the output response for the first five sensors is shown in Fig. 4.7. We can observe that as time progresses, there is a change in the response of the sensor due to the changes in the characteristics of the velostat thin film. Hence, each sensor has to be calibrated. The average deviations in the sensor values for a load of 1 kg, as shown in the figure, are 0.03 V, 0.06 V, 0.07 V, 0.11 V, and 0.10 V for sensor 1 to sensor 5, respectively, in 210 days. The total average deviation in the sensor's response to placing a load of 1 kg on all sixteen sensor pixels is 0.32 V. We can observe that the deviation is very low and hence it can be used durably for non-critical sensing applications.

To test the sensor response to the application of higher pressure, we recorded the sensor's response by applying weights in a range of 1-12 kg every fortnight from day 90 on all sixteen sensors. Fig. 4.8

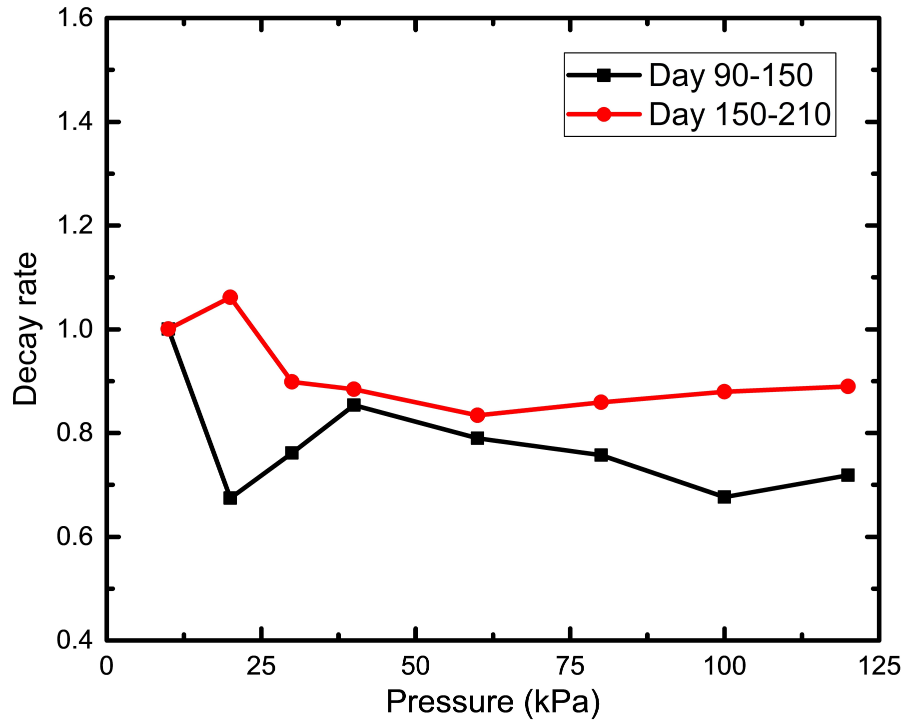

Figure 4.10 Decay ratio of the sensor's response in two different periods during the 210 day testing.

shows the change in resistance of the first sensor pixel from day 90 to day 210. Other sensor pixels show similar sensor responses. From the figure, we can understand that as the molecules in the velostat start settling, the resistance shows more gradation during the later days, i.e., from day 165 to day 210, and is closer to the mean graph. The mean graph was calculated by selecting constant values of the calibration constants a and b. The constants can also be varied to fit the individual curves. Fig. 4.9 shows the variation of the constants a and b over time from day 90 to day 210. We can observe that the constant b is starting to stabilize after day 150. We need to account for this change when calibrating the sensor to use it for commercial applications.

In order to determine the time needed for velostat to stabilize and produce consistent and replicable outcomes, we computed the decay ratio in the sensor's reaction. Fig. 4.10 illustrates the rate of change in values between day 90 and day 210. From day 150 to day 210, the sensor's repone closely approximates to 1, while from day 90 to day 150, it deviates significantly from 1. After a period of 150 days, the decay ratio of the pressure, which initially started at 10 kPa and decreased to 120 kPa, approaches a value closer to 1. This demonstrates that after a period of 150 days, velostat begins to exhibit consistent behavior. Over a period of 210 days, we conducted the test every two weeks, resulting in a total of 15 instances of loading on the sensor array. The weight range varied from 1 to 12 kg. In summary, our proposal suggests utilizing velostat, a thin film material, for designing a sensor array. However, instead

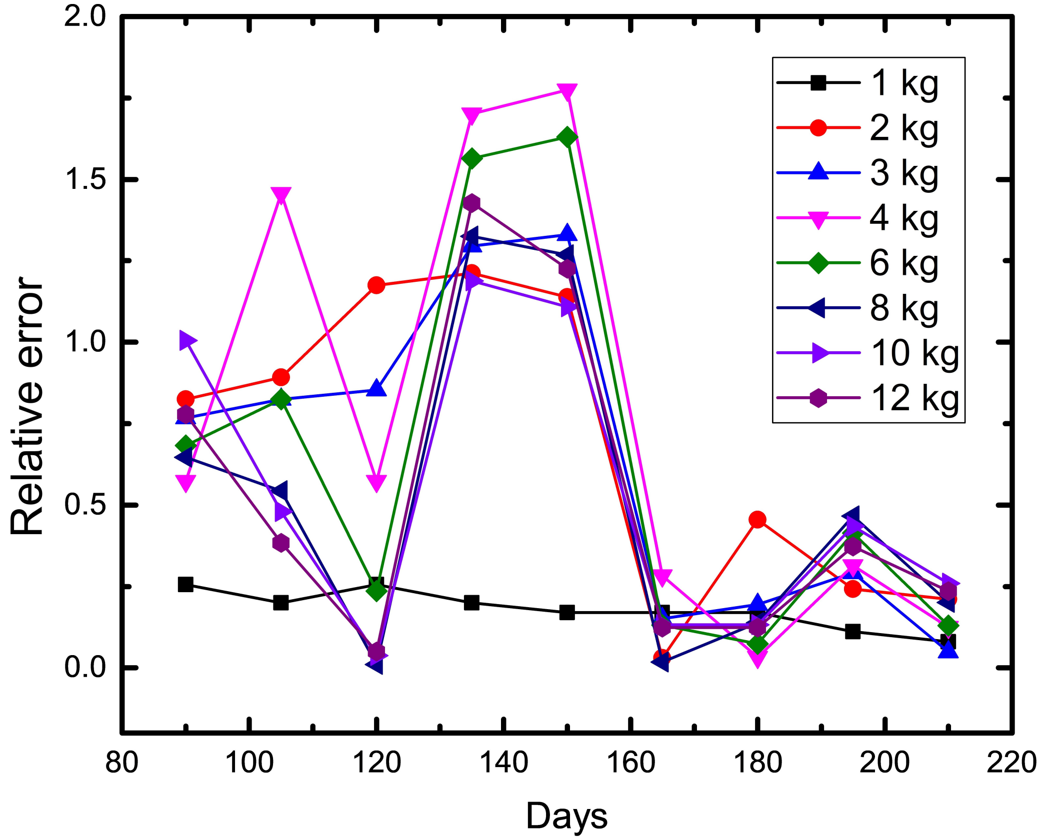

Figure 4.11 Variation in the relative error of the sensor pixel for 120 days from day 90 to day 210 shows reduction in error as the sensor ages.

of employing an unused or artificially created velostat film, we recommend loading it with various weights for a specific duration. This approach aims to yield more dependable and consistent outcomes.

The sensor pixel's relative error is computed over a span of 120 days, specifically from day 90 to day 210. The estimated error over a specific time period provides insights into the minimum time needed to achieve the lowest error and the long-term accuracy of the sensor. The calculation involved determining the absolute discrepancy between the estimated weight and the actual weight. The estimated weight was determined by applying the calibration constants of the ideal response (consistent values for all computations). The relative error is given by:

$$E_r = \frac{W_e - W_a}{W_a} \tag{4.6}$$

where W_e is the estimated weight by the sensor pixel and W_a is the actual weight placed on the sensor pixel. The W_e is calculated by:

$$W_e = (\frac{a}{R_{sens}})^{\frac{1}{b}} \tag{4.7}$$

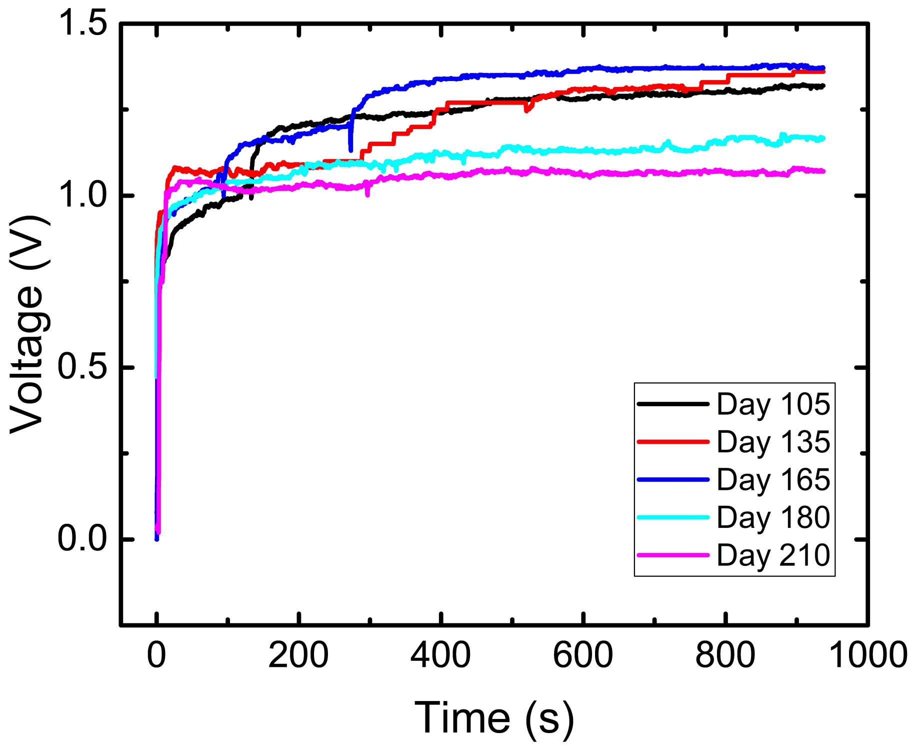

Figure 4.12 Variation in the temporal stability of the sensor's response over the period of the testing shows more stable sensor at the later stages of testing.

Fig. 4.11 shows the error for different loads from 1-12 kg. We can observe that the error for all the loads decreases drastically after 150 days. When we consider the error with respect to the load applied on the sensor pixel, we can observe that it is minimal for weights from 1 to 6 kg. This implies that the velostat-based sensors can be used reliably with repeatable responses till a maximum of 6 kg load. The error was reduced by 17.49, 61.43, 71.87, 44.82, 55.26, 44.57, 74.67, 54.34 percentage points for 1 kg, 2 kg, 3 kg, 4 kg, 6 kg, 8 kg, 10 kg and 12 kg respectively.

Finally, we conducted an experiment to calculate the time required by the sensor to reach a stable value. A load of 2 kg was placed on the same sensor pixel for a period of 20 minutes, every fortnight from day 105 to day 210. It was observed that as the load was placed for more amount of time, the output voltage of the sensor pixel increased. We also observed that the deviation in the sensor's response decreased every fortnight and is minimal on day 210 as observed in Fig. 4.12. The deviation on day 105 was 12.3% while the deviation on day 210 was 5.2%. This implies that even after using a used or aged velostat, we should always wait for at least 30 to 50 secs before taking the output response of the sensor pixel so that we get stable values.

To summarize the reliability study, in Fig. 4.13, we can visualize the change in sensor response over 210 days with the help of the heat maps showing the sensor response for a weight of 6 kg placed on every sensor pixel. This change in response is because of a change in the mechanical characteristics

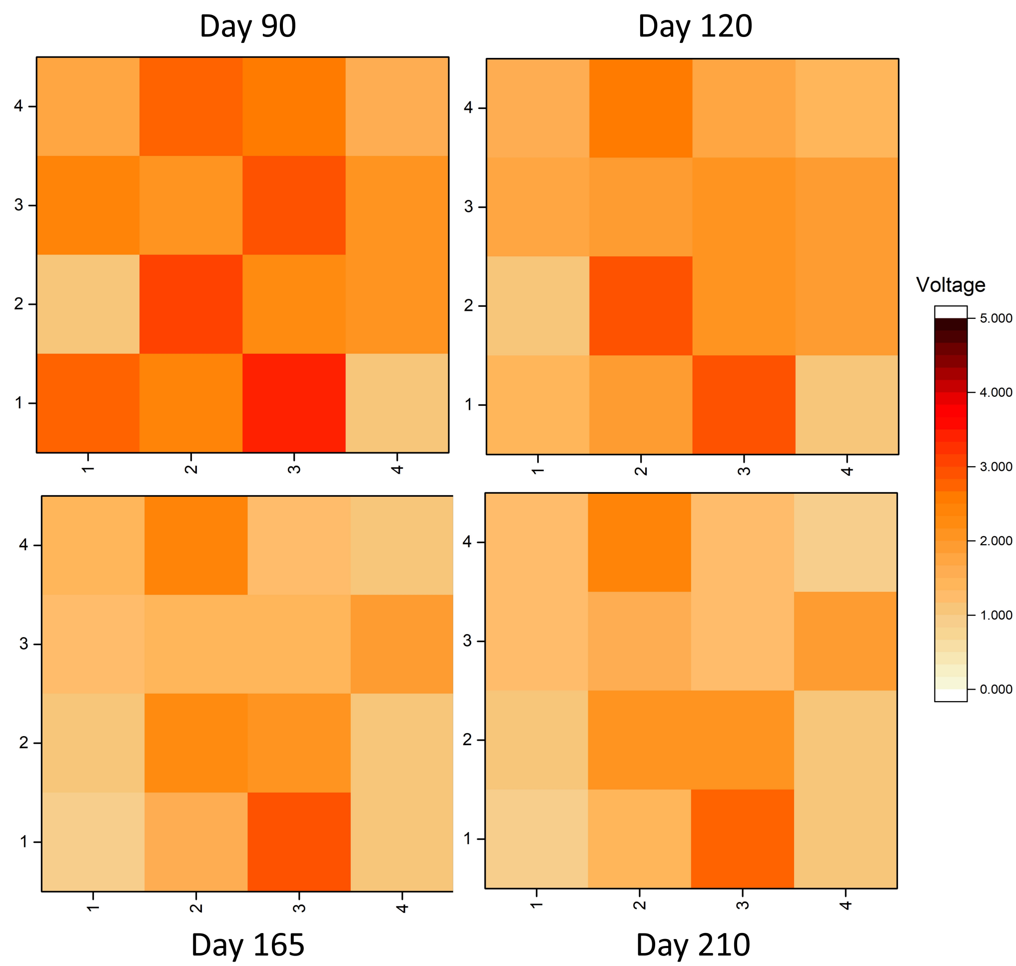

Figure 4.13 Heat map representing the response of all the sensor pixels on the sensor mat on various days of testing.

of the velostat across the mat. It can be seen that the response on earlier days (90 and 120) has more variations (difference between dark and light pixels), as compared to the response on later days. Further, the response stabilizes after a certain number of days, with minimal difference between the response at day 165 and day 210. The spatial variations can then be remedied using calibration.

4.5 Summary

In this chapter, we introduced our innovative methodology for calibrating the sensor. We introduced a new method to measure the interference between sensors in a matrix, which can be applied to any type of array and employed in many technologies. We conducted a comprehensive analysis of three flexible pressure sensing matrices utilizing a crossbar design employing Velostat material. In addition, we employed various weights to examine the patterns associated with fluctuating pressure values. We introduced the sensor's mechanical reliability for the first time. We have demonstrated the sensor's reaction when applied to curved surfaces with varying bending radii, as well as its response after subjecting it to multiple cycles of bending to assess its mechanical properties. We introduced a mathematical model to quantify the parameters of the sensor calibration curve. We additionally showcased the sensor's durability through extensive long-term reliability testing. Upon repeated application of load, we have discovered that the particles of the velostat eventually settle after a specific duration of time. Once this occurs, the resistance of the velostat undergoes a shift that remains constant over time. After a period of 210 days, we have noticed that the decay ratio is approaching a value of 1. Consequently, we can anticipate consistent and replicable outcomes from the velostat sensor following the implementation of force 15 times, within a load spectrum ranging from 1 to 12 kg. After 210 days, the relative error experiences a significant decrease, resulting in an overall reduction in error of 53 percentage points. Overall, after conducting a 210-day analysis on the dependability of velostat-based sensors, we observe promising indications for their utilization in a range of applications beyond just identifying and correcting sitting posture.

Chapter 5

Data Acquisition Circuit Design

5.1 Publication History

This chapter contains excerpts from the following publications: [26]

- **Anis Fatema**, A. Navnit, D. Devendra, A. M. Hussain, "A Combined Capacitance and Resistance Read-out circuit for Sensory Nodes," *IEEE Sensors Conference 2021, pp 1-4*.

5.2 Introduction

A data acquisition circuit is a circuit designed to retrieve data from a sensor. Designing an efficient data-collecting circuit is crucial for retrieving data from the sensor. Due to the presence of 1024 sensor pixels, it is necessary for us to have a readout circuit that provides a more rapid output. The preceding chapter covered the design and creation of the flexible pressure sensor array. The reading circuit included a microcontroller, multiplexers, resistors, and 16-pin connectors. The microcontroller primarily executed the task of converting analog signals to digital signals and provided us with the resulting output. Instead of utilizing a pre-made microcontroller, we opted to create our own custom read-out circuit. We have developed a circuit capable of converting capacitance and resistance into a digital output. A sensing system that can sense multiple environmental variables is an important block in Internet of Things (IoT) devices. Such a sensing system consists of different types of sensors based on their applications. Most of the sensors are designed based on the variation of capacitance or the resistance of a circuit entity. Capacitive sensing is used in a wide range of applications such as tactile sensing pressure sensing, humidity sensing and many more. Resistive sensors are also popular for the measurement of physical variables such as strain, displacement, and pressure. So, here we propose a combined capacitive-sensor and resistive-sensor interface circuit.

Many capacitive-sensor and resistive-sensor interfacing circuits have been proposed so far but very few circuits proposed the combined interface circuit. In [133], a period modulation approach was used. The capacitance was converted to time, followed by a time to digital conversion. In this case, a high frequency signal was required to perform time to digital conversion, resulting in increased power consumption. In [134], a Sigma-Delta Successive Approximation Register (SAR) topology was used, resulting in good resolution, however, the power consumption was very high. In [135], a hybrid SAR-VCO-based Sigma-Delta Capacitance to Digital Converter (CDC) was implemented to achieve high resolution with good energy efficiency. However, it could measure capacitance for a limited range of 0-5 pF. In [136], the interface circuit was implemented using two matched RC oscillators and a counter-based programmable digital converter that was independent of supply voltage and temperature. However, the designing of matched oscillators and programmable converter employed complex circuitry. The resistance to frequency converter proposed in [137] had a significant non-linearity in the output due to switching delays. A resistance to time period or pulse-width converter was presented in [138], but it required an additional interface unit to convert the quasi-digital output to digital. In [139], a Direct Digital Converter was proposed. The resistance was converted to analog voltage using Wheatstone bridge and then to digital data using dual-slope technique that comprises a complex circuitry of timing and control logic. A combined RCDC circuit was proposed in [140], which contained a sensor oscillator and a reference oscillator that were configured to read out the capacitive sensor or resistive sensors by selecting an appropriate tri-state buffer. However, it covered a limited range and consumed a high amount of power.

This chapter introduces a merged RCDC that utilizes SAR-ADC. A high gain operational amplifier (op-amp) has been utilized in the design of the capacitance to voltage converter to enhance linearity and minimize gain and offset error. The Wheatstone bridge is employed for converting resistance to voltage,

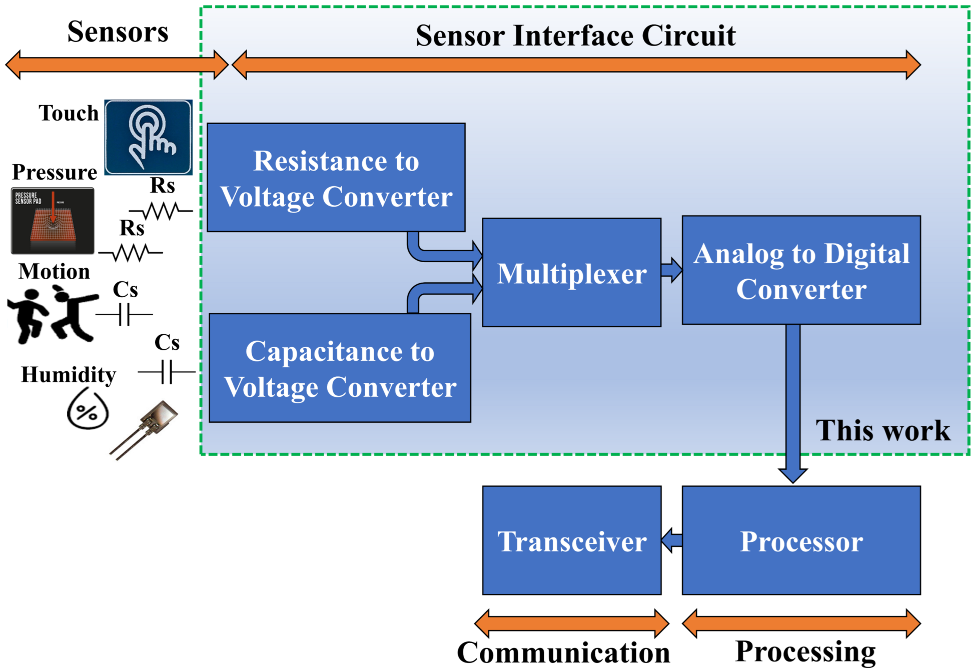

Figure 5.1 Architecture of a complete sensor system showing the component developed in this work.

as an alternative to a basic voltage divider circuit, in order to minimize power usage and vulnerability to temperature and supply voltage variations.

5.3 Circuit Design and Implementation

5.3.1 Proposed Architecture

An architecture of a complete sensor system is shown in Fig. 5.1. We present a combined resistance and capacitance to digital converter, which consists of separate resistance-to-voltage and capacitance-to-voltage converters. The analog output of these blocks is fed to a common Analog to Digital Converter (ADC).The user determines whether to read a resistive or capacitive sensor by utilizing an input pin. The SAR-ADC circuit converts the analog voltage to a 12-bit digital data, depending on the chosen operation.

5.3.2 Circuit Implementation

5.3.2.1 Capacitance to Voltage Converter

Fig. 5.2(a) shows the designed Capacitance to Voltage Converter (CVC) circuit. C_s and C_r represent sensor capacitance and reference capacitance, respectively. V_r represents the DC reference voltage. The circuit operation is performed by non-overlapping two-phase clocks. When $\phi = 1$, C_s is charged to

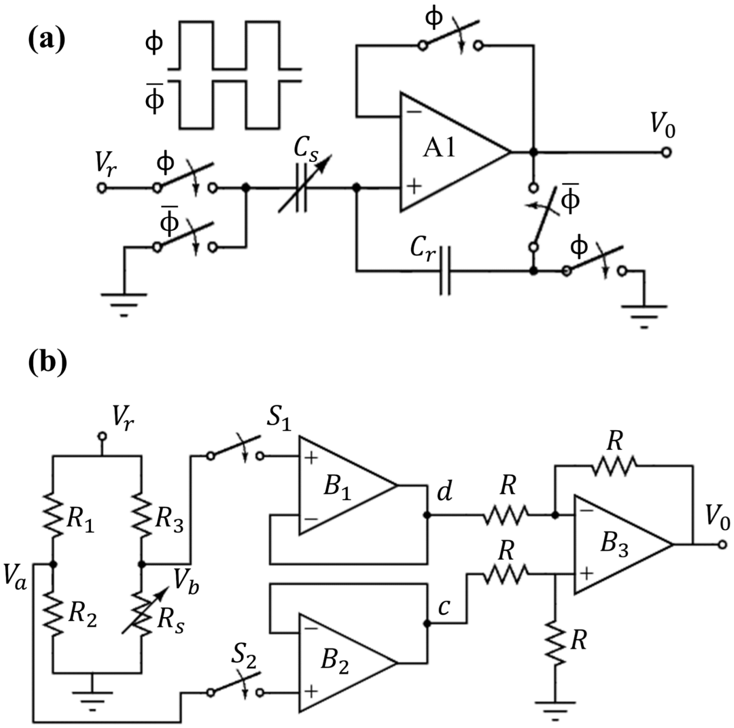

Figure 5.2 Circuit diagram of the (a) Capacitance to Voltage Converter, and (b) Resistance to Voltage Converter.

V_r, and C_r is discharged, then in the next phase when $\overline{\phi} = 1$, the charge present in the capacitor C_s is transferred to C_r. The output voltage V_0 is given by,

$$V_0 = \left(\frac{C_s}{C_s + C_r}\right) V_r \tag{5.1}$$

The use of a low-gain amplifier will produce a gain error in capacitance to voltage conversion [141]. Hence, a two-stage PMOS-input operational amplifier was implemented. The DC gain, unity gain frequency, and phase margin of the op-amp were found to be 75 dB, 83.9 MHz, and 72.8° respectively. A high reference capacitance of C_r = 500 pF was selected, to reduce the non-linearity in the output.

5.3.2.2 Resistance to Voltage Converter

Fig. 5.2(b) shows the designed Resistance to Voltage Converter (RVC) circuit. The resistors are connected in the form of a Wheatstone bridge because it provides good linearity, increased sensitivity, and automatic temperature compensation [142]. R_1=10 kΩ, R_2=50 kΩ and R_3=100 Ω are fixed resistors, and R_s is the sensed resistor. High values of R_1 and R_2 are selected to reduce the current flow and a low value of R_3 is chosen to meet the low range requirements of the sensed resistor. V_r is the DC reference voltage. The switches S_1 and S_2 are controlled by the reset signal, hence, the resistance to voltage conversion occurs only when the reset signal is high. When the reset signal goes low, the analog

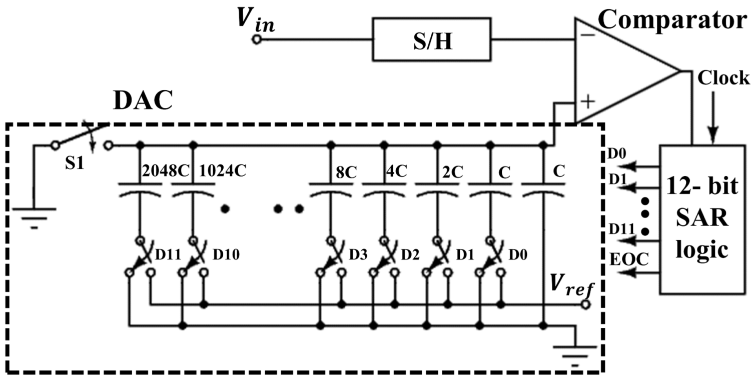

Figure 5.3 Architecture of SAR-ADC with binary weighted charge redistribution DAC.

voltage corresponding to the sensor resistance is converted to digital data. B_1 and B_2 are the analog buffers that are connected to avoid loading at the output. The voltages at the points c and d will be same as V_a and V_b. B_3 is an instrumentation amplifier whose output V_0 is given by:

$$V_0 = \left(\frac{R_2}{R_1 + R_2} - \frac{R_s}{R_3 + R_{sens}} \right) V_r \tag{5.2}$$

5.3.2.3 Analog to Digital converter

The main building blocks of SAR-ADC are sample and hold circuit, comparator, SAR logic, and DAC. The sample and hold circuit samples the signal during reset phase and holds it during the conversion phase. A dynamic latch comparator is used, as it is low power, high speed, high input impedance, and gives a full swing output. The designed comparator has delay, resolution, and power consumption of 8.8 ns, 0.01 V, and 0.47 mW respectively.

The SAR-ADC was preferred because it gives high accuracy and speed and is the lowest power-consuming type of ADC [143]. It has less number of analog components and has a novel switching scheme [144]. A binary-weighted capacitive DAC (CDAC) was chosen because it has fewer non-linearities compared to a split CDAC, however, it occupies a large layout area because the capacitance of each bit doubles in size [145]. The 12-bit binary-weighted DAC consists of 12 capacitors with values of C, $2C$, $4C$ up to $2048C$ plus one extra non-charging branch with capacitance C. The unit capacitance C was chosen to be 40 fF.

5.4 Results

The layout of the designed RCDC circuit is shown in Fig. 5.4. The circuit was designed and implemented in TSMC 0.18 μm IP6M CMOS technology. Assura verification tool was used for the Design Rule Check (DRC), Layout Vs Schematic (LVS) and extraction of parasitics in the layout. The capacitors used in the layout design are MIMcaps (metal insulator metal capacitors) with capacitance per unit

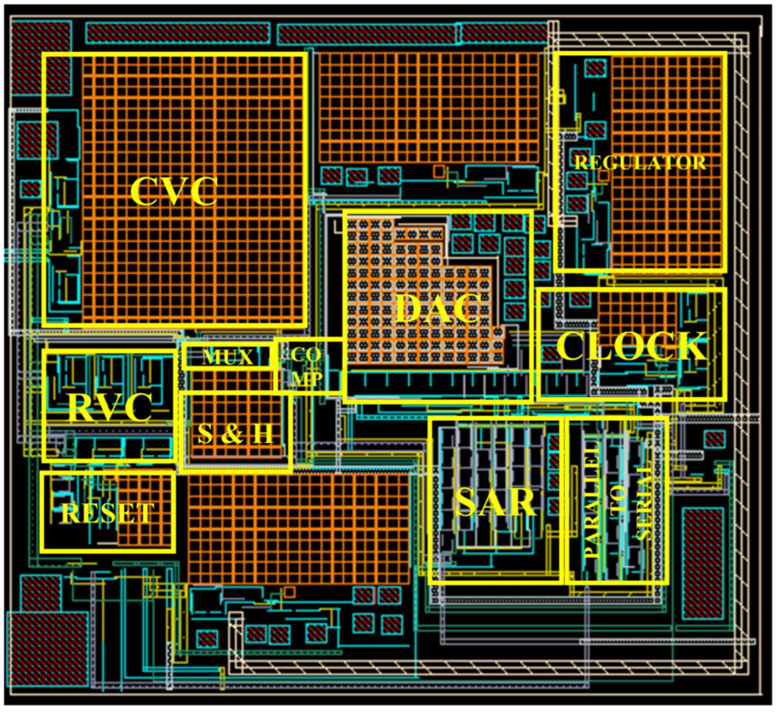

Figure 5.4 Layout of the RCDC circuit, with functional block diagrams. The abbreviation 'MUX' shown in the layout stands for multiplexer, 'COMP' for comparator and 'S & H' for sample and hold. The scale bar is 0.25 mm.

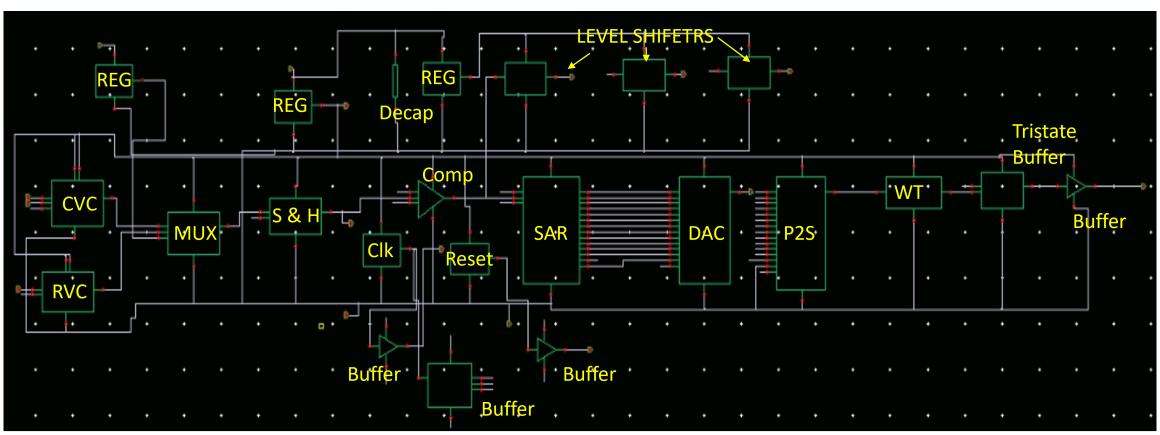

Figure 5.5 The complete circuit design in cadence.

area of 2 fF/μm^2. The complete circuit design is shown in Fig. 5.5. The post-extraction active area was 3.2 mm^2. Fig. 5.6 shows the simulation results of the timing and operation of the circuit. The circuit uses capacitive charge/discharge timing to internally generate a 1.2 MHz clock. The 'select' signal decides whether the capacitance or the resistance will be converted to digital data. When End of Conversion (EOC) goes high, the parallel output data from SAR is converted into serial output. The

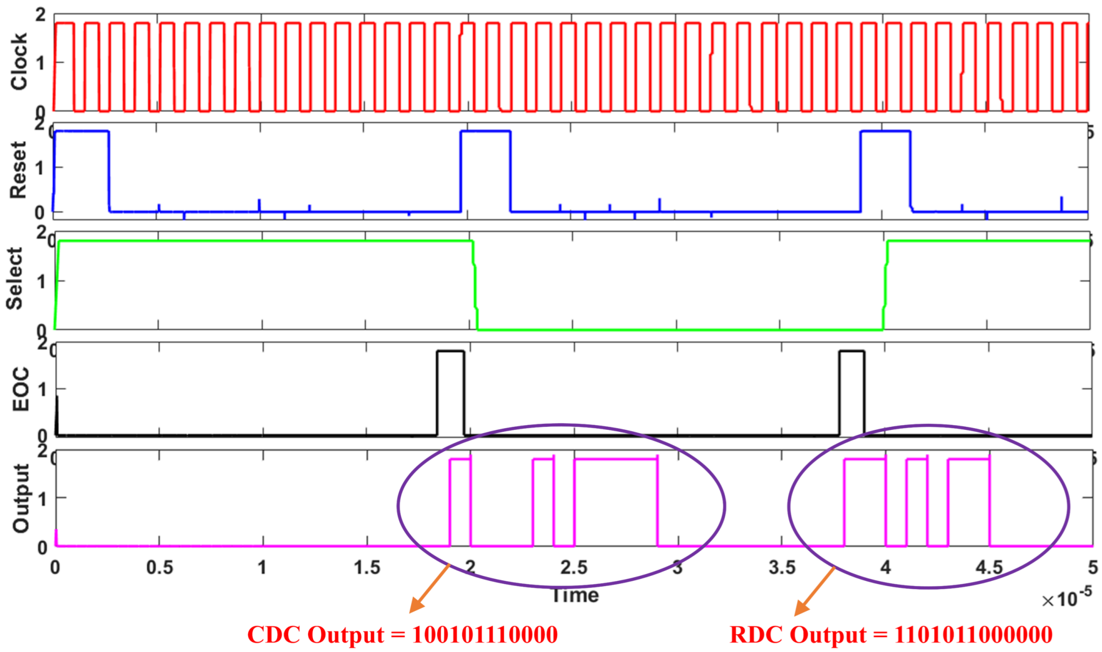

Figure 5.6 Output response of the interface circuit with sensor capacitance 50 pF and sensor resistance 20 ohms.

Table 5.1 Performance summary

Architecture	SAR
Output format	12-bit Digital code
Technology	0.18 μm
Supply Voltage	2.5 V to 4.2 V
Conversion time	20 μs
Range of CDC	30 pF to 100 pF
Range of RDC	1 Ω to 30 Ω
Temperature Range	-40 to 125^{0}C
Resolution of CDC	17fF
Resolution of RDC	7 mΩ
Power consumption of CDC	117 mW
Power consumption of RDC	126 mW
Nonlinearity of CDC	0.66%
Nonlinearity of RDC	0.57%

operation is divided into two phases: reset phase and the conversion phase. In the reset phase, the 'reset' signal will be high, and the capacitance and the resistance are converted into the analog voltage. In the conversion phase, the reset signal will be low, and the conversion of analog voltage into digital data is performed. To evaluate the performance of the circuit, the sensor capacitance is varied from 30 pF to 100 pF and the sensor resistance is varied from 1 Ω to 30 Ω and their digital output (reported after

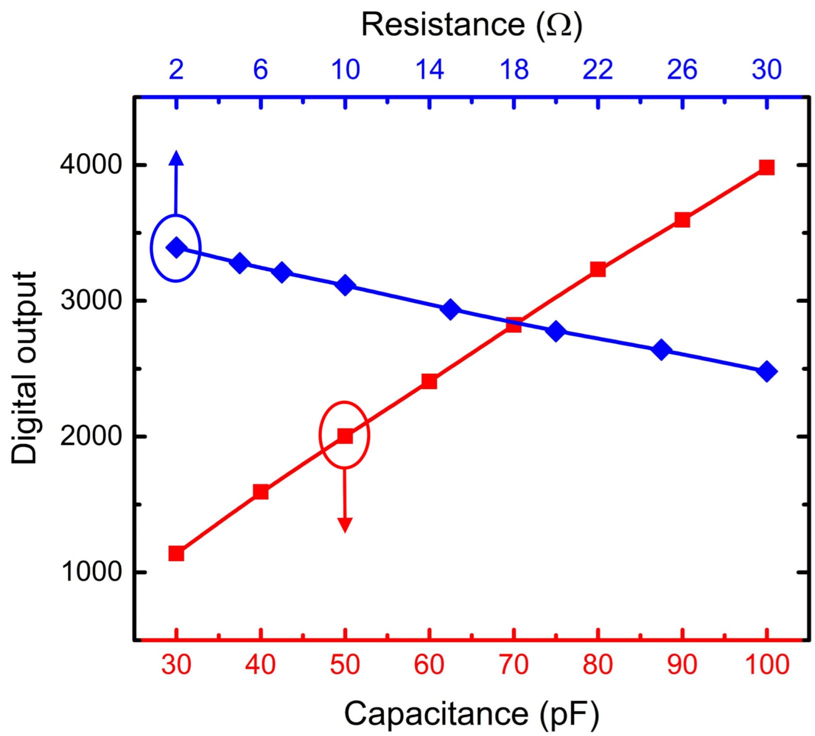

Figure 5.7 The 12-bit digital output (represented as a decimal number) versus sensor capacitance and sensor resistance.

Table 5.2 Performance comparison with commercially available ICs

Parameters	**Our circuit**	**PCAP04**	**AD7745**	**PS081**	**MAX31865**
Manufacturers	-	ScioSens	Analog devices	Analog devices	Analog devices
Circuit	RCDC	CDC	CDC	RDC	RDC
Digital output	12 bit	20 bit	7 bit	24 bit	15 bit
Supply Voltage	2.5 V to 4.2 V	2.1 V to 3.6 V	2.7 V to 5.25 V	2.1 V to 3.6 V	0.3 V to 4 V
Range of CDC	30 pF to 100 pF	1 pF to 100 nF	4 pF to 17 pF	-	-
Range of RDC	1 Ω to 30 Ω	-	-	1 Ω to 10 Ω	100 Ω to 1 KΩ
Operating Temp.	-40 to 125^{0}C	-40 to 125^{0}C	-40 to 125^{0}C	-40 to 125^{0}C	-40 to 125^{0}C

conversion to decimal) is recorded as shown in Fig. 5.7. The resolution of CDC and RDC is 17 fF and 7 mΩ respectively. The non-linearity shown by CDC and RDC is 0.66% and 0.57%, respectively. The final top layout with pads is shown in Fig. 5.8

The table 5.1 shows the performance summary of the circuit design. All the internal circuits operate at 1.8 V and 3.3 V. We have also designed the complete layout with pads and sent for fabrication to Muse semiconductors. The performance of the designed circuit was also compared with the commercially available sensor ICs as shown in the table 5.2

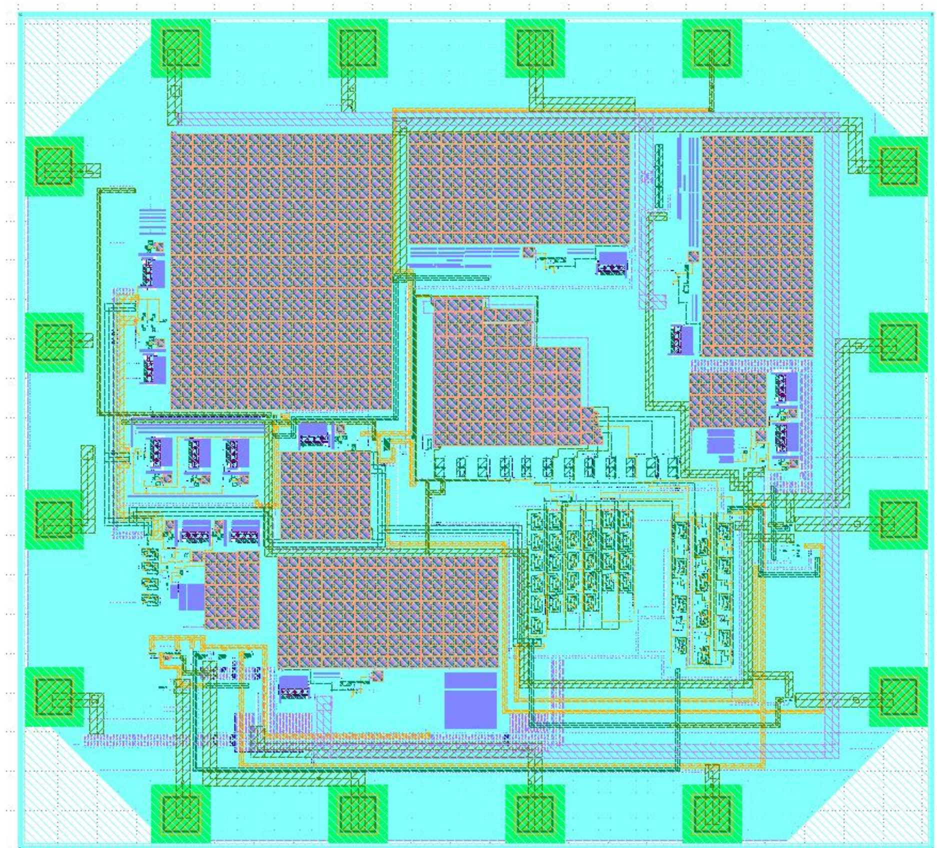

Figure 5.8 The final top level chip design with pads sent for fabrication

5.5 Summary

An interface circuit with flexibility to read out both capacitive and resistive types of sensors has been presented in this chapter. It requires less area and is more cost-effective than separate single-sensor read-out circuits. The designed SAR-RCDC circuit is implemented in TSMC 0.18 μm IP6M CMOS technology, with an active area of 3.2 mm^2. It converts the resistance or capacitance to 12-bit digital data with a conversion time of 20 μs at a 1.8 V power supply. It consumes 117 mW and 126 mW of power at full-scale input capacitance and resistance, respectively. The 12-bit output data is communicated as a serial output with synchronization achieved using the system clock output. The novelty of the design is its performance and designing a combined read-out circuit. This read-out circuit can be used with single resistive or capacitive sensors but has limitations when used with the sensor array.

Chapter 6

Posture Recognition System

6.1 Publication History

- **Anis Fatema**, B. Kokad. M. Hussain, “Development of Flexible Pressure Sensor System for Posture Recognition in Smart Chair using Machine Learning,” to be submitted in *Scientific Reports*, 2024.

6.2 Introduction

Long periods of time spent sitting with bad posture can result in a number of health problems, such as cervical, lower, and upper back pain. It's critical for people to maintain good posture when working or studying. The existing pressure sensor-based systems that have been proposed to recognize sitting postures are limited by the number of sensors, number of postures detected, and accuracy, leaving room for improvement. Nowadays, most people work or study for extended periods of time while seated in chairs. Most students and office workers spend more than 8 to 9 hours a day seated. Due to an increase in persons working from home during and after the COVID-19 epidemic, the issue has got worse. Research indicates that sitting incorrectly for longer than six hours can harm the body and raise health risks [146]. For example, it may increase the risk of long-term conditions like diabetes, heart disease, stroke, and metabolic syndrome. Inadequate sitting positions can also lead to issues with the spine, including unequal shoulders, leg length disparity, pelvic tucking, and neck pain [147–149].

Figure 6.1 Prevalance of lower back pain in adults

Numerous techniques have been put forth to identify sitting positions. We can broadly classify them into three categories. The first method is to use wearable sensors [150–154]. In [150], a method for continuously monitoring of head posture was presented. Forward head posture (FHP) is a common musculoskeletal disorder that is correlated with neck pain. It affects a large percentage of the population. It is seen in situations such as slouching while sitting or standing. They used accelerometer-based wireless inertial body sensors to monitor FHP. In another research, through the use of mobile devices affixed to specific human spinal sites (thoracic, thoraco-lumbar, and lumbar), [151] built models to identify correct or incorrect sitting postures. It also discovered the connections between appropriate sitting positions and human body frames. The models were created by leveraging the data gathered from 49 students with varying body frames to train several well-known classifiers, including KNN, SVM, MLP, and Decision Tree. The Decision Tree classifier showed the most promising performance, with a kappa of 0.921 and an accuracy of 96.13%. The findings also indicated a connection between posture and body frame. In another wearable sensor based posture recognition system, [152] presented the recognition and categorization of various sitting and standing postures. Classification accuracies employing three triaxial accelerometers and gyroscope sensors are shown to be higher than those obtained with just one or two sensors. The collected characteristics' principal component analysis (PCA) demonstrates a considerable degree of differentiation between the postures under consideration. The study included four distinct classifiers: random forest (RF), decision tree, multi-layer perceptron, and support vector machine (SVM). Of these, SVM yielded the highest accuracy. An average classification accuracy of 95.68% is obtained by the RF classifier for 9 distinct body postures (5 seated postures and 4 standing postures) executed by 7 participants. In [153], a wearable strain gauge sensor was designed to measure the recognition of sitting posture and was positioned at the lower back. The low-cost tool that was developed has a number of benefits, such as its high precision, straightforward design, low power consumption, and easy installation. In order to optimize and integrate these innovative sensors into a sitting posture monitoring application, the volume fractions of the nickel nanostrands (NiNs) and nickel coated carbon fibers (NCCF) were selected. In another work, to get the required information regarding the sitting posture of the person, Sangyong Ma et al. [154] employed a three-axis accelerometer. Support vector machine (SVM) and K-means algorithms were used to identify a sitting position after the data had been standardized. Nonetheless, wearing a three-axis accelerometer or any other wearable device for posture monitoring for an extended amount of time is inconvenient for the user. Hence, we didn't select this category for designing a posture recognition system.

The second category is to use camera for posture recognition. Initially, a camera was positioned in front of or next to a seat to record sitting positions. Subsequently, sitting postures were classified using an image recognition technique [155–159]. For instance, Lan Mu et al. [159] recognized seated postures using a Webcam. Initially, the sitting posture profile is extracted; Second, pattern matching based on Hausdorff distance is used to further extract the profile features, including the size and placement of the face. Lastly, the surveillance system would advise the user to adjust their sitting position by contrasting the standard profile characteristics with the real-time profile features. The Hausdorff distance was chosen as the method for identifying body and facial postures. However, their method is restricted to identifying the sitting posture of the upper body. The lower body cannot be identified. Furthermore, the results of this process might not be reliable if someone passes in front of the camera and the camera records them.

Methods based on pressure sensors make up the third category. We have also selected this method. To identify sitting postures, flexible pressure sensors or a matrix sensor mat were placed on the chair. Two ultrasonic sensors were placed on a chair's back by Haeyoon Cho et al. [160], together with multiple pressure sensors on the cushion. Data was collected using both the ultrasonic sensor and the pressure sensors. In order to gather pressure data, they placed 25 pressure sensors throughout the chair's hip area. The regions of the chair surface that best represent important aspects of sitting postures were found using the data that have been gathered. Subsequently, they employ diverse machine learning techniques to identify ten typical sitting positions and assess their effectiveness. Support vector machine (SVM), k-nearest neighbors (KNN), decision tree, random forest, and logistic regression are some of the machine learning techniques employed in the evaluation.

Apart from the three categories mentioned above, [161] presented the first sitting posture identification system that just uses radio frequency wave (SitR), requiring no wearable sensors on the human body or jeopardizing privacy. They demonstrated that SitR can identify seven common sitting postures with just three inexpensive, lightweight RFID tags applied to the user's back. The solution takes advantage of the relationship between sitting postures and the phase change of RFID tags. Using ten volunteers, SitR's performance was assessed in two distinct circumstances. Numerous tests demonstrated that SitR can accurately identify seven sitting positions in a variety of settings and circumstances. It can further detect the abnormal respiration, stand up, and sit down and provide sitting posture history for sedentary people. The fundamental concept involves an antenna positioned on the chair's back and three tags adhered to the user's back. Under various sitting positions, the distance between each tag and the antenna varies. Secondly, the phase of the received signal at the reader fluctuates in accordance with changes in the tag-to-antenna distance and angle. As each sitting posture has a distinct phase variation, it helps in identifying different sitting postures. However, it is difficult to use the tags to accurately identify sitting postures without making the user uncomfortable and decide how to produce a noticeable phase-changing pattern in the face of hardware noise, and the multipath effect presents the second challenge. In addition to this, RFID tags might also have problems when multiple individuals are sitting in the same room.

6.3 Related Work

In recent years, numerous pressure sensor-based techniques have been put forth. The basic concept is to attach pressure sensors to a chair's back and hip areas to record signals related to sitting positions. Six pressure sensors were first mounted on a chair's hips, armrests, and back sections by Qisong Hu et al. [162] in order to gather pressure readings. They then constructed an Artificial Neural Network (ANN) model for classification using a look-up table. Their findings revealed a 9 ns processing time and a 97.8% accuracy rate. A technique to categorize sitting positions was proposed by Wenyao Xu et al. [163] using an electronic textile (eTextile) pressure sensor on the seat cushion. The conductive polymer-coated fibers in the eTextile are equipped with strain and pressure sensors. While a user was seated on the cushion, the device recorded pressure signals. Dynamic Time Warping (DTW), which filters out background noise, was used to categorize postures. The accuracy rate obtained was 85.9%. 90 pressure sensors were mounted on the back of the chair, and 81 pressure sensors were positioned on the hip by Jianquan Wang et al. [164]. They achieved an accuracy rate of 88.52% in the classification of sitting postures using the Spiking Neural Network (Spiking-NN). Their approach involved sensor readings from the back of the seat. A wide range of pressure pads on the hip region were employed by Zhe Fan, Qilong Wan, Xu Ran, and colleagues [54, 165, 166] to gather user hip pressure signals, which were then transformed into a pressure map. This pressure map was utilized to construct a classification neural network model. Despite the fact that this technique can accurately recognize sitting postures, the hardware is expensive—it can cost up to 300 USD. The recognition results were displayed on an Android phone. Although the system achieved an accuracy rate of up to 96%, it required 18 sensors, resulting in relatively high hardware costs. A hybrid sensor system with six pressure sensors and six distance sensors mounted on a chair was proposed by Haeseok Jeong et al. [167]. A K-nearest neighbors (KNN) model for posture classification was trained using the gathered pressure and distance measurements. Their findings demonstrated an accuracy as high as 92%. Nevertheless, this approach necessitated the installation of distance sensors on the back of the seat, and the height and size of the user may have an impact on the accuracy. A system including 16 pressure sensors and two ultrasonic sensors was created by Haeyoon Cho et al. [168]. An Arduino board was utilized to process the gathered signals before sending them to the Naver Cloud Platform for posture categorization using Convolutional Neural Network (CNN) and Lower-Balanced Check Network (LBCNet).

6.4 Posture Recognition Methods

Upon a person's sitting, we gauge the pressure they apply and utilize this information to ascertain their posture. We examine each pressure map to determine whether the individual is maintaining a favorable or unfavorable body position. In order to accomplish this, we employ diverse machine learning algorithms to categorize and identify distinct postures by analyzing their respective pressure maps.

Data is gathered from a pressure sensor pad that is linked to both the seat and backrest. The sensor consists of a combined total of 2048 pixels, with 1024 located on the seat and 1024 on the backrest. These pixels are utilized to accurately track and record an individual's body position. The provided data is utilized for categorizing various seating positions. In order to identify these postures, five distinct algorithms were employed and will be examined in this section. The subsequent section will provide a comprehensive account of the outcomes and precision of each method.

6.4.1 Support Vector Machine

The SVM is a highly popular and effective supervised learning algorithm utilized for classification and regression tasks [169]. This method establishes the decision boundary for different datasets on sitting posture and optimizes it by transforming it into a hyperplane for classification [170]. The number of sitting posture data points, denoted as N, can be expressed as X = (x_{ij}, y_i), where x_{ij} represents the j-th pressure sensor value of the i-th sitting posture data, and y_i represents the corresponding sitting posture category. The formula shown in Equation 6.1 and 6.2 represents the good sitting posture (y_i = 1) and the hunchback posture (y_i=$-$ 1) in SVM. In this formula, ω denotes the weight vector, and b represents the bias used to separate the hyperplane. [170] The simplified formula is shown in equation 6.3. It allows for the differentiation of distinct limits for each individual session.

$$\omega^T x_{ij} + b \geq 1 \tag{6.1}$$

$$\omega^T x_{ij} + b \leq -1 \tag{6.2}$$

$$y_i(\omega^T x_{ij} + b) \geq 1 \tag{6.3}$$

6.4.2 K Nearest Neighbour

The KNN algorithm entails the identification of analogous coordinates in a vector space, which serves as a measure of the distance between two data points representing sitting postures. [171]. The Euclidean Distance is employed to compute the distance between distinct sitting posture data. Assume that there are two sitting posture data points in the training set, denoted as n, where x_i represents the known sitting posture data: x_i = [x_1, x_2, $\cdots$, $x_1$3], and x_j represents the unknown sitting posture data: x_j = [x_1, x_2, $\cdots$, $x_1$3]. The Euclidean Distance between them is expressed in Equation 6.4.

$$d(x_i, x_j) = \sqrt{\sum_{k=1}^{n}(x_{ik} - x_{jk})^2} \tag{6.4}$$

In order to determine the distance, it is necessary to specify the value of k, which denotes the quantity of closest neighbors to be taken into account. For instance, when k is equal to 3, the algorithm will detect the three coordinates with the smallest distance and determine the sitting position based on these three coordinates. The predominant sitting posture among these neighbors is regarded as the superior class. In order to get a comprehensive classification of the 10 sitting postures, it is customary to select k as an odd number to prevent any instances of ties. When the value of k is excessively big, it may lead to the inclusion of unnecessary coordinates, hence reducing the accuracy of the classification. Conversely, if the value of k is too little, there is a risk of overfitting. This study employed the attributes of the KNN model, which entails placing a substantial quantity of sitting posture coordinates in a multi-dimensional space. The KNN method can categorize sitting postures based on the high similarity of coordinates in the vector space when the sitting posture features are comparable.

6.4.3 Decision Tree

The decision tree algorithm is a hierarchical algorithm that acquires and deduces decision rules for forecasting results based on characteristics of the data [172]. It is frequently employed in regression and classification tasks. The Gini coefficient is used to identify the root node and build the model in a recursive top-down approach until the dataset is fully divided. The Gini coefficient quantifies the level of impurity in a given sample. The dataset representing the sitting posture, labeled as N, can be expressed as X = (x_{ij}, y_i).

In this context, S denotes the number of labels, whereas x_{ij} indicates the likelihood of category y_i being in the dataset X. A lower Gini coefficient signifies reduced impurity within the dataset. Given the nature of our study, which deals with an issue involving several classifications, we employ the calculation of 10 Gini coefficients for various sitting postures in order to carry out the division.

$$Gini(X) = 1 - \sum_{y_i=1}^{S}(x_{ij}^2) \tag{6.5}$$

The decision tree algorithm partitions the features and their respective values to identify the optimal branches for identifying sitting postures. The depth of the tree is indicative of the intricacy of the decision rules, and a greater depth generally captures more complicated patterns, resulting in a model that is more closely aligned with actual sitting positions. Nevertheless, an abundance of noise in the data or an excessively complex tree can result in overfitting problems. In order to tackle this issue, we made modifications to the parameters associated with the depth of the trees. This was done to find a suitable equilibrium between collecting significant patterns and avoiding overfitting.

6.4.4 Logistic Regression

Logistic regression is a statistical model that is derived from the principles of linear regression. The classification model primarily computes a decision boundary to partition the data [173]. It can also be referred to as a linear regression model for classification, primarily utilizing the sigmoid function for classification as demonstrated in equation 6.6. In equation 6.6, the N sitting posture data can be represented as X = (x_{ij}, y_i). The e is a Euler's number which is a mathematical constant. The sitting postures are classified according to a threshold.

$$g(X) = \frac{1}{1 + e^{-z}} \tag{6.6}$$

However, logistic regression is usually used for binary classification. In our study, it generates K binary classifiers. When predicting, the sitting posture data will be put into the K classifiers, and the classifier with the highest prediction score wins.

6.4.5 Artificial Neural networks

Artificial Neural Networks (ANN) are a valuable tool that draws inspiration from biological neural networks. They can be employed to estimate unknown functions using known inputs. The architecture of an Artificial Neural Network (ANN) consists of three layers: the input layer (u), the hidden layer (h), and the output layer (y). The input layer is represented by u = u_1, u_2, $\ldots$, u_M, the hidden layer is represented by h = h_1, h_2, $\ldots$, h_L, and the output layer is represented by y = y_1, y_2, $\ldots$, y_N. M, L, and N represent the number of data points in the input layer, the number of neurons in the hidden layer, and the number of approximated outputs, respectively. The benefits of ANN classifiers encompass, but are not restricted to, exceptional classification accuracy; formidable capability for parallel distributed processing, distributed storage, and learning; substantial resilience, tolerance to noise, and ability to approximate nonlinear relationships [174].

6.4.6 Principal Component Analysis

In a PCA-based approach, the most important thing is to find the principal components of the distribution of pressure maps, or more generally, the eigenvectors of the covariance matrix of a set of training pressure maps. Our PCA-based posture classification algorithm involves two separate steps:

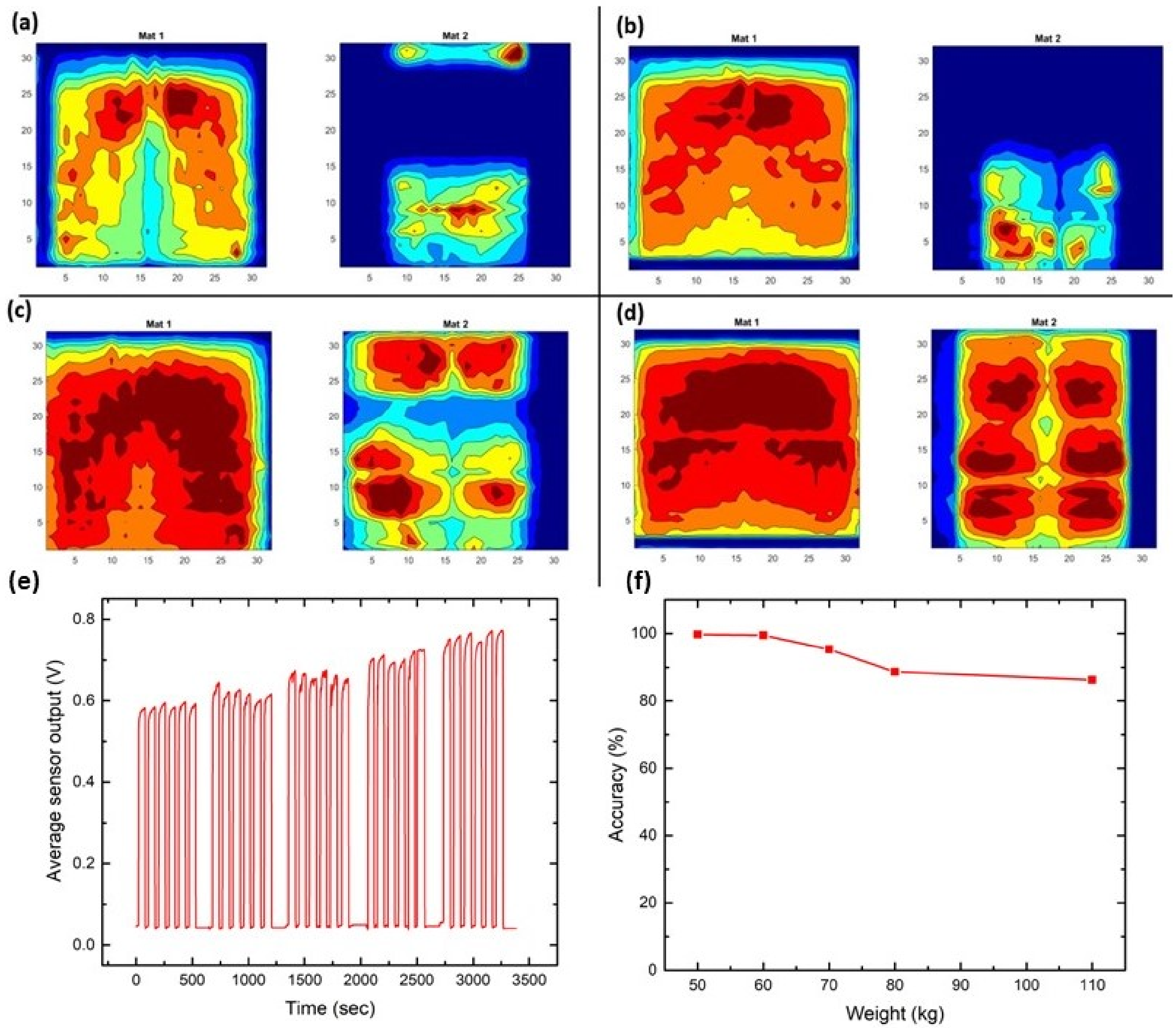

Figure 6.2 The heat maps of the sensor mat on the seat and the backrest as obtained from four different users sitting in Posture 1 are shown in (a–d). The weights of the subjects are 60 kg, 70 kg, 80 kg, and 110 kg, respectively. (e) Graph showing repeatability of the sensor with subjects of different weights of 50 kg, 60 kg, 70 kg, 80 kg, and 110 kg. (f) Graph showing the relationship of testing accuracy of the NN model with respect to the weight of the person

training and posture classification. In the first step, training data for a set of predefined static postures are collected. Pressure maps corresponding to the same posture are used to calculate the eigenvectors that best represent the variations among them. Each of the total training pressure maps is raster-scanned to form a vector of 2048 elements. The mean-adjusted vectors are then used to compute the covariance matrix, from which a set of eigenvectors are calculated so that their corresponding eigenvalues decrease monotonically. These eigenvectors can be thought of as forming an n-dimensional eigen posture space where a 2048-element pressure map can be represented by the weights of its projection onto this eigenspace [175].

6.5 Methodology

6.5.1 Experiment Details

The flexible pressure sensing mat of size 42 cm × 42 cm is placed on the seat and the backrest of the chair. It is a low-cost, automated sensor mat providing high accuracy. It is a 32 × 32 pressure sensing array with each sensing pixel of size 0.6 cm × 0.6 cm. The read-out circuit box is fixed at the back side of the chair. It is connected to the laptop using a USB cable, and the posture recognition app is run on the screen. We can observe the change in the posture of the user in real-time. When the algorithm detects a wrong posture for more than 10 minutes, it alerts the user with a beep. The system architecture includes data collection from the sensor mat, data processing by the user interface and data display that includes showing the posture is good or bad.

6.5.2 Data Collection and Analysis

To verify the accuracy of the model, we conducted a data collection process involving two stages. In the first stage, we collected data to train the model and evaluate its accuracy. In the second stage, we collected additional data to test the model's classification performance and assess the usability of the system. It's important to note that our experiment has received ethics approval from the Institute Review Board (IRB) of the International Institute of Information Technology Hyderabad. Each participant in the study was provided with detailed information about the experimental procedures and goals, and they voluntarily signed a research participant consent form.

A total of 15 volunteers participated in the study. The characteristics of the volunteers are as follows: The age distribution was between 20 and 28 years old, the weight distribution was between 60 and 107 kg, and the height distribution was between 156 and 182 cm. During the experiment, the participants were instructed to perform seven different sitting postures: straight, slouch, leaning forward, leaning left, leaning right, leaning left leg crossed, and leaning right leg crossed.

For each sitting posture, the subjects consecutively maintained the position for 2 minutes, resulting in a total test duration of 14 minutes. The data sampling rate is one sample per second, resulting in a total of 840 posture data points. Each data point includes the sensor readings of the 2048 pressure sensing pixels, that includes 1024 pixels on the seat and 1024 pixels on the backrest. Since we have 15 participants, there were 12,600 data points used to establish models. We used the data of 12 participants for training and then the data of the remaining 3 participants to test the algorithm's accuracy.

Figure 6.2(a-d) shows the heat maps of the pressure sensor mat on the seat and the backrest of four users of different weights of 60 kg, 70 kg, 80 kg, and 110 kg, respectively. Figure 6.2e shows the repeatability of the sensor. We have conducted the experiment with the same users whose heatmaps are shown in Figure 6.2(a-d). The users were asked to sit on the mat for 60 seconds, stand for 30 seconds, and repeat six times. We took the average sensor output of the 1024 sensor pixels of the sensor mat on the seat and observed repeatable results for all users. In order to test the dependency of weight on the testing accuracy for all postures, we trained the NN model and tested the data of users of different

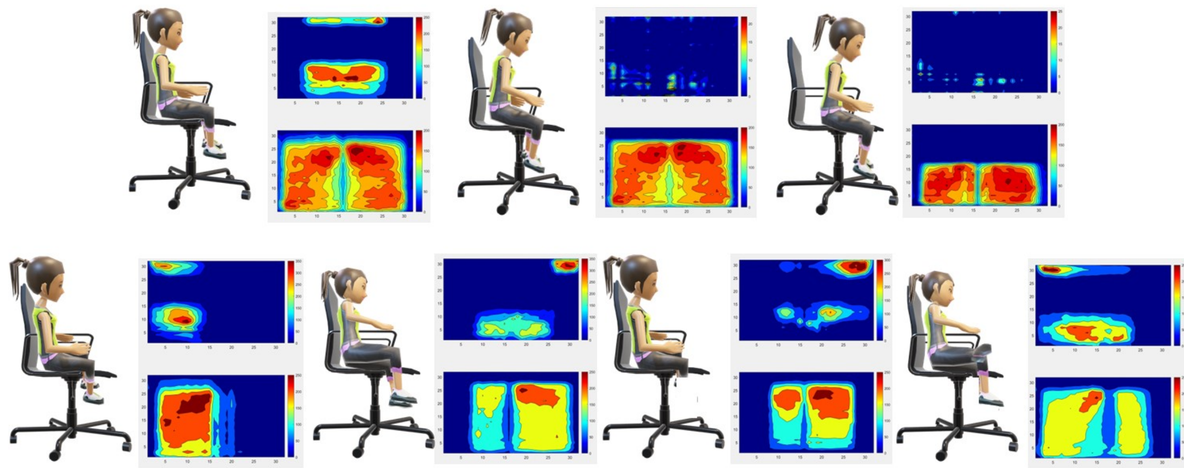

Figure 6.3 Illustration of seven different sitting postures with pressure maps of seat and backrest: (a) sitting upright, (b) slouching, (c) leaning forward, (d) leaning left, (e) leaning right, (f) leaning left leg crossed, and (g) leaning right leg crossed.

weights of 50 kg, 60 kg, 70 kg, 80 kg, and 110 kg, as shown in Figure 6.2e. We can observe that the average accuracy from 50-70 kg weight is 98.2%, and the accuracy until 90 kg is 95.2%, and it reduces to 93.9% beyond 110 kg. Hence, in this approach, users with weights of 40 to 110 kg can use the smart chair without any need for weight calibration. While maintaining the recognition accuracy above 95%, the weight limit can be considered as 110 kg.

6.6 Results and Discussion

6.6.1 Support Vector Machine

The SVM model was trained for different kernel functions. The parameters of the Kernel Function can be categorized into linear parameters and nonlinear parameters. We have trained and tested our model using linear, quadratic, cubic, and gaussian SVM models. The accuracy of the SVM model using different Kernel Functions is summarized in Table 6.1. The SVM model exhibits varying performance with different Kernel Functions. The gaussian SVM model has achieved the highest accuracy rate of 99.88% for validation and 95.89% for testing. Figure 6.4 shows the confusion matrix for all the models.

6.6.2 K- Nearest Neighbour

We have tested KNN algorithm for different K values and different distances. Since the K value directly influences the performance of KNN, it is crucial to compare different K values to determine the one with the highest accuracy. We tested the algorithm using Euclidean, Minkowski, and Cosine

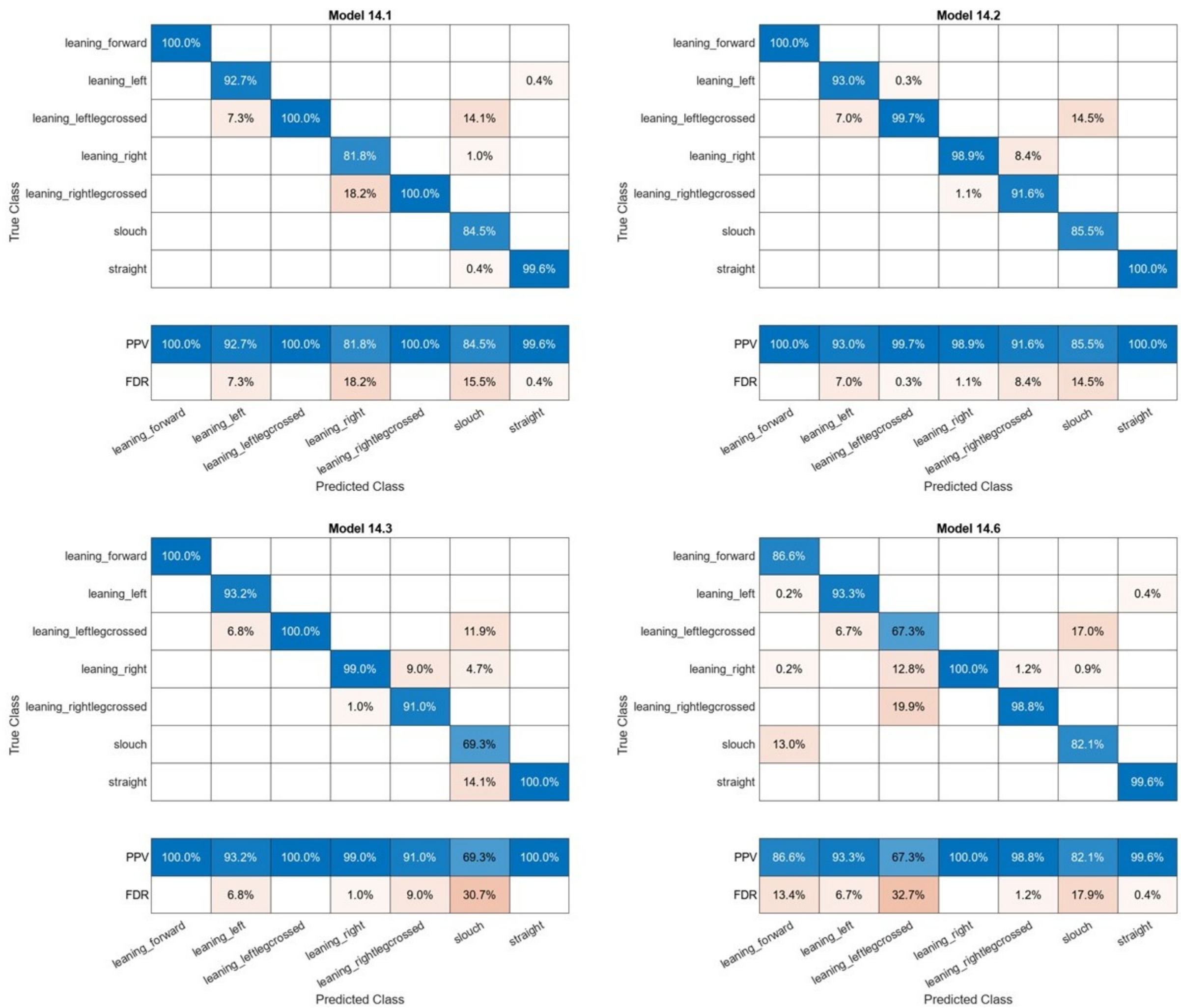

Figure 6.4 Confusion matrix of SVM models. Starting from left (a) linear (b) quadratic (c) cubic (d) gaussian

Table 6.1 Comparison of SVM models

Name	Training time	Validation Accuracy	Testing Accuracy
SVM linear model	503.59 s	99.6%	93%
SVM quadratic model	477.36 s	99.8%	95.2%
SVM cubic model	496.72 s	99.9%	91.6%
SVM gaussian model	94.27 s	99.88%	95.89%

distance. Table 6.2 shows the comparison of accuracies achieved using different methods. We obtained the best hyperparameters for the KNN by observing the Minimum Classification Error (MCE). Table 6.2 shows that the K value of 1 with Minkowski distance yields the best validation accuracy of 99.84%, testing accuracy of 92.71%, and an F1 score of 0.93.

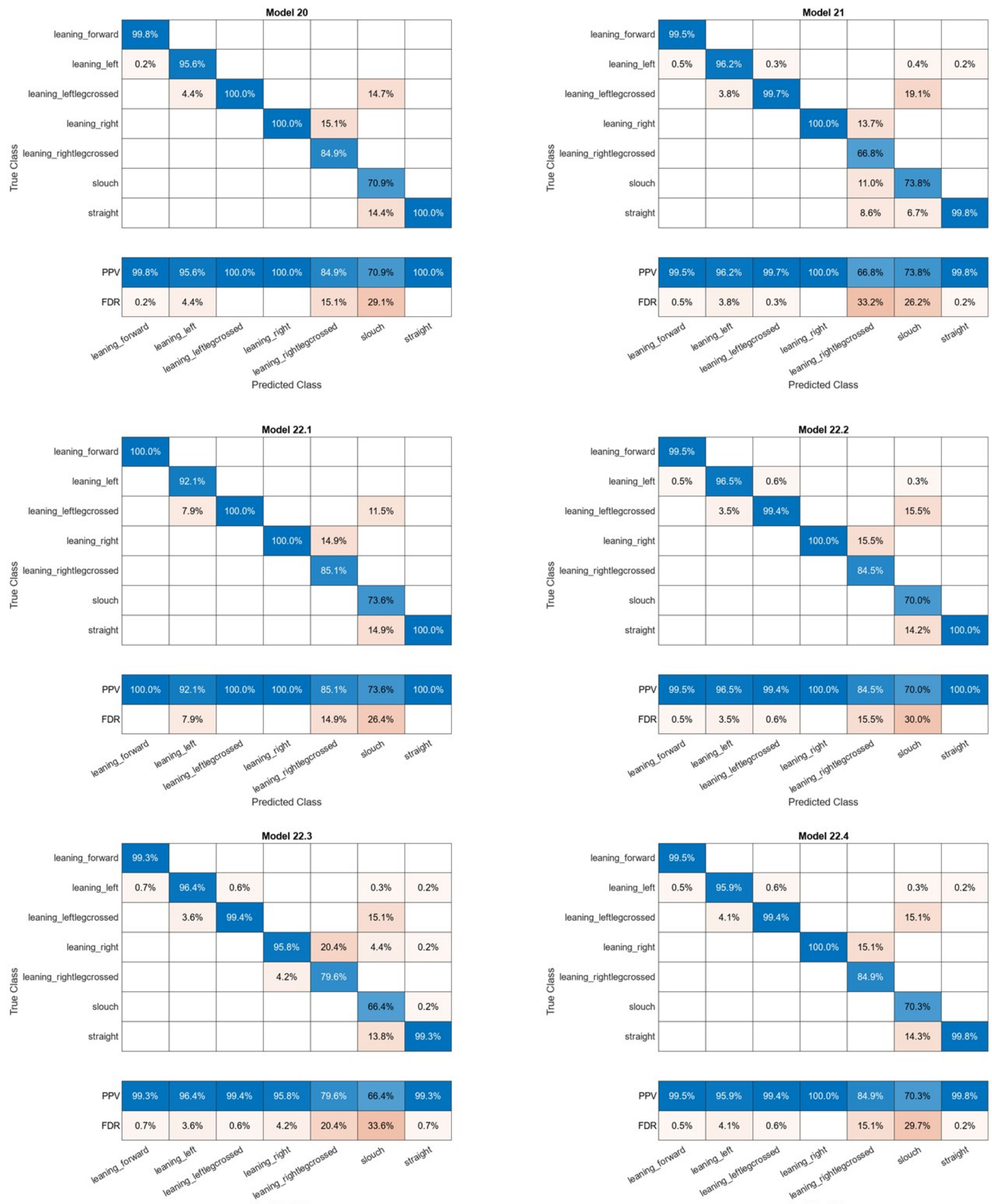

Figure 6.5 Confusion matrix of KNN models. Starting from left (a) k=3, Euclidean distance (b)k=1, Minkowski distance (c) k=1, Euclidean distance (d) k=10, Euclidean distance (e) k=100, Euclidean distance (f) k=10, cosine distance

Table 6.2 Comparison of k-NN models

Name	Training time	Validation Accuracy	Testing Accuracy
k=3, Euclidean distance	683.88 s	99.8%	91.5%
k=1, Minkowski distance	1942.6 s	99.84%	92.71%
k=1, Euclidean distance	1851.9 s	99.9%	91.4%
k=10, Euclidean distance	1943.2 s	99.6%	91.3%
k=10, Euclidean distance	1900.2 s	96.6%	88.9%
k=100, Euclidean distance	2117 s	99.7%	91.3%

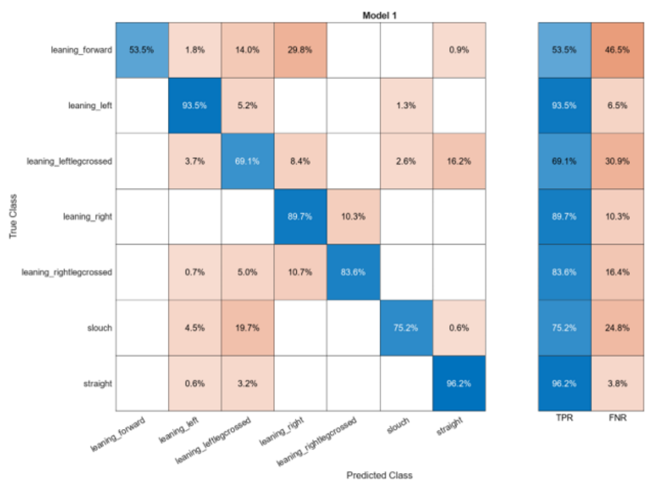

Figure 6.6 Confusion matrix of decision tree with n=425

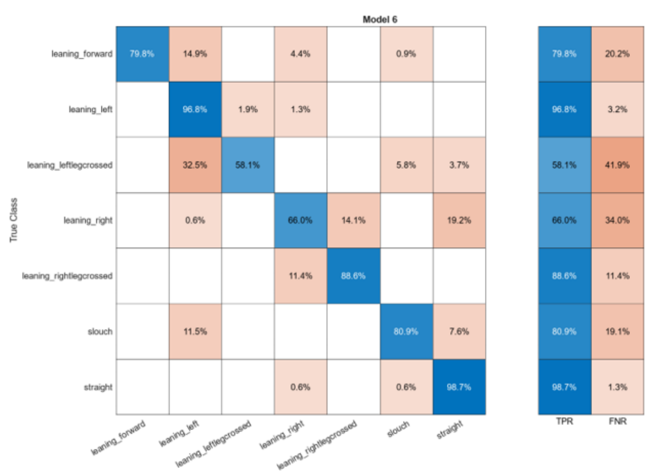

Figure 6.7 Confusion matrix of Logistic Regression model

6.6.3 Decision Tree

We observed the MCE plot for the Decision Tree (DT) model trained for variable number of splits and split criteria. The best hyperparameter point yeilds number of splits as 425, and Twoing rule as the

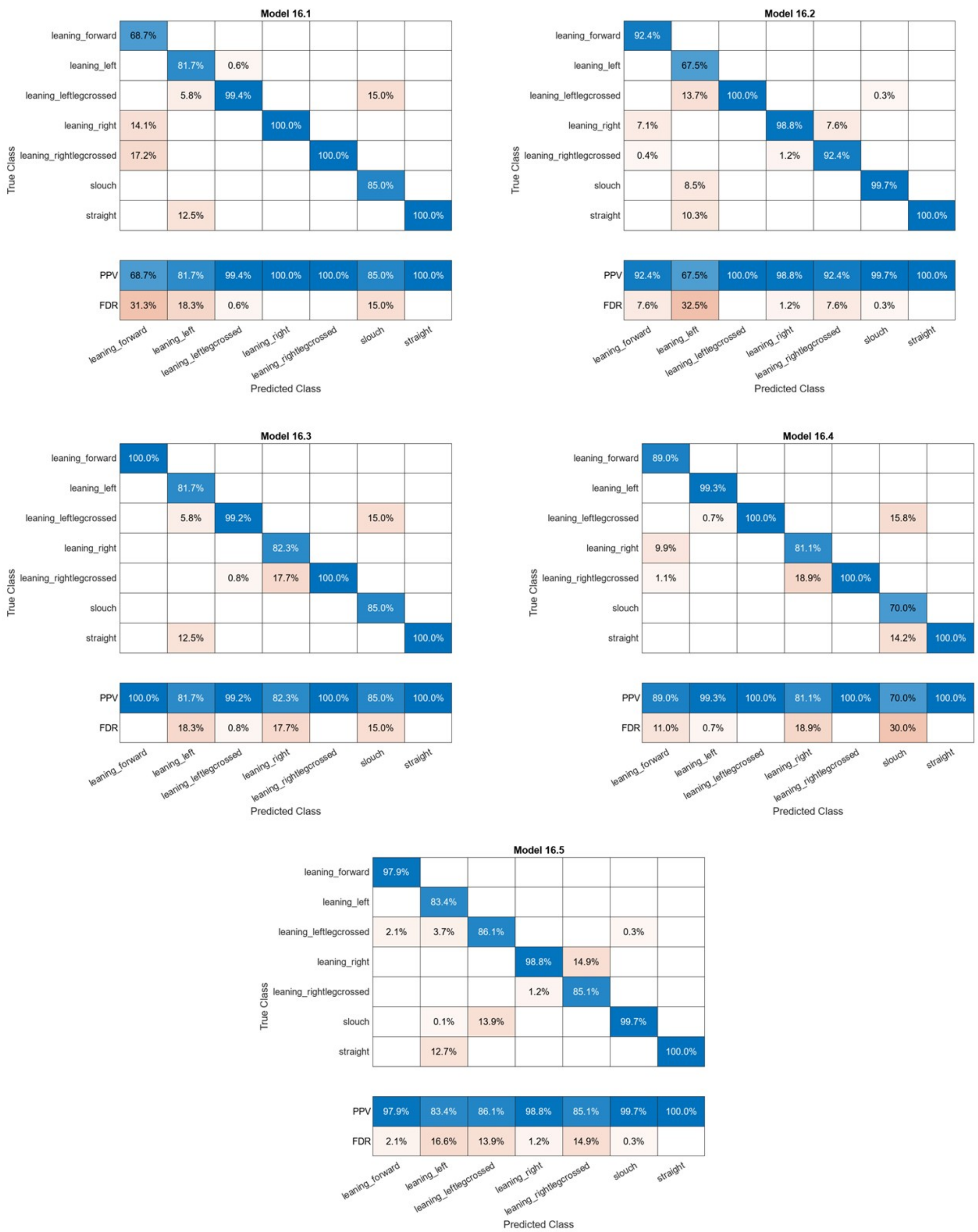

Figure 6.8 Confusion matrix of Neural Network models

split criterion. We proceed with testing and we obtain validation accuracy achieved of 98.79%, testing accuracy of 80.75%, and an F1 score of 0.82. Though the accuracy is much less compared to other models, it has the least training time of 15.13 seconds and highest prediction speed of 11000 obs/sec.

6.6.4 Logistic Regression

Logistic regression calculates the probability of each classification based on probability theory and selects the class with the highest probability as the result. The training time for the model is 72.19 sec. The validation accuracy achieved is 95.36%, the testing accuracy of 80.47%, and an F1 score of 0.83.

6.6.5 Neural Network

We observed the MCE plot for neural network trained for variable number of hidden layers, and variable size of hidden layers. From the MCE graph, we obtain the best hyperparameters as tanh activation function, and 1 fully connected layer with 189 neurons, it yields a validation accuracy of 99.86%. Upon testing, we obtain a testing accuracy of 95.61% and an F1 score of 0.96. It gives the best accuracy compared to other models (along with SVM) but takes the highest training time of 12,446 seconds. We conclude this model to be the best for our application due to it's high testing accuracy and prediction speed. Moreover, neural networks have great tolerance to noise, and ability to approximate nonlinear relationships [174].

Table 6.3 Comparison of Neural Network models

Name	Training time	Validation Accuracy	Testing Accuracy
1 hidden layer of size=10	505.2 s	99.9%	88%
1 hidden layer of size=25	303.41 s	99.8%	89.4%
1 hidden layer of size=189	12446 s	99.86%	95.61%
2 hidden layer of size=10 each	517.93 s	99.8%	89.7%
3 hidden layer of size=10 each	707.54 s	99.8%	91.7%

6.6.6 Comparison of Algorithms

The confusion matrices of the classification test results for each classifier selected with their best hyperparameters are shown in Figure 6.9. These confusion matrices show the true positive rates and false negative rates. A row-normalized row summary displays the percentages of correctly and incorrectly classified observations for each true class. In the confusion matrix of the NN model in Figure 6.8e, we can observe that the true positive rate(TPR) is 100% for five of the seven postures. The false negative rate (FNR) is limited to 21.5% for the leaning left leg cross posture label, where it is confused with leaning left posture for 16.2% and slouching for 5.2%. The TPR of the leaning right leg cross posture is 95.7%, where it is confused with the leaning right posture for 4.3%. All the remaining postures have 100% accuracy. Similarly, in the SVM model, we have observed 100% test accuracy in five out of seven postures. The TPR of leaning forward is 96.5% with FNR of 3.5% as it is confused with leaning right posture. The TPR of leaning left leg cross posture is 79.1% with FNR of 20.9% contributed by confusion due to leaning left and slouching posture. From the confusion matrices, we can observe the next best model is KNN, having four out of seven postures with 100% accuracy. The least TPR in KNN is for

Name	Training time	Predic. speed	Val. Acc.	Test. Acc.	F1 score
SVM Gaussian model	94.27 s	3500 obs/sec	99.88%	95.89%	0.96
KNN, k=1, Minkowski distance	1942.6 s	22 obs/sec	99.84%	92.71%	0.93
Efficient logistic Regression	72.19 s	6200 obs/sec	95.36%	80.47%	0.83
Decision tree (n=425)	15.13 s	11000 obs/sec	98.79%	80.75%	0.82
NN, with tanh activation function	12446 s	7800 obs/sec	99.86%	95.61%	0.96

Table 6.4 Comparison of all machine learning models

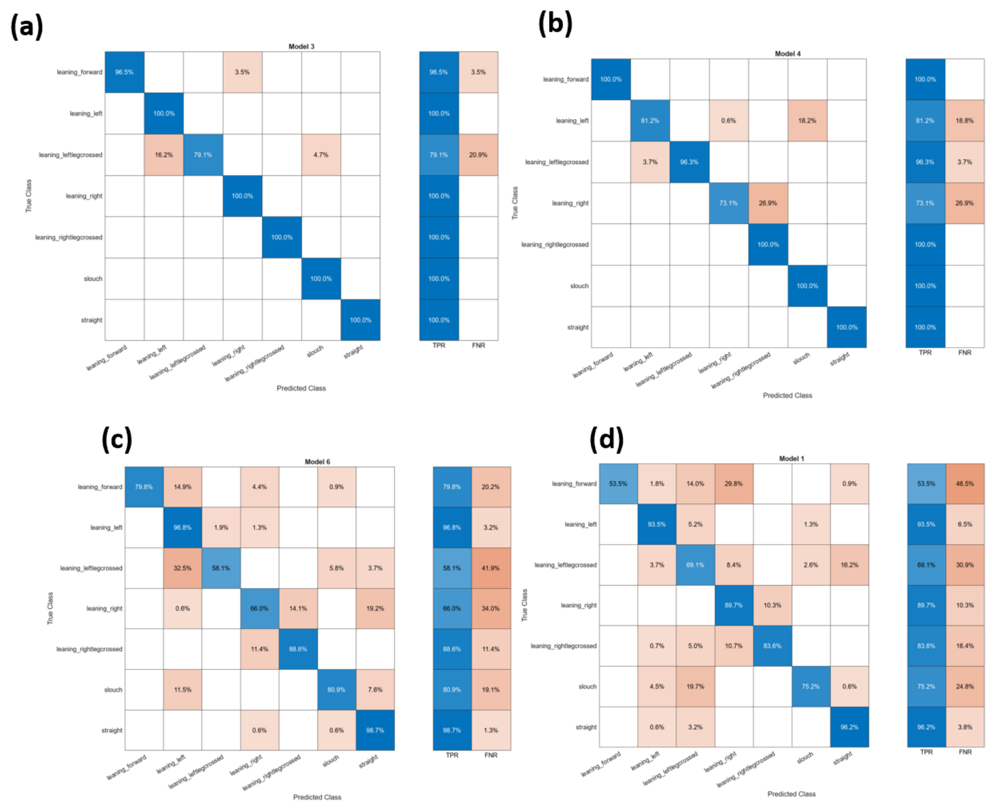

Figure 6.9 Confusion matrix of the classification results for each classifier selected with their best accuracy condition (a) Support Vector Machine (Gaussian kernel) (b) k-Nearest neighbor (k=1, Minkowski distance) (c) Logistic regression (d) Decision tree (maximum splits=425)

leaning right posture as it is confused with leaning right leg cross. Logistic regression and decision tree have the lowest accuracy of 80.47% and 80.75%, respectively, compared to other ML models. However, the decision tree model have the lowest training time of 15.13 seconds and a prediction speed of 11000 obs/sec. Table 6.4 shows the overview of the results of all the ML models used for testing.

6.6.7 Dimension reduction using t-distributed Stochastic Neighbor Embedding

We have used a dimensionality reduction technique called as t-distributed Stochastic Neighbor Embedding (t-SNE), which is commonly used for visualizing high-dimensional data in lower dimensions,

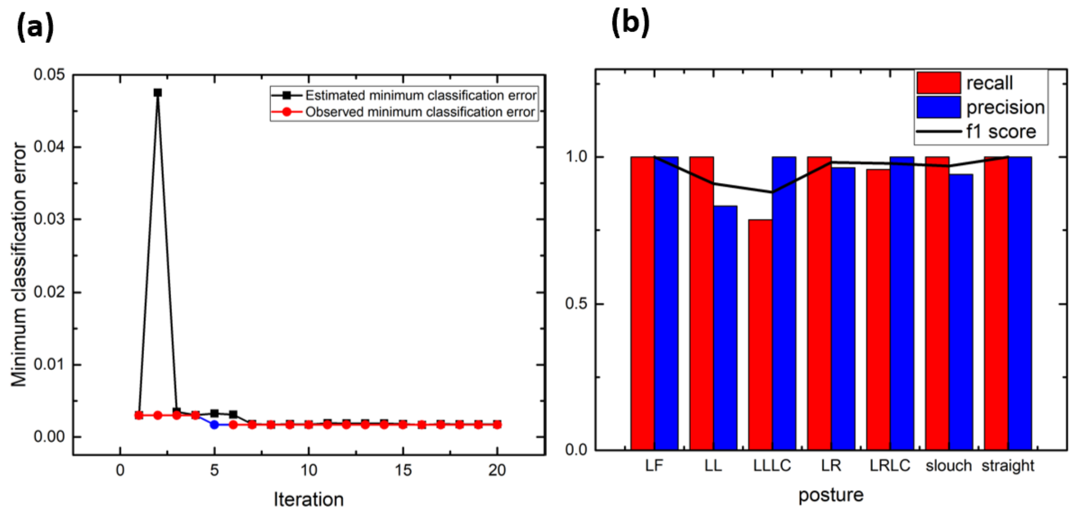

Figure 6.10 (a) Graph showing the minimum classification error for 20 iterations indicating the best hyperparameters for neural network model. (b) Graph showing the class-wise recall, precision and F1 score on testing the neural network.

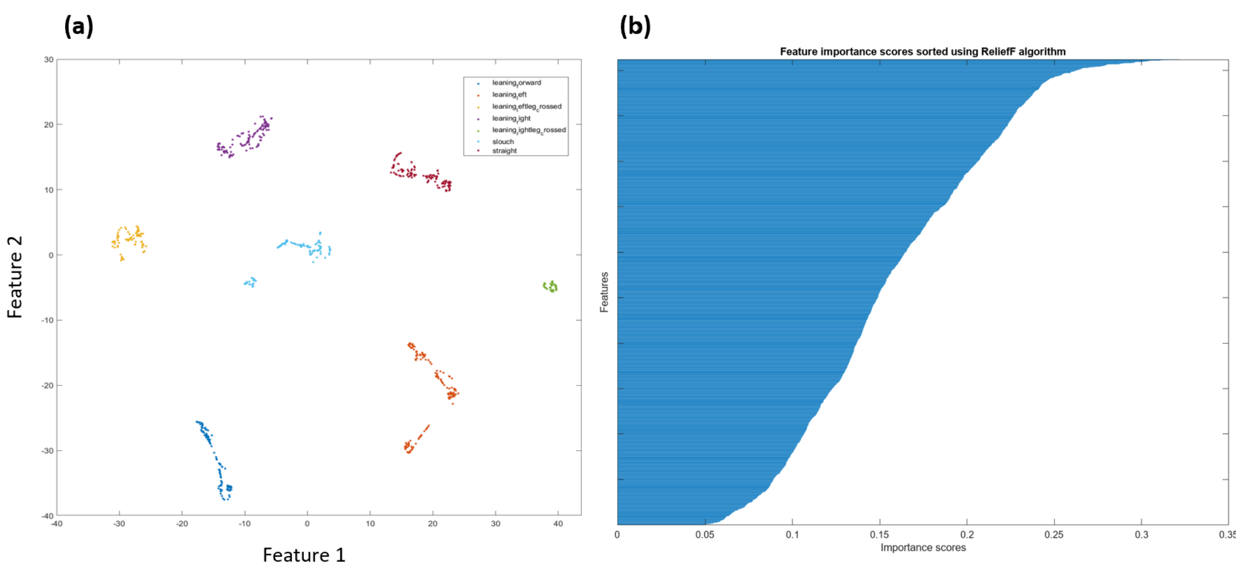

Figure 6.11 (a) t-SNE plot for the data collected for one person for different postures (b) Feature importance scores using relief feature selection (reliefF) algorithm

like 2D in this case. It does so using stochastic measures and the axes in the final plot do not have any units or physical significance, hence, they are mentioned as feature 1 and feature 2 of t-SNE. The t-SNE plot being nicely clustered shows that points that are close to each other in the t-SNE plot are likely to be similar or have similar features. This can be an indication that instances with similar characteristics or behavior are grouped together. Secondly, clear and separated clusters on the t-SNE plot may suggest

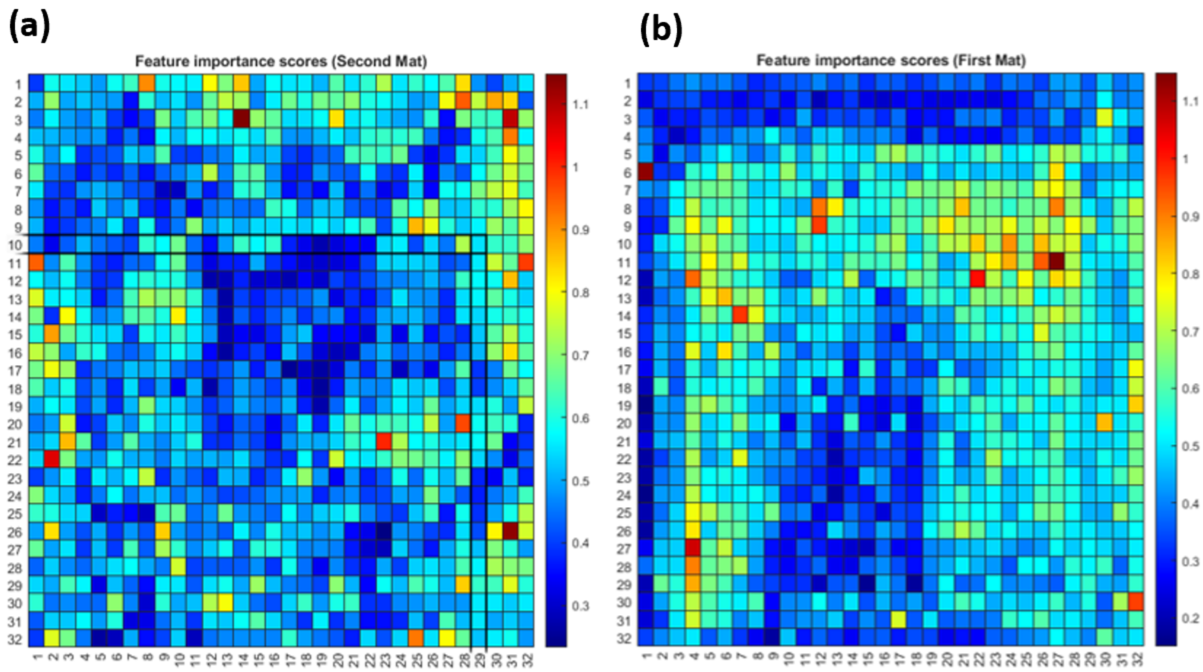

Figure 6.12 Feature importance score for the seat and the backrest

the presence of distinct classes or clusters in the data. This can be particularly useful in tasks such as unsupervised learning or clustering, where the goal is to identify natural groupings within the data.

6.6.8 Minimum Redundancy Maximum Relevance (mRMR) algorithm

The mRMR algorithm has been used to present the feature importance scores ranked for the 2048 sensors, each treated as a feature. In both the results, we can see that the importance of sensors does not fall very rapidly, this means that there are many dominant sensors. Instead, multiple features (sensors) contribute roughly equally to the predictions. Thus, it justifies the need for so many sensors throughout the mats.

6.6.9 Comparison with Previous Work

Table 6.5 shows the comparison of our work with prior work. In [168], pressure sensors and ultrasonic sensors were used for posture recognition. The sensors were pasted on the seat and the backrest. Users can improve their sitting posture by watching instructional films provided by the system that demonstrate how to stretch different body parts. [177] created a low-power sitting posture recognition system using commercially available flex sensors that were placed on the seat and the back. It detected 8 different postures. The accuracy achieved by the system was 97.7% using ANN algorithm. In [176], force-sensitive resistors (FSRs), multiplexers, and analog-to-digital converters (ADCs) make up each

Table 6.5 Comparison with previous work

References	Sensor	Position of sensor	Method	Accuracy	No.
Cho, et. al. [168] 2019	Pressure and Ultrasonic sensor	Seat and back	LBC Net	96%	7
Wang, et. al. [176] 2020	Pressure sensor	Seat and back	ANN	88.5%	8
Hu, et. al. [177] 2020	Pressure sensor	Seat, armrests, back	ANN	97.7%	6
Fan, et. al. [165] 2022	Pressure sensor matrix	Seat	CNN	99.1%	5
Wan, et. al. [178] 2021	Pressure sensor matrix	Seat	SVM	89.6%	4
Ran, et. al. [166] 2021	Pressure sensor matrix	Seat	RF	96.2%	7
Jeong, et. al. [179] 2021	Pressure and distance sensor	Seat and back	KNN	92%	6
Psai, et. al. [170] 2023	Pressure sensor	Seat	SVM	99.18%	4
Our work, et. al. 2023	Pressure sensor matrix	Seat and back	SVM	95.2%	7

sensor unit. For the chair's backrest (10 × 9) and seat pan (9 × 9), two FSR sheets were created. A new model named as spiking neural network was used for classification and identification of sitting postures. The accuracy obtained is 88.5%.

In [165], a commercially available pressure sensor mat of matrix 44 × 52 was used. The mat was placed on the seat of the chair. It was able to identify 5 postures with 99.1% accuracy using CNN model. [179] used pressure sensors and distance sensors for posture recognition. They were able to identify 6 pressure sensors with 92% accuracy using KNN model. In [166], a sensor array of dimensions 11 × 13 was designed for seat. Random Forest algorithm realized gave the classification accuracy of 96.26 %. The final system prediction time is 19 us on the Raspberry Pi, which could satisfy the practical application requirement on the embedded platform.

6.7 Summary

In this chapter, we presented the high resolution large-area array-based piezoresistive flexible pressure sensor for posture recognition of seven different postures using machine learning algorithms. We collected the sitting posture data from 15 participants, which was used as the dataset for our research, and trained them using different models like SVM, KNN, decision tree, logistic regression, and NN. We achieved an accuracy of 95.89% using the SVM model with Gaussian kernel and an accuracy of 95.61% using the NN. The SVM and NN turn out to be the best fits in terms of testing accuracy and f1 score, though the difference between them is negligible. We perform subsequent tests using the NN because of it's higher testing speed, moreover, NN shall be a better choice when the data is high-dimensional as they are capable of learning the relevant features from the data. We have also seen the feature importance score of all sensors using reliefF algorithm that justifies the need for a pressure sensor array for posture detection.

Chapter 7

Conclusion

7.1 Applications and Impact of Work

A pressure sensor-based intelligent sensing chair system has various applications in different fields. It can be used to make a smart wheelchair that can record the posture of the patient and help in fall detection. If the patient is sitting in the same position for a long time, the caretakers can monitor the patient and suggest they change their posture to avoid ulcers. Similarly, in the case of bedridden patients, we can design a bigger mat in the future for fall detection and prevention of bed sores. In future applications, smart chairs can be equipped with sensors to monitor vital signs such as heart rate, respiratory rate, along with posture. This data can be invaluable for healthcare professionals in tracking patients' health status remotely or for individuals to monitor their own health.

In office environments, smart chairs can be used to optimize workplace ergonomics. By collecting data on employees' sitting habits and posture, employers can identify areas for improvement and make adjustments to prevent discomfort and reduce the risk of musculoskeletal injuries. They can also assist individuals with mobility impairments by providing features such as automatic seat adjustment, built-in lifts, and remote control operation. These features can enhance independence and improve the quality of life for people with disabilities.

Gaming chairs with pressure sensing systems along with smart features such as built-in speakers, vibration feedback, and customizable seating positions can enhance the gaming experience and provide immersive gameplay. They can also be used in educational settings to promote better posture habits among students. They can also be integrated into virtual reality (VR) training simulations to provide a more realistic and immersive experience. Hence, they have the potential to revolutionize various aspects of daily life by providing comfort, convenience, and valuable health insights.

The integration of smart technology into everyday objects like chairs may influence social norms and behavior. For example, individuals may become more conscious of their posture and sitting habits in public spaces where smart chairs are prevalent, leading to cultural shifts in how people interact with their environment. The adoption of smart chairs could have economic implications for industries such as healthcare, manufacturing, and retail. The widespread adoption of smart chairs would have the potential to impact various aspects of society, from health and accessibility to privacy and the economy.

7.2 Major Achievements

In this doctoral thesis, we have developed a flexible pressure sensor-based system for posture recognition and correction in chairs. The designed flexible pressure sensor mat is a detachable system that can be integrated into any type of chair like an office chair, gaming chair, wheelchair, and even in driver eats of automobiles. Some of the major achievements of the work are listed as follows:

- We presented a flexible pressure sensor designed using polypyrrole-coated cotton (PCC) that was synthesized using in-situ chemical oxidative liquid polymerization. The sensor showed high sensitivity at low-pressure ranges and can measure pressures in the range of 160 Pa to 16 kPa.

- We presented the design and fabrication of a flexible pressure sensor array that works on the principle of piezoresistivity. We designed a 4×4 pressure sensor matrix to quantify the performance and progress of a patient undergoing physiotherapy. We have also developed an AI based algorithm to determine the accuracy of positioning by the patients and compared it with mathematical analysis. With this system, a patient can be asked to move a weight to a particular location (as part of regular physiotherapy), and the pressure sensor matrix can be used to calculate errors in positioning along with the time taken to complete the task.

- We presented, for the first time in the world, the mechanical reliability of a velostat-based pressure sensor. We reported the bending response by examining its reliability when subjected to repeated mechanical stress for 150 bending cycles.

- We presented, for the first time ever, the analysis of the performance of a flexible pressure sensor array under long-term and repeated loading. Tests were performed every fortnight for 210 days. We have observed that the material characteristics of the velostat material change on repeated application of pressure up to a certain time frame.

- We presented and developed the novel design of an interface circuit with flexibility to read out both capacitive and resistive type of sensors known as resistance and capacitance to digital converter. It requires less area and is more cost-effective than separate single-sensor read-out circuits.

- We finally presented the design of a smart chair system and the different machine learning algorithms used for the training and classification of seven different postures.

7.3 Future Work

This doctoral work has mainly focused on the development of flexible pressure sensors for posture recognition to develop smart chairs. Several major achievements have been presented, however, we believe there is a great prospect for further work in this field. The designed smart chair system is wired. This is one of the limitations of the designed smart chair system. To solve this, in future work, we can work on making it a wireless system with the smartphone application for easy access to our posture data. We can also design a more simplified circuit and incorporate low-power microcontrollers to minimize battery charging time. Another limitation is that the flexible pressure sensing mat is fixed on the chair; in our future work, we can incorporate the sensor mat inside the cushion of the chair to provide a more comfortable experience to the user.

In terms of AI, we can develop a system such that by utilizing the user's sitting posture data, the system could analyze the presence of conditions such as scoliosis or other spinal diseases, providing users with insights into their spinal health. Furthermore, users could share their historical data with healthcare professionals, enabling them to gain a better understanding of the user's past sitting posture and spinal health information. We can also train the system such that the chair can identify the person sitting on it using the sitting postures data. With the huge innovation in AI and increased demand in healthcare; I believe in the future, every chair will be a smart chair.

Bibliography

[1] S. I. Jung, N. K. Lee, K. W. Kang, K. Kim, and Y. L. Do, "The effect of smartphone usage time on posture and respiratory function," *Journal of physical therapy science*, vol. 28, no. 1, pp. 186–189, 2016.

[2] A. Biswas, P. I. Oh, G. E. Faulkner, R. R. Bajaj, M. A. Silver, M. S. Mitchell, and D. A. Alter, "Sedentary time and its association with risk for disease incidence, mortality, and hospitalization in adults: a systematic review and meta-analysis," *Annals of internal medicine*, vol. 162, no. 2, pp. 123–132, 2015.

[3] C. G. Ryan, P. M. Dall, M. H. Granat, and P. M. Grant, "Sitting patterns at work: objective measurement of adherence to current recommendations," *Ergonomics*, vol. 54, no. 6, pp. 531–538, 2011.

[4] G. M. Shetty, S. Jain, H. Thakur, and K. Khanna, "Prevalence of low back pain in india: A systematic review and meta-analysis," *Work*, vol. 73, no. 2, pp. 429–452, 2022.

[5] A. Matosova, "Chronic lower back pain among women in india: Evidence-based approach to risk factors and interventions," *Master's Projects and Capstones*, p. 1618, 2023.

[6] U. D. of Health, H. Services *et al.*, "National occupational research agenda for musculoskeletal disorders: Research topics for the next decade," *Public Health Services. Cincinnati, Ohio, National Institute for Occupational Safety and Health*, 2001.

[7] S. B. Mishra, A. Fatema, and A. M. Hussain, "Development of conductive surface on polyurethane foam using in-situ polymerization of pyrrole for capacitive pressure sensing," *IEEE Sensors Letters*, 2023.

[8] A. Fatema, S. B. Mishra, M. D. Gupta, and A. M. Hussain, "Polypyrrole-based cotton flexible pressure sensor using in-situ chemical oxidative polymerization," in *2023 IEEE International Conference on Flexible and Printable Sensors and Systems (FLEPS)*, 2023, pp. 1–4.

[9] M. Šetka, J. Drbohlavová, and J. Hubálek, "Nanostructured polypyrrole-based ammonia and volatile organic compound sensors," *Sens.*, vol. 17, no. 3, p. 562, 2017.

[10] A. M. Hussain, *Introduction to Flexible Electronics*. CRC Press, 2022.

[11] Y. Li, X. Cheng, M. Leung, J. Tsang, X. Tao, and M. Yuen, "A flexible strain sensor from polypyrrole-coated fabrics," *Synth. Met.*, vol. 155, no. 1, pp. 89–94, 2005.

[12] J. Mao and Z. Zhang, "Polypyrrole as electrically conductive biomaterials: synthesis, biofunctionalization, potential applications and challenges," *Cutting-Edge Enabling Technol. Regen. Med.*, pp. 347–370, 2018.

[13] S. Dong, Z. Sun, and Z. Lu, "Chloride chemical sensor based on an organic conducting polypyrrole polymer," *Analyst*, vol. 113, no. 10, pp. 1525–1528, 1988.

[14] D. Hao, B. Xu, and Z. Cai, "Polypyrrole coated knitted fabric for robust wearable sensor and heater," *J. Mater. Sci.: Mater. Electron.*, vol. 29, no. 11, pp. 9218–9226, 2018.

[15] J. Hur, K. Im, S. W. Kim, J. Kim, D.-Y. Chung, T.-H. Kim, K. H. Jo, J. H. Hahn, Z. Bao, S. Hwang *et al.*, "Polypyrrole/agarose-based electronically conductive and reversibly restorable hydrogel," *ACS Nano*, vol. 8, no. 10, pp. 10 066–10 076, 2014.

[16] M. T. Chikhaoui, A. Cot, K. Rabenorosoa, P. Rougeot, and N. Andreff, "Design and closed-loop control of a tri-layer polypyrrole-based telescopic soft robot," in *2016 IEEE/RSJ Int. Conf. Intel. Robot Syst. (IROS)*, 2016, pp. 1145–1150.

[17] S. Cui, J. Mao, M. Rouabhia, S. Elkoun, and Z. Zhang, "A biocompatible polypyrrole membrane for biomedical applications," *RSC Adv.*, vol. 11, no. 28, pp. 16 996–17 006, 2021.

[18] U. S. Bubniene, V. Ratautaite, A. Ramanavicius, and V. Bucinskas, "Conducting polymers for the design of tactile sensors," *Polymers*, vol. 14, no. 15, p. 2984, 2022.

[19] R. B. Mishra, W. Babatain, N. El-Atab, A. M. Hussain, and M. M. Hussain, "Polymer/paper-based double touch mode capacitive pressure sensing element for wireless control of robotic arm," in *2020 IEEE 15th Int. Conf. Nano/Micro Eng. Mol. Syst. (NEMS)*, 2020, pp. 95–99.

[20] N. El-Atab, R. B. Mishra, F. Al-Modaf, L. Joharji, A. A. Alsharif, H. Alamoudi, M. Diaz, N. Qaiser, and M. M. Hussain, "Soft actuators for soft robotic applications: a review," *Adv. Intell. Syst.*, vol. 2, no. 10, p. 2000128, 2020.

[21] N. El-Atab, S. F. Shaikh, S. M. Khan, and M. M. Hussain, "Bi-facial substrates enabled heterogeneous multi-dimensional integrated circuits (md-ic) for internet of things (iot) applications," *Adv. Eng. Mater.*, vol. 21, no. 7, p. 1900043, 2019.

[22] A. M. Hussain and M. M. Hussain, "Cmos-technology-enabled flexible and stretchable electronics for internet of everything applications," *Adv. Mater.*, vol. 28, no. 22, pp. 4219–4249, 2016.

[23] A. M. Hussain, F. A. Ghaffar, S. I. Park, J. A. Rogers, A. Shamim, and M. M. Hussain, "Metal/polymer based stretchable antenna for constant frequency far-field communication in wearable electronics," *Adv. Funct. Mater.*, vol. 25, no. 42, pp. 6565–6575, 2015.

[24] A. Fatema, I. Kuriakose, D. Devendra, and A. M. Hussain, "Investigation of the mechanical reliability of a velostat-based flexible pressure sensor," in *2022 IEEE Int. Conf. Flexible Printable Sens. Syst. (FLEPS)*. IEEE, 2022, pp. 1–4.

[25] I. Kuriakose, S. Chauhan, A. Fatema, and A. M. Hussain, "Wearable pressure sensor suit for real-time detection of incorrect exercise techniques," in *2022 IEEE Sens.* IEEE, 2022, pp. 1–4.

[26] A. Fatema, A. Navnit, D. Devendra, and A. M. Hussain, "A Combined Capacitance and Resistance Digital Readout Circuit for Sensory Nodes," in *2021 IEEE Sens.*, 2021, pp. 1–4.

[27] T. Sharma, S.-S. Je, B. Gill, and J. X. Zhang, "Patterning piezoelectric thin film pvdf–trfe based pressure sensor for catheter application," *Sens. Actuator A Phys.*, vol. 177, pp. 87–92, 2012.

[28] R. B. Mishra, S. F. Shaikh, A. M. Hussain, and M. M. Hussain, "Metal coated polymer and paper-based cantilever design and analysis for acoustic pressure sensing," *AIP Adv.*, vol. 10, no. 5, p. 055112, 2020.

[29] A. Fatema, S. Poondla, R. B. Mishra, and A. M. Hussain, "A Low-Cost Pressure Sensor Matrix for Activity Monitoring in Stroke Patients Using Artificial Intelligence," *IEEE Sens. J.*, vol. 21, no. 7, pp. 9546–9552, 2021.

[30] L. Pan, A. Chortos, G. Yu, Y. Wang, S. Isaacson, R. Allen, Y. Shi, R. Dauskardt, and Z. Bao, "An ultra-sensitive resistive pressure sensor based on hollow-sphere microstructure induced elasticity in conducting polymer film," *Nat. Commun.*, vol. 5, no. 1, p. 3002, 2014.

[31] S. Liu, P. Gordiichuk, Z.-S. Wu, Z. Liu, W. Wei, M. Wagner, N. Mohamed-Noriega, D. Wu, Y. Mai, A. Herrmann *et al.*, "Patterning two-dimensional free-standing surfaces with mesoporous conducting polymers," *Nat. Commun.*, vol. 6, no. 1, p. 8817, 2015.

[32] J. Fan, M. Wan, D. Zhu, B. Chang, Z. Pan, and S. Xie, "Synthesis, characterizations, and physical properties of carbon nanotubes coated by conducting polypyrrole," *J. Appl. Polym. Sci*, vol. 74, no. 11, pp. 2605–2610, 1999.

[33] S. Shukla, "Synthesis and characterization of polypyrrole grafted cellulose for humidity sensing," *Int. J. Biol. Macromol.*, vol. 62, pp. 531–536, 2013.

[34] S. H. Ravandi and M. Valizadeh, "Properties of fibers and fabrics that contribute to human comfort," in *Improving comfort in clothing*. Elsevier, 2011, pp. 61–78.

[35] J. M. Nassar, M. D. Cordero, A. T. Kutbee, M. A. Karimi, G. A. T. Sevilla, A. M. Hussain, A. Shamim, and M. M. Hussain, "Paper skin multisensory platform for simultaneous environmental monitoring," *Advanced Materials Technologies*, vol. 1, no. 1, p. 1600004, 2016.

[36] R. B. Mishra, N. El-Atab, A. M. Hussain, and M. M. Hussain, "Recent progress on flexible capacitive pressure sensors: From design and materials to applications," *Advanced Materials Technologies*, vol. 6, no. 4, p. 2001023, 2021.

[37] T. Mirfakhrai, J. D. Madden, and R. H. Baughman, "Polymer artificial muscles," *Materials today*, vol. 10, no. 4, pp. 30–38, 2007.

[38] R. B. Mishra, F. Al-Modaf, W. Babatain, A. M. Hussain, and N. El-Atab, "Structural engineering approach for designing foil-based flexible capacitive pressure sensors," *IEEE Sensors Journal*, vol. 22, no. 12, pp. 11 543–11 551, 2022.

[39] J.-W. Jeong, M. K. Kim, H. Cheng, W.-H. Yeo, X. Huang, Y. Liu, Y. Zhang, Y. Huang, and J. A. Rogers, "Capacitive epidermal electronics for electrically safe, long-term electrophysiological measurements," *Advanced Healthcare Materials*, vol. 3, no. 5, pp. 642–648, 2014.

[40] Y. Luo, M. R. Abidian, J.-H. Ahn, D. Akinwande, A. M. Andrews, M. Antonietti, Z. Bao, M. Berggren, C. A. Berkey, C. J. Bettinger *et al.*, "Technology roadmap for flexible sensors," *ACS Nano*, vol. 17, no. 6, pp. 5211–5295, 2023.

[41] L. Zou, Y. Sun, T. Dou, M. Yao, Z. Xu, and C. Lan, "Low-temperature treated polypyrrole coated cotton fabrics for efficient electromagnetic interference shielding," *Cellulose*, pp. 1–14, 2023.

[42] Y. Shi, L. Pan, B. Liu, Y. Wang, Y. Cui, Z. Bao, and G. Yu, "Nanostructured conductive polypyrrole hydrogels as high-performance, flexible supercapacitor electrodes," *Journal of Materials Chemistry A*, vol. 2, no. 17, pp. 6086–6091, 2014.

[43] A. Khan, M. Jawaid, A. A. P. Khan, and A. M. Asiri, *Electrically conductive polymers and polymer composites: from synthesis to biomedical applications*. John Wiley & Sons, 2018.

[44] A. Yussuf, M. Al-Saleh, S. Al-Enezi, and G. Abraham, "Synthesis and characterization of conductive polypyrrole: the influence of the oxidants and monomer on the electrical, thermal, and morphological properties," *International Journal of Polymer Science*, vol. 2018, 2018.

[45] B. Maharjan, V. K. Kaliannagounder, S. R. Jang, G. P. Awasthi, D. P. Bhattarai, G. Choukrani, C. H. Park, and C. S. Kim, "In-situ polymerized polypyrrole nanoparticles immobilized poly (ε-caprolactone) electrospun conductive scaffolds for bone tissue engineering," *Materials Science and Engineering: C*, vol. 114, p. 111056, 2020.

[46] M. Pruvost, W. J. Smit, C. Monteux, P. Poulin, and A. Colin, "Polymeric foams for flexible and highly sensitive low-pressure capacitive sensors," *npj Flexible Electronics*, vol. 3, no. 1, p. 7, 2019.

[47] M. Totaro, I. Bernardeschi, H. Wang, and L. Beccai, "Analysis and optimization of fully foam-based capacitive sensors," in *2020 3rd IEEE International Conference on Soft Robotics (RoboSoft)*. IEEE, 2020, pp. 470–475.

[48] X. Karagiorgis, M. Ntagios, P. Skabara, and R. Dahiya, "3d-printed elastomer foam-based soft capacitive pressure sensors," in *2022 IEEE International Conference on Flexible and Printable Sensors and Systems (FLEPS)*. IEEE, 2022, pp. 1–4.

[49] Z. He, W. Chen, B. Liang, C. Liu, L. Yang, D. Lu, Z. Mo, H. Zhu, Z. Tang, and X. Gui, "Capacitive pressure sensor with high sensitivity and fast response to dynamic interaction based on graphene and porous nylon networks," *ACS Applied Materials & Interfaces*, vol. 10, no. 15, pp. 12 816–12 823, 2018.

[50] K.-H. Ha, H. Huh, Z. Li, and N. Lu, "Soft capacitive pressure sensors: trends, challenges, and perspectives," *ACS Nano*, vol. 16, no. 3, pp. 3442–3448, 2022.

[51] S. R. A. Ruth, V. R. Feig, H. Tran, and Z. Bao, "Microengineering pressure sensor active layers for improved performance," *Advanced Functional Materials*, vol. 30, no. 39, p. 2003491, 2020.

[52] F. Rizzi, S. Puce, F. La Malfa, M. Totaro, M. De Vittorio, and L. Beccai, "Modeling and development of an auxetic foam-based multimodal capacitive strain gauge," *Smart Materials and Structures*, vol. 32, no. 2, p. 025013, 2023.

[53] S. Park, H. Kim, M. Vosgueritchian, S. Cheon, H. Kim, J. H. Koo, T. R. Kim, S. Lee, G. Schwartz, H. Chang *et al.*, "Stretchable energy-harvesting tactile electronic skin capable of differentiating multiple mechanical stimuli modes," *Advanced Materials*, vol. 26, no. 43, pp. 7324–7332, 2014.

[54] Y. Wan, N. Qin, Y. Wang, Q. Zhao, Q. Wang, P. Yuan, Q. Wen, H. Wei, X. Zhang, and N. Ma, "Sugar-templated conductive polyurethane-polypyrrole sponges for wide-range force sensing," *Chemical Engineering Journal*, vol. 383, p. 123103, 2020.

[55] A. Fatema, S. Chauhan, M. Datta, and A. M. Hussain, "Investigation of the Long-term Reliability of a Velostat-based Flexible Pressure Sensor Array for 210 Days," *IEEE Transactions on Device and Materials Reliability, 2023, unpublished*, 2023.

[56] A. Fatema, I. Kuriakose, R. Gupta, and A. M. Hussain, "Analysis of interpolation techniques for a flexible sensor mat for plantar pressure measurement," in *2023 IEEE Applied Sensing Conference (APSCON)*. IEEE, 2023, pp. 1–3.

[57] S. Muppavram, N. Patel, and M. Nadeem, "Posture alert," in *2018 IEEE Region Ten Symposium (Tensymp)*. IEEE, 2018, pp. 213–218.

[58] A. M. Lis, K. M. Black, H. Korn, and M. Nordin, "Association between sitting and occupational lbp," *European spine journal*, vol. 16, no. 2, pp. 283–298, 2007.

[59] H. Zhao, A. M. Hussain, M. Duduta, D. M. Vogt, R. J. Wood, and D. R. Clarke, "Compact dielectric elastomer linear actuators," *Advanced functional materials*, vol. 28, no. 42, p. 1804328, 2018.

[60] S. U. N. Goparaju, L. Lakshmanan, N. Abhinav, B. Rahul, B. Lovish, D. Gangadharan, and A. M. Hussain, "Time series-based driving event recognition for two wheelers," in *2023 Design, Automation & Test in Europe Conference & Exhibition (DATE)*. IEEE, 2023, pp. 1–2.

[61] S. Karmakar, A. Ranjan, and A. M. Hussain, "Fabrication and testing of a pneunet actuator-based caterpillar like amphibian soft robot for multi-terrain applications," in *2023 IEEE International Conference on Flexible and Printable Sensors and Systems (FLEPS)*. IEEE, 2023, pp. 1–4.

[62] H. Kulkarni, K. Zohaib, A. Khusru, and K. S. Aiyappa, "Application of piezoelectric technology in automotive systems," *Materials Today: Proceedings*, vol. 5, no. 10, pp. 21 299–21 304, 2018.

[63] A. Zaszczyńska, A. Gradys, and P. Sajkiewicz, "Progress in the applications of smart piezoelectric materials for medical devices," *Polymers*, vol. 12, no. 11, p. 2754, 2020.

[64] A. Tiwari, S. Chauhan, S. Bharatala, T. Ajay, N. Paleru, and A. M. Hussain, "Labour monitoring in pregnant women using electrocardiography and electromyography," in *2023 IEEE Applied Sensing Conference (APSCON)*. IEEE, 2023, pp. 1–3.

[65] Y. Wu, Y. Ma, H. Zheng, and S. Ramakrishna, "Piezoelectric materials for flexible and wearable electronics: A review," *Materials & Design*, vol. 211, p. 110164, 2021.

[66] D. Niteesh, S. Malkurthi, C. Goyal, and A. M. Hussain, "Fabrication and characterization of a dielectric elastomer actuator based flapping wing," in *2023 IEEE International Conference on Flexible and Printable Sensors and Systems (FLEPS)*. IEEE, 2023, pp. 1–4.

[67] S. S. Kumar and B. Pant, "Design principles and considerations for the 'ideal'silicon piezoresistive pressure sensor: a focused review," *Microsystem technologies*, vol. 20, pp. 1213–1247, 2014.

[68] S. M. Khan, N. Qaiser, S. F. Shaikh, and M. M. Hussain, "Design analysis and human tests of foil-based wheezing monitoring system for asthma detection," *IEEE Transactions on Electron Devices*, vol. 67, no. 1, pp. 249–257, 2019.

[69] R. B. Mishra, S. R. Nagireddy, S. Bhattacharjee, and A. M. Hussain, "Theoretical modeling and numerical simulation of elliptical capacitive pressure microsensor," in *2019 IEEE Conference on Modeling of Systems Circuits and Devices (MOS-AK India)*. IEEE, 2019, pp. 17–22.

[70] M. Akiyama, Y. Morofuji, T. Kamohara, K. Nishikubo, M. Tsubai, O. Fukuda, and N. Ueno, "Flexible piezoelectric pressure sensors using oriented aluminum nitride thin films prepared on polyethylene terephthalate films," *Journal of applied physics*, vol. 100, no. 11, 2006.

[71] S. J. M. Bamberg, A. Y. Benbasat, D. M. Scarborough, D. E. Krebs, and J. A. Paradiso, "Gait analysis using a shoe-integrated wireless sensor system," *IEEE Trans. Inf. Technol. Biomed.*, vol. 12, no. 4, pp. 413–423, 2008.

[72] A. Fatema, I. Kuriakose, D. Devendra, and A. M. Hussain, "Investigation of the mechanical reliability of a velostat-based flexible pressure sensor," in *2022 IEEE Int. Conf. Flex. Print. Sens. Syst. (FLEPS)*, 2022, pp. 1–4.

[73] L. Seminara, M. Capurro, P. Cirillo, G. Cannata, and M. Valle, "Electromechanical characterization of piezoelectric pvdf polymer films for tactile sensors in robotics applications," *Sens. Actuators A: Phys.*, vol. 169, no. 1, pp. 49–58, 2011.

[74] M. Laurenti, D. Perrone, A. Verna, C. F. Pirri, and A. Chiolerio, "Development of a flexible lead-free piezoelectric transducer for health monitoring in the space environment," *Micromachines*, vol. 6, no. 11, pp. 1729–1744, 2015.

[75] R. B. Mishra, S. M. Khan, S. F. Shaikh, A. M. Hussain, and M. M. Hussain, "Low-cost foil/paper based touch mode pressure sensing element as artificial skin module for prosthetic hand," in *2020 3rd IEEE International conference on soft robotics (RoboSoft)*. IEEE, 2020, pp. 194–200.

[76] R. Mishra, S. F. Shaikh, A. M. Hussain, and M. M. Hussain, "Metal coated polymer and paper-based cantilever design and analysis for acoustic pressure sensing," *Aip Advances*, vol. 10, no. 5, 2020.

[77] D. Giovanelli and E. Farella, "Force sensing resistor and evaluation of technology for wearable body pressure sensing," *J. Sens.*, vol. 2016, 2016.

[78] A. M. Hussain, E. B. Lizardo, G. A. Torres Sevilla, J. M. Nassar, and M. M. Hussain, "Ultrastretchable and flexible copper interconnect-based smart patch for adaptive thermotherapy," *Advanced healthcare materials*, vol. 4, no. 5, pp. 665–673, 2015.

[79] K. Kamiya, M. Kudo, H. Nonaka, and J. Toyama, "Sitting posture analysis by pressure sensors," in *2008 19th International Conference on Pattern Recognition*. IEEE, 2008, pp. 1–4.

[80] J. Cheng, B. Zhou, M. Sundholm, and P. Lukowicz, "Smart chair: What can simple pressure sensors under the chairs legs tell us about user activity," in *UBICOMM13: The Seventh International Conference on Mobile Ubiquitous Computing, Systems, Services and Technologies*, 2013, pp. 81–84.

[81] K. Flores De Jesus, M. H. Cheng, L. Jiang, E. G. Bakhoum *et al.*, "Resolution enhancement method used for force sensing resistor array," *Journal of sensors*, vol. 2015, 2015.

[82] S. Suprapto, A. Setiawan, H. Zakaria, W. Adiprawita, and B. Supartono, "Low-cost pressure sensor matrix using velostat," in *2017 5th International Conference on Instrumentation, Communications, Information Technology, and Biomedical Engineering (ICICI-BME)*. IEEE, 2017, pp. 137–140.

[83] H. Perner-Wilson and M. Satomi, "Diy wearable technology," in *ISEA 15th International Symposium on Electronic Art*, 2009.

[84] L. S. Pardue, C. Harte, and A. P. McPherson, "A low-cost real-time tracking system for violin," *Journal of New Music Research*, vol. 44, no. 4, pp. 305–323, 2015.

[85] H. Muhedinovic and D. Boskovic, "Design of iot solution for velostat footprint pressure sensor system," in *Internet of Things Technologies for HealthCare: Third International Conference, HealthyIoT 2016, Västerås, Sweden, October 18-19, 2016, Revised Selected Papers 3*. Springer, 2016, pp. 171–176.

[86] E. Jeong, J. Lee, and D. Kim, "Finger-gesture recognition glove using velostat (iccas 2011)," in *2011 11th International Conference on Control, Automation and Systems*. IEEE, 2011, pp. 206–210.

[87] R. Van Donselaar and W. Chen, "Design of a smart textile mat to study pressure distribution on multiple foam material configurations," in *Proceedings of the 4th International Symposium on Applied Sciences in Biomedical and Communication Technologies*, 2011, pp. 1–5.

[88] M. Hopkins, R. Vaidyanathan, and A. H. Mcgregor, "Examination of the performance characteristics of velostat as an in-socket pressure sensor," *IEEE Sensors Journal*, vol. 20, no. 13, pp. 6992–7000, 2020.

[89] J. Ahmad, H. Andersson, and J. Siden, "Screen-printed piezoresistive sensors for monitoring pressure distribution in wheelchair," *IEEE Sens. J.*, vol. 19, no. 6, pp. 2055–2063, 2018.

[90] P. Ramya, B. Padmapriya, and S. Poornachandra, "Foot pressure monitoring using single layer carbon loaded piezoresistive material," *Microprocess. Microsyst.*, vol. 79, p. 103263, 2020.

[91] A. Dzedzickis, E. Sutinys, V. Bucinskas, U. Samukaite-Bubniene, B. Jakstys, A. Ramanavicius, and I. Morkvenaite-Vilkonciene, "Polyethylene-carbon composite (velostat) based tactile sensor," *Polymers*, vol. 12, no. 12, p. 2905, 2020.

[92] L. Paredes-Madrid, C. A. Palacio, A. Matute, and C. A. Parra Vargas, "Underlying physics of conductive polymer composites and force sensing resistors (fsrs) under static loading conditions," *Sens.*, vol. 17, no. 9, p. 2108, 2017.

[93] A. Tihak and D. Bošković, "Experimental evaluation of challenges in designing a resistive pressure sensors," in *IEEE EUROCON 2019-18th Int. Conf. Smart Technol.* IEEE, 2019, pp. 1–6.

[94] A. Katunin and K. Krukiewicz, "Electrical percolation in composites of conducting polymers and dielectrics," *J. Polym. Eng.*, vol. 35, no. 8, pp. 731–741, 2015.

[95] S. Salibindla, B. Ripoche, D. T. Lai, and S. Maas, "Characterization of a new flexible pressure sensor for body sensor networks," in *2013 IEEE Int. Conf. Intell. Sens, Sens. Net. Inf. Process.* IEEE, 2013, pp. 27–31.

[96] J. H. Low, P. M. Khin, and C.-H. Yeow, "A pressure-redistributing insole using soft sensors and actuators," in *2015 IEEE Int. Conf. Robot. Autom. (ICRA)*. IEEE, 2015, pp. 2926–2930.

[97] R. Barba, Á. P. de Madrid, and J. G. Boticario, "Development of an inexpensive sensor network for recognition of sitting posture," *Int. J. Distrib. Sens. Netw.*, vol. 11, no. 8, p. 969237, 2015.

[98] B. W. Lee and H. Shin, "Feasibility study of sitting posture monitoring based on piezoresistive conductive film-based flexible force sensor," *IEEE Sens. J.*, vol. 16, no. 1, pp. 15–16, 2015.

[99] L. Harris, "Design and fabrication of a piezoresistive fabric sensor for ergonomic analyses," Ph.D. dissertation, University of Guelph, 2014.

[100] O. N. Athavale, N. Paskaranandavadivel, T. R. Angeli, R. Avci, and L. K. Cheng, "Design of pressure sensor arrays to assess electrode contact pressure during in vivo recordings in the gut," in *2020 42nd Conf. Proc. IEEE Eng. Med. Biol. Soc. (EMBC)*. IEEE, 2020, pp. 4204–4207.

[101] M. Vega-Barbas, I. Pau, J. Ferreira, E. Lebis, and F. Seoane, "Utilizing smart textiles-enabled sensorized toy and playful interactions for assessment of psychomotor development on children," *J. Sens.*, vol. 2015, 2015.

[102] A. H. Abdul Razak, A. Zayegh, R. K. Begg, and Y. Wahab, "Foot plantar pressure measurement system: A review," *Sens.*, vol. 12, no. 7, pp. 9884–9912, 2012.

[103] G. Ralphs, T. R. Lunsford, and J. Greenfield, "Measurement of plantar pressure using fuji prescale film—preliminary study," *J Prosthet Orthot.*, vol. 2, p. 130, 1990.

[104] L. Wafai, A. Zayegh, J. Woulfe, S. M. Aziz, and R. Begg, "Identification of foot pathologies based on plantar pressure asymmetry," *Sens.*, vol. 15, no. 8, pp. 20 392–20 408, 2015.

[105] P. R. Cavanagh and S. A. Bus, "Off-loading the diabetic foot for ulcer prevention and healing," *J. Am. Podiatr. Med. Assoc.*, vol. 100, no. 5, pp. 360–368, 2010.

[106] D. Rai and L. Aggarwal, "The study of plantar pressure distribution in normal and pathological foot," *Pol. J. Med. Phys. Eng.*, vol. 12, no. 1, pp. 25–34, 2006.

[107] M. C. Hodge, T. M. Bach, and G. M. Carter, "Orthotic management of plantar pressure and pain in rheumatoid arthritis," *Clin Biomech.*, vol. 14, no. 8, pp. 567–575, 1999.

[108] A. Konings-Pijnappels, M. Tenten-Diepenmaat, R. Dahmen, S. Verberne, J. Dekker, J. Twisk, L. Roorda, and M. van der Leeden, "Forefoot pathology in relation to plantar pressure distribution in patients with rheumatoid arthritis: A cross-sectional study in the amsterdam foot cohort," *Gait Posture*, vol. 68, pp. 317–322, 2019.

[109] H. Baan, R. Dubbeldam, A. V. Nene, and M. A. van de Laar, "Gait analysis of the lower limb in patients with rheumatoid arthritis: a systematic review," in *Semin. Arthritis Rheum.*, vol. 41, no. 6. Elsevier, 2012, pp. 768–788.

[110] M. Ferrarin, I. Carpinella, M. Rabuffetti, E. Calabrese, P. Mazzoleni, and R. Nemni, "Locomotor disorders in patients at early stages of parkinson's disease: a quantitative analysis," in *Conf. Proc. IEEE Eng. Med. Biol. Soc.*, 2006, pp. 1224–1227.

[111] M. Jenkins, Q. Almeida, S. Spaulding, R. Van Oostveen, J. Holmes, A. M. Johnson, and S. Perry, "Plantar cutaneous sensory stimulation improves single-limb support time, and emg activation patterns among individuals with parkinson's disease," *Parkinsonism Relat. Disord.*, vol. 15, no. 9, pp. 697–702, 2009.

[112] S. Kimmeskamp and E. M. Hennig, "Heel to toe motion characteristics in parkinson patients during free walking," *Clin Biomech.*, vol. 16, no. 9, pp. 806–812, 2001.

[113] A. Nieuwboer, W. De Weerdt, R. Dom, L. Peeraer, E. Lesaffre, F. Hilde, and B. Baunach, "Plantar force distribution in parkinsonian gait: a comparison between patients and age-matched control subjects." *Scand. J. Rehabil. Med. Suppl.*, vol. 31, no. 3, pp. 185–192, 1999.

[114] A. Caselli, H. Pham, J. M. Giurini, D. G. Armstrong, and A. Veves, "The forefoot-to-rearfoot plantar pressure ratio is increased in severe diabetic neuropathy and can predict foot ulceration," *Diabetes Care*, vol. 25, no. 6, pp. 1066–1071, 2002.

[115] I. C. Sacco, A. N. Hamamoto, L. M. Tonicelli, R. Watari, N. R. Ortega, and C. D. Sartor, "Abnormalities of plantar pressure distribution in early, intermediate, and late stages of diabetic neuropathy," *Gait Posture*, vol. 40, no. 4, pp. 570–574, 2014.

[116] J. Shen, F. Liu, H. Zeng, J. Wang, J.-G. Zhao, J. Zhao, F.-D. Lu, and W.-P. Jia, "Vibrating perception threshold and body mass index are associated with abnormal foot plantar pressure in type 2 diabetes outpatients," *Diabetes Technol. Ther.*, vol. 14, no. 11, pp. 1053–1059, 2012.

[117] M. Yavuz, A. Erdemir, G. Botek, G. B. Hirschman, L. Bardsley, and B. L. Davis, "Peak plantar pressure and shear locations: relevance to diabetic patients," *Diabetes Care*, vol. 30, no. 10, pp. 2643–2645, 2007.

[118] S. Taş and A. Çetin, "An investigation of the relationship between plantar pressure distribution and the morphologic and mechanic properties of the intrinsic foot muscles and plantar fascia," *Gait Posture*, vol. 72, pp. 217–221, 2019.

[119] J. K. Chia, S. Suresh, A. Kuah, J. L. Ong, J. M. Phua, and A. L. Seah, “Comparative trial of the foot pressure patterns between corrective orthotics, formthotics, bone spur pads and flat insoles in patients with chronic plantar fasciitis,” *Ann. Acad. Med.*, vol. 38, no. 10, p. 869, 2009.

[120] Y.-p. Huang, H.-T. Peng, X. Wang, Z.-R. Chen, and C.-Y. Song, “The arch support insoles show benefits to people with flatfoot on stance time, cadence, plantar pressure and contact area,” *PloS One*, vol. 15, no. 8, p. e0237382, 2020.

[121] S. A. Bus, R. Haspels, and T. E. Busch-Westbroek, “Evaluation and optimization of therapeutic footwear for neuropathic diabetic foot patients using in-shoe plantar pressure analysis,” *Diabetes Care*, vol. 34, no. 7, pp. 1595–1600, 2011.

[122] A. Erdemir, J. J. Saucerman, D. Lemmon, B. Loppnow, B. Turso, J. S. Ulbrecht, and P. R. Cavanagh, “Local plantar pressure relief in therapeutic footwear: design guidelines from finite element models,” *J. Biomech.*, vol. 38, no. 9, pp. 1798–1806, 2005.

[123] M. J. Mueller, “Application of plantar pressure assessment in footwear and insert design,” *J. Orthop. Sports Phys. Ther.*, vol. 29, no. 12, pp. 747–755, 1999.

[124] S. Lee, I. Ho, C. Yang, W. Wu, and L. Guo, “Investigation on plantar pressure pattern while jogging on treadmill,” *J. Biomech.*, vol. 40, p. S496, 2007.

[125] S. H. Mahajan and V. K. Harpale, “Adaptive and non-adaptive image interpolation techniques,” in *Int. Conf. Comput. Commun. Cont. Autom.*, 2015, pp. 772–775.

[126] S. Chauhan, A. Fatema, I. Kuriakose, and A. M. Hussain, “Efficient calibration of velostat-based flexible pressure sensor matrix,” in *2023 IEEE International Conference on Flexible and Printable Sensors and Systems (FLEPS)*, 2023, pp. 1–4.

[127] L. Lakshmanan, M. D. Gupta, A. Fatema, and A. M. Hussain, “Characterisation and quantification of crosstalk on a velostat-based flexible pressure sensing matrix,” in *2023 IEEE International Conference on Flexible and Printable Sensors and Systems (FLEPS)*, 2023, pp. 1–4.

[128] X.-W. Zhang, Y. Pan, Q. Zheng, and X.-S. Yi, “Time dependence of piezoresistance for the conductor-filled polymer composites,” *J. Polym. Sci. B Polym. Phys.*, vol. 38, no. 21, pp. 2739–2749, 2000.

[129] L. Yuan, H. Qu, and J. Li, “Velostat sensor array for object recognition,” *IEEE Sens. J.*, vol. 22, no. 2, pp. 1692–1704, 2021.

[130] S. Chen, M. Li, Y. Huang, H. Xu, G. Gu, and X. Guo, “Matrix-addressed flexible capacitive pressure sensor with suppressed crosstalk for artificial electronic skin,” *IEEE Trans. Electron Devices*, vol. 67, no. 7, pp. 2940–2944, 2020.

[131] L. Lakshmanan, M. Datta, A. Fatema, and A. M. Hussain, "Characterisation and quantification of crosstalk on a velostat-based flexible pressure sensing matrix," in *IEEE Int. Conf. Flex. Print. Sens. Syst. (FLEPS),*, 2023.

[132] C. Medrano-Sánchez, R. Igual-Catalán, V. H. Rodríguez-Ontiveros, and I. Plaza-García, "Circuit analysis of matrix-like resistor networks for eliminating crosstalk in pressure sensitive mats," *IEEE Sens. J.*, vol. 19, no. 18, pp. 8027–8036, 2019.

[133] Z. Tan, S. H. Shalmany, G. C. M. Meijer, and M. A. P. Pertijs, "An Energy-Efficient 15-Bit Capacitive-Sensor Interface Based on Period Modulation," *IEEE J. Solid-State Circuits*, vol. 47, no. 7, pp. 1703–1711, 2012.

[134] S. Oh, W. Jung, K. Yang, D. Blaauw, and D. Sylvester, "15.4b incremental sigma-delta capacitance-to-digital converter with zoom-in 9b asynchronous SAR," in *Symp. VLSI Circuits Digest Tech. Pap.*, 2014, pp. 1–2.

[135] A. Sanyal and N. Sun, "An Energy-Efficient Hybrid SAR-VCO $\Delta\Sigma$ Capacitance-to-Digital Converter in 40-nm CMOS," *IEEE J. Solid-State Circuits*, vol. 52, no. 7, pp. 1966–1976, 2017.

[136] A. K. George, J. Lee, Z. H. Kong, and M. Je, "A 0.8 V Supply- and Temperature-Insensitive Capacitance-to-Digital Converter in 0.18- μm CMOS," *IEEE Sens. J.*, vol. 16, no. 13, pp. 5354–5364, 2016.

[137] V. Ferrari, C. Ghidini, D. Marioli, and A. Taroni, "Oscillator-based signal conditioning with improved linearity for resistive sensors," *IEEE Trans. Instrum. Meas.*, vol. 47, no. 1, pp. 293–298, 1998.

[138] Z. Kokolanski, C. Gavrovski, V. Dimcev, and M. Makraduli, "Simple Interface for Resistive Sensors Based on Pulse Width Modulation," *IEEE Trans. Instrum. Meas.*, vol. 62, no. 11, pp. 2983–2992, 2013.

[139] P. Ramanathan Nagarajan, B. George, and V. J. Kumar, "An Improved Direct Digital Converter for Bridge-Connected Resistive Sensors," *IEEE Sens. J.*, vol. 16, no. 10, pp. 3679–3688, 2016.

[140] A. George, W. Shim, M. Je, and J. Lee, "A 114-AF RMS- Resolution 46-NF/10-MΩ -Range Digital-Intensive Reconfigurable RC-to-Digital Converter with Parasitic-Insensitive Femto-Farad Baseline Sensing," *IEEE Symp. VLSI Circuits*, pp. 157–158, 2018.

[141] L. Zhong, X. Lai, H. Song, and D. Xu, "Differential Capacitive Readout Circuit Using Oversampling Successive Approximation Technique," *IEEE Trans. Circuits Syst. I Regul. Pap.*, vol. 65, no. 12, pp. 4072–4085, 2018.

[142] B. Maundy and S. Gift, "Strain Gauge Amplifier Circuits," *IEEE Trans. Instrum. Meas.*, vol. 62, pp. 693–700, 04 2013.

[143] H.-C. Hong and G.-M. Lee, “A 65-fJ/Conversion-Step 0.9-V 200-kS/s Rail-to-Rail 8-bit Successive Approximation ADC,” *IEEE J. Solid-State Circuits*, vol. 42, pp. 2161–2168, 2007.

[144] Z. Zhu, Z. Qiu, M. Liu, and R. Ding, “A 6-to-10-Bit 0.5 V-to-0.9 V Reconfigurable 2 MS/s Power Scalable SAR ADC in 0.18 μm CMOS,” *IEEE Trans. Circuits Syst. I Regul. Pap.*, vol. 62, no. 3, pp. 689–696, 2015.

[145] X. Yue, “Determining the reliable minimum unit capacitance for the DAC capacitor array of SAR ADCs,” *Microelectron. J.*, vol. 44, no. 6, pp. 473–478, 2013.

[146] J. Faucett and D. Rempel, “Vdt-related musculoskeletal symptoms: Interactions between work posture and psychosocial work factors,” *American journal of industrial medicine*, vol. 26, no. 5, pp. 597–612, 1994.

[147] L. Ortiz-Hernandez, S. Tamez-Gonzalez, S. Martinez-Alcantara, and I. Mendez-Ramirez, “Computer use increases the risk of musculoskeletal disorders among newspaper office workers,” *Archives of medical research*, vol. 34, no. 4, pp. 331–342, 2003.

[148] J. P. Callaghan and S. M. McGill, “Low back joint loading and kinematics during standing and unsupported sitting,” *Ergonomics*, vol. 44, no. 3, pp. 280–294, 2001.

[149] P. Waongenngarm, A. J. van der Beek, N. Akkarakittichoke, and P. Janwantanakul, “Perceived musculoskeletal discomfort and its association with postural shifts during 4-h prolonged sitting in office workers,” *Applied Ergonomics*, vol. 89, p. 103225, 2020.

[150] T. Kim, S. Chen, and J. Lach, “Detecting and preventing forward head posture with wireless inertial body sensor networks,” in *2011 International Conference on Body Sensor Networks*. IEEE, 2011, pp. 125–126.

[151] J. E. Estrada and L. A. Vea, “Real-time human sitting posture detection using mobile devices,” in *2016 IEEE Region 10 Symposium (TENSYMP)*. IEEE, 2016, pp. 140–144.

[152] R. Gupta, S. H. Gupta, A. Agarwal, P. Choudhary, N. Bansal, and S. Sen, “A wearable multisensor posture detection system,” in *2020 4th International Conference on Intelligent Computing and Control Systems (ICICCS)*. IEEE, 2020, pp. 818–822.

[153] Z. Qian, A. E. Bowden, D. Zhang, J. Wan, W. Liu, X. Li, D. Baradoy, and D. T. Fullwood, “Inverse piezoresistive nanocomposite sensors for identifying human sitting posture,” *Sensors*, vol. 18, no. 6, p. 1745, 2018.

[154] S. Ma, W.-H. Cho, C.-H. Quan, and S. Lee, “A sitting posture recognition system based on 3 axis accelerometer,” in *2016 IEEE Conference on Computational Intelligence in Bioinformatics and Computational Biology (CIBCB)*. IEEE, 2016, pp. 1–3.

[155] L. Chin, K. S. Eu, T. T. Tay, C. Y. Teoh, and K. M. Yap, "A posture recognition model dedicated for differentiating between proper and improper sitting posture with kinect sensor," in *2019 IEEE international symposium on haptic, audio and visual environments and games (HAVE)*. IEEE, 2019, pp. 1–5.

[156] H. Sun, G.-a. Zhu, X. Cui, and J.-X. Wang, "Kinect-based intelligent monitoring and warning of students' sitting posture," in *2021 6th International Conference on Automation, Control and Robotics Engineering (CACRE)*. IEEE, 2021, pp. 338–342.

[157] E. S. Ho, J. C. Chan, D. C. Chan, H. P. Shum, Y.-m. Cheung, and P. C. Yuen, "Improving posture classification accuracy for depth sensor-based human activity monitoring in smart environments," *Computer Vision and Image Understanding*, vol. 148, pp. 97–110, 2016.

[158] W. Min, H. Cui, Q. Han, and F. Zou, "A scene recognition and semantic analysis approach to unhealthy sitting posture detection during screen-reading," *Sensors*, vol. 18, no. 9, p. 3119, 2018.

[159] L. Mu, K. Li, and C. Wu, "A sitting posture surveillance system based on image processing technology," in *2010 2nd International Conference on Computer Engineering and Technology*, vol. 1, 2010, pp. V1–692–V1–695.

[160] H. Cho, H.-J. Choi, C.-E. Lee, and C.-W. Sir, "Sitting posture prediction and correction system using arduino-based chair and deep learning model," in *2019 IEEE 12th Conference on Service-Oriented Computing and Applications (SOCA)*, 2019, pp. 98–102.

[161] L. Feng, Z. Li, C. Liu, X. Chen, X. Yin, and D. Fang, "Sitr: Sitting posture recognition using rf signals," *IEEE Internet of Things Journal*, vol. 7, no. 12, pp. 11 492–11 504, 2020.

[162] Q. Hu, X. Tang, and W. Tang, "A smart chair sitting posture recognition system using flex sensors and fpga implemented artificial neural network," *IEEE Sensors Journal*, vol. 20, no. 14, pp. 8007–8016, 2020.

[163] W. Xu, M.-C. Huang, N. Amini, L. He, and M. Sarrafzadeh, "ecushion: A textile pressure sensor array design and calibration for sitting posture analysis," *IEEE Sensors Journal*, vol. 13, no. 10, pp. 3926–3934, 2013.

[164] J. Wang, B. Hafidh, H. Dong, and A. E. Saddik, "Sitting posture recognition using a spiking neural network," *IEEE Sensors Journal*, vol. 21, no. 2, pp. 1779–1786, 2021.

[165] Z. Fan, X. Hu, W.-M. Chen, D.-W. Zhang, and X. Ma, "A deep learning based 2-dimensional hip pressure signals analysis method for sitting posture recognition," *Biomedical Signal Processing and Control*, vol. 73, p. 103432, 2022.

[166] X. Ran, C. Wang, Y. Xiao, X. Gao, Z. Zhu, and B. Chen, "A portable sitting posture monitoring system based on a pressure sensor array and machine learning," *Sensors and Actuators A: Physical*, vol. 331, p. 112900, 2021.

[167] H. Jeong and W. Park, "Developing and evaluating a mixed sensor smart chair system for real-time posture classification: Combining pressure and distance sensors," *IEEE Journal of Biomedical and Health Informatics*, vol. 25, no. 5, pp. 1805–1813, 2021.

[168] H. Cho, H.-J. Choi, C.-E. Lee, and C.-W. Sir, "Sitting posture prediction and correction system using arduino-based chair and deep learning model," in *2019 IEEE 12th Conference on Service-Oriented Computing and Applications (SOCA)*. IEEE, 2019, pp. 98–102.

[169] V. N. Vapnik, "An overview of statistical learning theory," *IEEE transactions on neural networks*, vol. 10, no. 5, pp. 988–999, 1999.

[170] M.-C. Tsai, E. T.-H. Chu, and C.-R. Lee, "An automated sitting posture recognition system utilizing pressure sensors," *Sensors*, vol. 23, no. 13, p. 5894, 2023.

[171] Z. Zhang, "Introduction to machine learning: k-nearest neighbors," *Annals of translational medicine*, vol. 4, no. 11, 2016.

[172] K. Wu, Z. Zheng, and S. Tang, "Bvdt: A boosted vector decision tree algorithm for multi-class classification problems," *International Journal of Pattern Recognition and Artificial Intelligence*, vol. 31, no. 05, p. 1750016, 2017.

[173] D. Wooff, "Logistic regression: a self-learning text," 2004.

[174] M. Huang, I. Gibson, and R. Yang, "Smart chair for monitoring of sitting behavior," *KnE Engineering*, pp. 274–280, 2017.

[175] H. Z. Tan, L. A. Slivovsky, and A. Pentland, "A sensing chair using pressure distribution sensors," *IEEE/ASME Transactions On Mechatronics*, vol. 6, no. 3, pp. 261–268, 2001.

[176] J. Wang, B. Hafidh, H. Dong, and A. El Saddik, "Sitting posture recognition using a spiking neural network," *IEEE Sensors Journal*, vol. 21, no. 2, pp. 1779–1786, 2020.

[177] Q. Hu, X. Tang, and W. Tang, "A smart chair sitting posture recognition system using flex sensors and fpga implemented artificial neural network," *IEEE Sensors Journal*, vol. 20, no. 14, pp. 8007–8016, 2020.

[178] Q. Wan, H. Zhao, J. Li, and P. Xu, "Hip positioning and sitting posture recognition based on human sitting pressure image," *Sensors*, vol. 21, no. 2, p. 426, 2021.

[179] H. Jeong and W. Park, "Developing and evaluating a mixed sensor smart chair system for real-time posture classification: Combining pressure and distance sensors," *IEEE Journal of Biomedical and Health Informatics*, vol. 25, no. 5, pp. 1805–1813, 2020.

Appendices

Arduino code for reading sensor response of FXR

```
int a;
void setup() {
  // put your setup code here, to run once:
Serial.begin(9600);
pinMode(2, OUTPUT);
Serial.println(",Res");
}

void loop() {
  // put your main code here, to run repeatedly:
  digitalWrite(2,HIGH);
  a=analogRead(A0);
  float v = ((float) a) / 1024.0 * 5.0;
  float z1=1.5*(5.0-v) / v;
  Serial.print(",");
  Serial.print(z1);
  Serial.println(" ");
  delay(1000);
}
```

Arduino code to get the sensor response of 2 × 2 array

```
int a0, a1;

void setup() {
  // put your setup code here, to run once:
  pinMode(4, OUTPUT);
  pinMode(5, OUTPUT);
  pinMode(A0, INPUT);
  pinMode(A1, INPUT);
  Serial.begin(9600);
}

void loop() {
  // put your main code here, to run repeatedly:
  digitalWrite(4,HIGH);
  {
  digitalWrite(5,LOW);
{
  delay(100);
  a0=analogRead(A0);
  a1=analogRead(A1);
  if (a0>400 && a0<600)
  {
    if(a0>a1){
    Serial.print("Sensor 1 has low pressure with value:" );
    Serial.println(a0);
    }
    else
    if( a1>400 && a1<600){
    Serial.print("Sensor 2 has low pressure  with value:");
     Serial.println(a1);
    }
  }

  if (a0>600 && a0<900)
  {
    if(a0>a1) {
    Serial.print("Sensor 1 has medium pressure with value: ");
    Serial.println(a0);
    }
    else
    if(a1>600 || a1<900){
    Serial.print("Sensor 2 has medium pressure with value: ");
    Serial.println(a1);
    }
  }
```

```
   if (a0>900 || a1>900)
  {
    if(a0>a1){
    Serial.print("Sensor 1 has high pressure with value: ");
    Serial.println(a0);
    }
    else
    Serial.print("Sensor 2 has high pressure with value: ");
    Serial.println(a1);
  }
 }
 }
digitalWrite(5,HIGH);
 {
 digitalWrite(4,LOW);
 {
  delay(100);
  a0=analogRead(A0);
  a1=analogRead(A1);
 if (a0>400 && a0<600)
  {
    if(a0>a1){
    Serial.print("Sensor 3 has low pressure with value: ");
    Serial.println(a0);
    }
    else
    if( a1>400 && a1<600){
    Serial.print("Sensor 4 has low pressure with value: ");
    Serial.println(a1);
    }
  }

  if (a0>600 && a0<900)
  {
    if(a0>a1) {
    Serial.print("Sensor 3 has medium pressure with value: ");
    Serial.println(a0);
    }
    else
    if(a1>600 || a1<900){
    Serial.print("Sensor 4 has medium pressure with value: ");
    Serial.println(a1);
    }
  }

   if (a0>900 || a1>900)
```

```
  {
    if(a0>a1)
    {
      Serial.print("Sensor 3 has high pressure with value: ");
      Serial.println(a0);
    }
    else
    Serial.print("Sensor 4 has high pressure with value: ");
     Serial.println(a1);
  }
 }
}
}
```

Arduino code to get the sensor response of 4 × 4 array

```
    int a1, a2, a3, a4; float z1,z2,z3,z4;

void setup() {
  // put your setup code here, to run once:
  pinMode(2, OUTPUT);
  pinMode(3, OUTPUT);
  pinMode(4, OUTPUT);
  pinMode(5, OUTPUT);
  pinMode(A1, INPUT);
  pinMode(A2, INPUT);
  pinMode(A3, INPUT);
  pinMode(A4, INPUT);
  Serial.begin(9600);
  Serial.println(",S1,S2,S3,S4,S5,S6,S7,S8,S9,S10,S11,S12,S13,S14,S15,S16");
}

void loop()
{
  delay(100);
  digitalWrite(2,HIGH);
  {
    digitalWrite(3,LOW);
    digitalWrite(4,LOW);
    digitalWrite(5,LOW);
    {
    a1=analogRead(A1);
    a2=analogRead(A2);
    a3=analogRead(A3);
    a4=analogRead(A4);

   z1=(5.0/1024)*a1;
  Serial.print(",");
   Serial.print(z1);
   Serial.print(",");

   z2=(5.0/1024)*a2;
   Serial.print(z2);
   Serial.print(",");

   z3=(5.0/1024)*a3;
   Serial.print(z3);
   Serial.print(",");

   z4=(5.0/1024)*a4;
   Serial.print(z4);
```

```
 Serial.print(",");

   }
  }
 digitalWrite(3,HIGH);
 {
   digitalWrite(2,LOW);
   digitalWrite(4,LOW);
   digitalWrite(5,LOW);
   {
   //delay(1000);
   a1=analogRead(A1);
   a2=analogRead(A2);
   a3=analogRead(A3);
   a4=analogRead(A4);

    z1=(5.0/1024)*a1;

 Serial.print(z1);
 Serial.print(",");

 z2=(5.0/1024)*a2;
 Serial.print(z2);
 Serial.print(",");

 z3=(5.0/1024)*a3;
 Serial.print(z3);
 Serial.print(",");

 z4=(5.0/1024)*a4;
 Serial.print(z4);
Serial.print(",");

   }
  }
 digitalWrite(4,HIGH);
 {
   digitalWrite(2,LOW);
   digitalWrite(3,LOW);
   digitalWrite(5,LOW);
   {
   //delay(1000);
   a1=analogRead(A1);
   a2=analogRead(A2);
   a3=analogRead(A3);
   a4=analogRead(A4);
 z1=(5.0/1024)*a1;
```

```

 Serial.print(z1);
 Serial.print(",");

 z2=(5.0/1024)*a2;
 Serial.print(z2);
 Serial.print(",");

 z3=(5.0/1024)*a3;
 Serial.print(z3);
 Serial.print(",");

 z4=(5.0/1024)*a4;
 Serial.print(z4);
 Serial.print(",");
  }
}
digitalWrite(5,HIGH);
{
  digitalWrite(2,LOW);
  digitalWrite(3,LOW);
  digitalWrite(4,LOW);
  {
  //delay(1000);
  a1=analogRead(A1);
  a2=analogRead(A2);
  a3=analogRead(A3);
  a4=analogRead(A4);
 z1=(5.0/1024)*a1;

 Serial.print(z1);
 Serial.print(",");

 z2=(5.0/1024)*a2;
 Serial.print(z2);
 Serial.print(",");

 z3=(5.0/1024)*a3;
 Serial.print(z3);
 Serial.print(",");

 z4=(5.0/1024)*a4;
 Serial.print(z4);

  }
}
Serial.println(" ");
```

```
}
```

Matlab code for reading data from Arduino and displaying the heat map for 4 × 4 array

```
clc
clear all;
global b;
if ~isempty(instrfind);
    fclose(instrfind);
    delete(instrfind);
end\\

b=serialport("COM7",9600);
interv=1000;
inittime=1;

while(inittime<interv)

write(b,'D5',1);
writeDigitalPin(b,'D6',0);
writeDigitalPin(b,'D9',0);
writeDigitalPin(b,'D10',0);

c=readVoltage(b, 'A1');
d=readVoltage(b, 'A2');
e=readVoltage(b, 'A3');
f=readVoltage(b, 'A4');

writeDigitalPin(b,'D5',0);
writeDigitalPin(b,'D6',1);
writeDigitalPin(b,'D9',0);
writeDigitalPin(b,'D10',0);

g=readVoltage(b, 'A1');
h=readVoltage(b, 'A2');
i=readVoltage(b, 'A3');
j=readVoltage(b, 'A4');

writeDigitalPin(b,'D5',0);
writeDigitalPin(b,'D6',0);
writeDigitalPin(b,'D9',1);
```

```
writeDigitalPin(b,'D10',0);

k=readVoltage(b, 'A1');
l=readVoltage(b, 'A2');
m=readVoltage(b, 'A3');
n=readVoltage(b, 'A4');

writeDigitalPin(b,'D5',0);
writeDigitalPin(b,'D6',0);
writeDigitalPin(b,'D9',0);
writeDigitalPin(b,'D10',1);

p=readVoltage(b, 'A1');
q=readVoltage(b, 'A2');
r=readVoltage(b, 'A3');
s=readVoltage(b, 'A4');


Z=[c d e f; g h i j; k l m n; p q r s];



heatmap(Z);
caxis([0,5]);
colormap(gca,jet);


grid ON;
inittime=inittime+1;
drawnow
end
```

Matlab code for NN analysis

```
clc
clear all;
input=xlsread(completedata.xlsx','Sheet1');
output=xlsread(completedata.xlsx','Sheet2');
x = input.';
y = output.';
net = feedforwardnet(10);
net = train(net,x,y);
view(net)
a = net(x);
new=net
   ([0.002097;0.104516;0.071452;0.050968;3.062258;0.589839;0;0;0])
perf = perform(net,a,y)
```

Arduino code for 16 × 16 pressure sensor array

```
#define muxpinAS0 2
#define muxpinAS1 3
#define muxpinAS2 4
#define muxpinAS3 5
#define muxpinBS0 6
#define muxpinBS1 7
#define muxpinBS2 8
#define muxpinBS3 9
#define sigA 10
#define sigB A1

int i,j;
void setup()
{
  Serial.begin(9600);
  pinMode(muxpinAS0, OUTPUT);
  pinMode(muxpinAS1, OUTPUT);
  pinMode(muxpinAS2, OUTPUT);
  pinMode(muxpinAS3, OUTPUT);
  pinMode(muxpinBS0, OUTPUT);
  pinMode(muxpinBS1, OUTPUT);
  pinMode(muxpinBS2, OUTPUT);
  pinMode(muxpinBS3, OUTPUT);
  pinMode(sigA,OUTPUT);
  digitalWrite(sigA, HIGH);
  pinMode(sigB, INPUT);
}
 void loop()
 {
  for(i=0;i<16;i++)
  {
    digitalWrite(muxpinAS0, bitRead(i, 0));
    digitalWrite(muxpinAS1, bitRead(i, 1));
    digitalWrite(muxpinAS2, bitRead(i, 2));
    digitalWrite(muxpinAS3, bitRead(i, 3));

    for(j=0;j<16;j++)
    {
    digitalWrite(muxpinBS0, bitRead(j, 0));
    digitalWrite(muxpinBS1, bitRead(j, 1));
    digitalWrite(muxpinBS2, bitRead(j, 2));
    digitalWrite(muxpinBS3, bitRead(j, 3));
    int sensorValue = analogRead(sigB);
    float voltage = ((float) sensorValue) / 1024.0 * 3.3;
    Serial.print(voltage);
```

```
    Serial.print(",");
    }
    Serial.println(" ");
  }
  Serial.println("***************");
  delay(1000);
}
```

Arduino code for 32 × 32 pressure sensor array

```
#define muxpinAS0 2
#define muxpinAS1 3
#define muxpinAS2 4
#define muxpinAS3 5
#define muxpinBS0 6
#define muxpinBS1 7
#define muxpinBS2 8
#define muxpinBS3 9
#define sigA A0
#define sigB A1
#define enableA1 10
#define enableA2 11
#define enableB1 12
#define enableB2 13
int i,j;
void setup()
{
  Serial.begin(115200);
  pinMode(muxpinAS0, OUTPUT);
  pinMode(muxpinAS1, OUTPUT);
  pinMode(muxpinAS2, OUTPUT);
  pinMode(muxpinAS3, OUTPUT);
  pinMode(muxpinBS0, OUTPUT);
  pinMode(muxpinBS1, OUTPUT);
  pinMode(muxpinBS2, OUTPUT);
  pinMode(muxpinBS3, OUTPUT);
  pinMode(enableA1, OUTPUT);
  pinMode(enableA2, OUTPUT);
  pinMode(enableB1, OUTPUT);
  pinMode(enableB2, OUTPUT);
  pinMode(sigA,INPUT);
  pinMode(sigB, INPUT);
}
 void loop()
 {
  for(i=0;i<16;i++)
  {
    digitalWrite(enableA1, LOW);
    digitalWrite(enableA2, HIGH);
    digitalWrite(muxpinAS0, bitRead(i, 0));
    digitalWrite(muxpinAS1, bitRead(i, 1));
    digitalWrite(muxpinAS2, bitRead(i, 2));
    digitalWrite(muxpinAS3, bitRead(i, 3));
    for(j=0;j<16;j++)
    {
```

```
    digitalWrite(enableB1, LOW);
    digitalWrite(enableB2, HIGH);
    digitalWrite(muxpinBS0, bitRead(j, 0));
    digitalWrite(muxpinBS1, bitRead(j, 1));
    digitalWrite(muxpinBS2, bitRead(j, 2));
    digitalWrite(muxpinBS3, bitRead(j, 3));
    int sensorValue = analogRead(sigA);
    //float voltage = ((float) sensorValue) / 1024.0 * 3.3;

    Serial.print(sensorValue);
    Serial.print(",");
    }
    for(j=0;j<16;j++)
    {
    digitalWrite(enableB1, HIGH);
    digitalWrite(enableB2, LOW);
    digitalWrite(muxpinBS0, bitRead(j, 0));
    digitalWrite(muxpinBS1, bitRead(j, 1));
    digitalWrite(muxpinBS2, bitRead(j, 2));
    digitalWrite(muxpinBS3, bitRead(j, 3));
    int sensorValue = analogRead(sigB);
    //float voltage = ((float) sensorValue) / 1024.0 * 3.3;

    Serial.print(sensorValue);
    Serial.print(",");
    }
    //Serial.println(" ");
  }
   for(i=0;i<16;i++)
  {
    digitalWrite(enableA1, HIGH);
    digitalWrite(enableA2, LOW);
    digitalWrite(muxpinAS0, bitRead(i, 0));
    digitalWrite(muxpinAS1, bitRead(i, 1));
    digitalWrite(muxpinAS2, bitRead(i, 2));
    digitalWrite(muxpinAS3, bitRead(i, 3));
    for(j=0;j<16;j++)
    {
    digitalWrite(enableB1, LOW);
    digitalWrite(enableB2, HIGH);
    digitalWrite(muxpinBS0, bitRead(j, 0));
    digitalWrite(muxpinBS1, bitRead(j, 1));
    digitalWrite(muxpinBS2, bitRead(j, 2));
    digitalWrite(muxpinBS3, bitRead(j, 3));
    int sensorValue = analogRead(sigA);
    //float voltage = ((float) sensorValue) / 1024.0 * 3.3;

```

```
      Serial.print(sensorValue);
      Serial.print(",");
      }
      for(j=0;j<16;j++)
      {
      digitalWrite(enableB1, HIGH);
      digitalWrite(enableB2, LOW);
      digitalWrite(muxpinBS0, bitRead(j, 0));
      digitalWrite(muxpinBS1, bitRead(j, 1));
      digitalWrite(muxpinBS2, bitRead(j, 2));
      digitalWrite(muxpinBS3, bitRead(j, 3));
      int sensorValue = analogRead(sigB);
      //float voltage = ((float) sensorValue) / 1024.0 * 3.3;

      Serial.print(sensorValue);
      Serial.print(",");
      }

  }
  Serial.println(" ");
  //Serial.println("****************");
  //delay(100);
}
```

Matlab code for reading data from Arduino and displaying the heat map for 16 $\times$ 16 array.

```
    clc
clear all;
global b;
if ~isempty(instrfind);
    fclose(instrfind);
    delete(instrfind);
end
b=arduino;
interv=100;
inittime=1;

while(inittime<interv)
writeDigitalPin(b,'D10',1);

for i=0:15

     p=bitget(i, 1);
     q=bitget(i, 2);
     r=bitget(i, 3);
     s=bitget(i, 4);
     writeDigitalPin(b, 'D2', p);
     writeDigitalPin(b, 'D3', q);
     writeDigitalPin(b, 'D4', r);
     writeDigitalPin(b, 'D5', s);


    for j=0:15

     a=bitget(j, 1);
     c=bitget(j, 2);
     d=bitget(j, 3);
     e=bitget(j, 4);
     writeDigitalPin(b, 'D6', a);
     writeDigitalPin(b, 'D7', c);
     writeDigitalPin(b, 'D8', d);
```

```
      writeDigitalPin(b, 'D9', e);

      sensorvalue(i+1,j+1) = readVoltage(b, 'A1');

    end
end
Z= [sensorvalue(1,1) sensorvalue(1,2) sensorvalue(1,3) sensorvalue
   (1,4) sensorvalue(1,5) sensorvalue(1,6) sensorvalue(1,7)
   sensorvalue(1,8) sensorvalue(1,9) sensorvalue(1,10) sensorvalue
   (1,11) sensorvalue(1,12) sensorvalue(1,13) sensorvalue(1,14)
   sensorvalue(1,15) sensorvalue(1,16);
    sensorvalue(2,1) sensorvalue(2,2) sensorvalue(2,3) sensorvalue
   (2,4) sensorvalue(2,5) sensorvalue(2,6) sensorvalue(2,7)
   sensorvalue(2,8) sensorvalue(2,9) sensorvalue(2,10) sensorvalue
   (2,11) sensorvalue(2,12) sensorvalue(2,13) sensorvalue(2,14)
   sensorvalue(2,15) sensorvalue(2,16);
    sensorvalue(3,1) sensorvalue(3,2) sensorvalue(3,3) sensorvalue
   (3,4) sensorvalue(3,5) sensorvalue(3,6) sensorvalue(3,7)
   sensorvalue(3,8) sensorvalue(3,9) sensorvalue(3,10) sensorvalue
   (3,11) sensorvalue(3,12) sensorvalue(3,13) sensorvalue(3,14)
   sensorvalue(3,15) sensorvalue(3,16);
    sensorvalue(4,1) sensorvalue(4,2) sensorvalue(4,3) sensorvalue
   (4,4) sensorvalue(4,5) sensorvalue(4,6) sensorvalue(4,7)
   sensorvalue(4,8) sensorvalue(4,9) sensorvalue(4,10) sensorvalue
   (4,11) sensorvalue(4,12) sensorvalue(4,13) sensorvalue(4,14)
   sensorvalue(4,15) sensorvalue(4,16);
    sensorvalue(5,1) sensorvalue(5,2) sensorvalue(5,3) sensorvalue
   (5,4) sensorvalue(5,5) sensorvalue(5,6) sensorvalue(5,7)
   sensorvalue(5,8) sensorvalue(5,9) sensorvalue(5,10) sensorvalue
   (5,11) sensorvalue(5,12) sensorvalue(5,13) sensorvalue(5,14)
   sensorvalue(5,15) sensorvalue(5,16);
    sensorvalue(6,1) sensorvalue(6,2) sensorvalue(6,3) sensorvalue
   (6,4) sensorvalue(6,5) sensorvalue(6,6) sensorvalue(6,7)
   sensorvalue(6,8) sensorvalue(6,9) sensorvalue(6,10) sensorvalue
   (6,11) sensorvalue(6,12) sensorvalue(6,13) sensorvalue(6,14)
   sensorvalue(6,15) sensorvalue(6,16);
    sensorvalue(7,1) sensorvalue(7,2) sensorvalue(7,3) sensorvalue
   (7,4) sensorvalue(7,5) sensorvalue(7,6) sensorvalue(7,7)
```

```
sensorvalue(7,8) sensorvalue(7,9) sensorvalue(7,10) sensorvalue
(7,11) sensorvalue(7,12) sensorvalue(7,13) sensorvalue(7,14)
sensorvalue(7,15) sensorvalue(7,16);
 sensorvalue(8,1) sensorvalue(8,2) sensorvalue(8,3) sensorvalue
(8,4) sensorvalue(8,5) sensorvalue(8,6) sensorvalue(8,7)
sensorvalue(8,8) sensorvalue(8,9) sensorvalue(8,10) sensorvalue
(8,11) sensorvalue(8,12) sensorvalue(8,13) sensorvalue(8,14)
sensorvalue(8,15) sensorvalue(8,16);
 sensorvalue(9,1) sensorvalue(9,2) sensorvalue(9,3) sensorvalue
(9,4) sensorvalue(9,5) sensorvalue(9,6) sensorvalue(9,7)
sensorvalue(9,8) sensorvalue(9,9) sensorvalue(9,10) sensorvalue
(9,11) sensorvalue(9,12) sensorvalue(9,13) sensorvalue(9,14)
sensorvalue(9,15) sensorvalue(9,16);
 sensorvalue(10,1) sensorvalue(10,2) sensorvalue(10,3)
sensorvalue(10,4) sensorvalue(10,5) sensorvalue(10,6) sensorvalue
(10,7) sensorvalue(10,8) sensorvalue(10,9) sensorvalue(10,10)
sensorvalue(10,11) sensorvalue(10,12) sensorvalue(10,13)
sensorvalue(10,14) sensorvalue(10,15) sensorvalue(10,16);
 sensorvalue(11,1) sensorvalue(11,2) sensorvalue(11,3)
sensorvalue(11,4) sensorvalue(11,5) sensorvalue(11,6) sensorvalue
(11,7) sensorvalue(11,8) sensorvalue(11,9) sensorvalue(11,10)
sensorvalue(11,11) sensorvalue(11,12) sensorvalue(11,13)
sensorvalue(11,14) sensorvalue(11,15) sensorvalue(11,16);
 sensorvalue(12,1) sensorvalue(12,2) sensorvalue(12,3)
sensorvalue(12,4) sensorvalue(12,5) sensorvalue(12,6) sensorvalue
(12,7) sensorvalue(12,8) sensorvalue(12,9) sensorvalue(12,10)
sensorvalue(12,11) sensorvalue(12,12) sensorvalue(12,13)
sensorvalue(12,14) sensorvalue(12,15) sensorvalue(12,16);
 sensorvalue(13,1) sensorvalue(13,2) sensorvalue(13,3)
sensorvalue(13,4) sensorvalue(13,5) sensorvalue(13,6) sensorvalue
(13,7) sensorvalue(13,8) sensorvalue(13,9) sensorvalue(13,10)
sensorvalue(13,11) sensorvalue(13,12) sensorvalue(13,13)
sensorvalue(13,14) sensorvalue(13,15) sensorvalue(13,16);
 sensorvalue(14,1) sensorvalue(14,2) sensorvalue(14,3)
sensorvalue(14,4) sensorvalue(14,5) sensorvalue(14,6) sensorvalue
(14,7) sensorvalue(14,8) sensorvalue(14,9) sensorvalue(14,10)
sensorvalue(14,11) sensorvalue(14,12) sensorvalue(14,13)
sensorvalue(14,14) sensorvalue(14,15) sensorvalue(14,16);
```

```
    sensorvalue(15,1) sensorvalue(15,2) sensorvalue(15,3)
   sensorvalue(15,4) sensorvalue(15,5) sensorvalue(15,6) sensorvalue
   (15,7) sensorvalue(15,8) sensorvalue(15,9) sensorvalue(15,10)
   sensorvalue(15,11) sensorvalue(15,12) sensorvalue(15,13)
   sensorvalue(15,14) sensorvalue(15,15) sensorvalue(15,16);
    sensorvalue(16,1) sensorvalue(16,2) sensorvalue(16,3)
   sensorvalue(16,4) sensorvalue(16,5) sensorvalue(16,6) sensorvalue
   (16,7) sensorvalue(16,8) sensorvalue(16,9) sensorvalue(16,10)
   sensorvalue(16,11) sensorvalue(16,12) sensorvalue(16,13)
   sensorvalue(16,14) sensorvalue(16,15) sensorvalue(16,16)];

heatmap(Z);
caxis([0,5]);
colormap(gca,jet);

grid ON;
inittime=inittime+1;
drawnow
end
```

Matlab code for reading data from Arduino and displaying the heat map for 32 $\times$ 32 array.

```
    clc
clear
s = serialport("COM6",115200);
s1 = serialport("COM27",115200);
configureTerminator(s,"LF");
configureTerminator(s1,"LF");
flush(s);
flush(s1);
while(1)
    flush(s);
    flush(s1);
    data=readline(s);
    data=readline(s);
    data1=readline(s1);
    data1=readline(s1);
    X=strsplit(data,",");
    X1=strsplit(data1,",");
    Y=X(1:1024);
    Y1=X1(1:1024);
    Z=reshape(Y,[32,32]);
    Z1=reshape(Y1,[32,32]);
    B=str2double(Z);
    B1=str2double(Z1);
    C=rot90(B);
    C1=rot90(B1);
    subplot(2,1,2);
    contourf(C)
    %color=load("CustomColormap1.mat");
    colormap("jet")
    colorbar()
    subplot(2,1,1);
    contourf(C1)
    colormap("jet")
    colorbar()
```

```
    % Append Y1 to the right of Y to create a matrix with 2048 columns
    mergedData = [str2double(Y), str2double(Y1)];

    % Write the merged data to a single CSV file
    mergedFilename = 'D:\My data\Projects\Smart chair\Test Data\Saurabh\leaning left leg cross.csv';
    writematrix(mergedData, mergedFilename, 'WriteMode', 'Append');
end
```